Electronic Transport in the Heavy Fermion Superconductors UPd_2Al_3 and UNi_2Al_3

– Thin Film Studies –

Dissertation
zur Erlangung des Grades
Doktor der Naturwissenschaften (Dr. rer. nat.)
am Fachbereich Physik
der Johannes-Gutenberg-Universität Mainz

von
Michael Foerster
geboren in Koblenz

Mainz, 2008

Referent: Datenschutz
Koreferent: Datenschutz

Tag der mündlichen Prüfung: 20.01.2009

"The American Standard translation orders men to triumph over sin, and you can call sin ignorance. The King James translation makes a promise in "Thou shalt," meaning that men will surely triumph over sin. But the Hebrew word, the word timshel"Thou mayest" that gives a choice. It might be the most important word in the world. That says the way is open. That throws it right back on a man. For if "Thou mayest"it is also true that "Thou mayest not." ... Now, there are many millions in their sects and churches who feel the order, "Do thou," and throw their weight into obedience. And there are millions more who feel predestination in "Thou shalt." Nothing they may do can interfere with what will be. But "Thou mayest"! Why, that makes a man great, that gives him stature with the gods, for in his weakness and his filth and his murder of his brother he has still the great choice. He can choose his course and fight it through and win."

Lee in *East of Eden* by J. Steinbeck

Contents

List of Figures

Introduction

Solid state physics consists of many-body problems. Although the underlying physical principles, in terms of particles (electrons and nuclei) and interactions (electromagnetism) can be considered well enough understood for this purpose, fundamental problems arise from the large amount of microscopic degrees of freedom in a macroscopic sample. Consequently, approaches to treat macroscopic ensembles have been developed, starting from the early beginnings of statistical physics and thermodynamics. The subsequent development of quantum mechanics changed drastically our understanding of the key ingredients, but left the same fundamental problem: Every system that does not consist of basically independent particles but also interactions between them is inherently difficult to describe.

Concepts have been devised to incorporate the interactions as far as possible, while keeping the calculations simple enough to arrive at some conclusion. Just to mention a few examples, treating the crystal lattice as periodic potential allows the separation of the electron system from the ionic cores (Born-Oppenheimer approximation). This is justified by the high ratio between nuclear and electronic masses, implying that changes in the ionic configuration are slow (adiabatic) for the electronic system. As another example, the Fermi liquid theory basically replaces interacting particles by almost free quasiparticles, in whose properties the original interaction is included. The mean field theory summarizes all actions on one particle by the others in a mean field, in an attempt to arrive at a self-consistent solution.

However, the concepts for treating interactions as perturbations break down and things become even more interesting when the temperature is lowered to the point where interaction energies become comparable to the thermal energy[1]. As

[1]This temperature may be zero when two competing interactions are canceling out. The result is a quantum critical point (QCP), where a phase transition is driven by quantum mechanical fluctuations at $T = 0$K. Variables of state can be applied pressure or chemical doping.

a consequence the system may undergo a phase transition, e.g. into a macroscopically ordered state like one with superconductivity or magnetic order. These collective phenomena of the electron system have always been a main focus of interest in solid state physics and require special descriptions. The reason for the great interest is certainly the intellectual challenge they pose to the researcher, but also the relevance of their applications.

Nowadays, our microscopic understanding of magnetism is based on the Heisenberg model for the exchange energy, ultimately resulting from the quantum mechanical Pauli principle. For what may be termed *classical* superconductivity exist the BCS and Eliashberg theories of a Cooper pair condensate with phonon mediated pairing. In the decade immediately following these theories, all known superconductors could be described within them. However, since the discovery of superconductivity in the heavy fermion compound $CeCu_2Si_2$, a considerable range of new *unconventional*[2] superconducting materials has emerged, which cannot be described in classical BCS terms.

Many of these new superconducting phases, like superfluid ^{3}He, heavy fermion systems and high temperature superconductors, incorporate magnetic interactions in a novel way. While in all examples known before, the two phenomena superconductivity and magnetism appeared to exclude each other or at least to compete with each other, they are found to coexist or enhance each other in these new materials. In most cases (except perhaps superfluid ^{3}He [3]) a satisfying description is still missing, rendering the interplay of these two important ordering phenomena a central topic in solid state physics today.

About this Work

The materials investigated in this work are the heavy fermion compounds UPd_2Al_3 and UNi_2Al_3, which are two examples for superconductivity arising from heavy quasiparticles in coexistence with antiferromagnetic order. At first glimpse, they display obvious similarities concerning their structure and electronic properties, but on the second viewing there are also significant differences, especially in the

[2]By definition an unconventional superconducting state is of lower symmetry than the crystal lattice, a characteristic not found in ordinary superconductors. However, at this point it may be more appropriate to relate it to any superconducting state whose properties strongly deviate from the ordinary phononic BCS scenario.

[3]Which represents a special case, since the condensate is formed from atoms and not electrons.

type of the magnetic order. Therefore, they are highly interesting objects of comparison for research addressing the interplay of superconductivity and magnetism.

In Chapter 1 of this work, some background information about heavy fermion systems is given in form of a short summary. After that, the structural and electronic properties of UPd_2Al_3 and UNi_2Al_3 are discussed with emphasis on recent developments concerning their superconducting states.

Experiments for this work were performed on UPd_2Al_3 and UNi_2Al_3 epitaxial thin films. The deposition of these by Molecular Beam Epitaxy (MBE) is described in Chapter 2, in which the epitaxial relation between substrate and film is also analyzed. One cornerstone is the finding that UPd_2Al_3 grows epitaxially in (100) orientation on $LaAlO_3$ (110) substrates, enabling the investigation of the anisotropy of transport properties. Further, the optical lithography process employed for structuring thin films and preparing mesa junctions for tunneling experiments is explained.

Thin film characterization methods are reviewed in Chapter 3. The results of these measurements, mainly X-ray diffraction, were employed in optimizing the deposition process parameters for UPd_2Al_3 (100) samples. Besides structural investigations, temperature dependent resistivity data demonstrated high sample quality by showing all features characteristic for UPd_2Al_3, including superconductivity at $T_c \approx 1.75$K. This implies a small but not negligible influence of impurities and defects.

Tunneling spectroscopy is an extremely powerful tool for investigating the superconducting density of states. In the first part of Chapter 4, a short introduction to this experimental technique is given. In the second part, results of tunneling measurements on UPd_2Al_3-AlO_x-Ag mesa contacts based on UPd_2Al_3 (100) thin films are presented. However, to date no signature of superconductivity has been observed in the measured spectra.

Chapter 5 is dedicated to the comparison of the anisotropic transport properties in UPd_2Al_3 and UNi_2Al_3. In particular the directional dependent resistive transition to superconductivity in UNi_2Al_3 is examined in detail. Results are brought in connection with Fermi surface properties and shown to support earlier interpretations. The comparison with equivalent UPd_2Al_3 (100) samples show an absence of such effect in UPd_2Al_3 and, combined with further experiments, prove this remarkable feature to be an intrinsic and unique property of UNi_2Al_3.

Chapter 1

The Superconductors UPd_2Al_3 and UNi_2Al_3

Purpose of this Chapter is to introduce the compounds UPd_2Al_3 and UNi_2Al_3. For the general context, first the phenomenon of heavy fermion systems and superconductivity therein is briefly discussed. Then a short overview on related topics of interest is given and some terms occurring in this framework are clarified.

In the main part, the properties of UPd_2Al_3 and UNi_2Al_3 are reviewed, trying to work out both, the characteristics and peculiarities with respect to the heavy fermion material class as well as to each other. One point of focus is the pairing scenario in UPd_2Al_3 and the superconducting energy gap symmetry $\Delta(\vec{k})$. This issue is covered extensively, since it is of highest interest (the clearest identification of a non-phononic pairing mechanism up to now) and stands in direct connection with Chapter 4 [1].

The part about UNi_2Al_3 is comparatively shorter, since this compound has been studied less intensely, which is due to rather the lack of high quality samples than scientific interest. Of what is known, the significant differences to UPd_2Al_3 are highlighted, such as the incommensurate magnetic order and a possible spin triplet pairing. Other materials that show phenomenological parallels are shortly discussed.

1.1 Introduction to Heavy Fermion Superconductivity

A new field in condensed matter physics opened in 1979 with the discovery of superconductivity in $CeCu_2Si_2$ by *F. Steglich et al.* [2]. Up to that point, the microscopic description of superconductivity by the Bardeen-Cooper-Schrieffer (BCS) theory and its extension to strong coupling superconductors, the Eliashberg theory, was considered complete to describe all superconducting materials. In this framework, electrons form Cooper pairs with opposite spin and momentum, mediated by the exchange of virtual phonons. Simultaneously with the formation, the bosonic Cooper pairs condense into a ground state, which can be described by a macroscopic wave function and is responsible for the properties of the superconductor. There are two aspects why the discovery of superconductivity in $CeCu_2Si_2$ was surprising and received a lot of attention [3].

First, Ce is in the $Ce^{3+}(4f^1)$ state which exhibits a localized magnetic moment associated to the $4f$ electron. In all cases that had been known previously, already small contents (around 1 atomic %) of a magnetic ion like Ce^{3+} destroys superconductivity completely. The reason for this is a possible spin flip scattering of one electron in the Cooper pair on a localized magnetic moment. Therefore, superconductivity and magnetism, which requires magnetic moments, had been seen as incompatible. This is supported by the fact that allmost all metallic elements show either superconductivity or magnetic order at sufficiently low temperatures.

However, in $CeCu_2Si_2$ the magnetic ions are necessary for superconductivity. In this compound the superconducting state is suppressed when $Ce^{3+}(4f^1)$ is replaced by a few atomic % of the nonmagnetic $La^{3+}(4f^0)$. In $CeCu_2Si_2$ nonmagnetic ions also have a strong pairbreaking effect, in contrast to conventional superconductors, where strong pairbreaking is caused in particularly by magnetic ions. And although magnetism and superconductivity had been observed in coexistence before, e.g. in rare-earth Molybdenum Chalcogenides and Rhodium Borides, in these previous cases superconducting and magnetic order are competing, while in some cases of the new material class represented by $CeCu_2Si_2$ they are coexisting, or even enhancing each other, as will be discussed later.

Second, the phononic pairing mechanism like in the BCS theory needs a retardation of the crystal lattice's movements with respect to the electrons, because of the latter strong Coulomb repulsion. Giving a simplified picture, one electron may deform the lattice which attracts another electron at a later time, thus avoid-

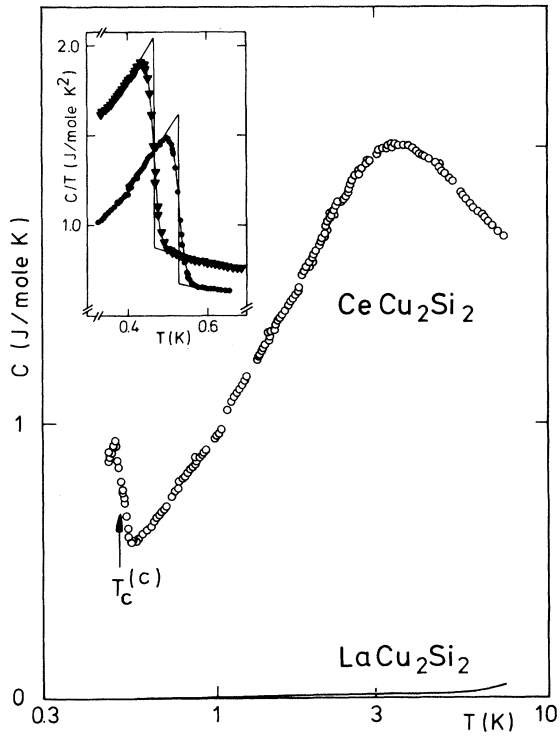

Figure 1.1: Low temperature specific heat of $CeCu_2Si_2$, published in Ref. [2]. Please note the absolute value in the order of J/(mol K) , indicating heavy fermion behavior. The jump upon entering the superconducting state at T_c is of the same order of magnitude, proving the formation of Cooper pairs from heavy quasiparticles. For comparison, the equivalent compound without $4f$ electrons, $LaCu_2Si_2$, is also shown. (Transition for two different samples in the inset.)

ing the direct Coulomb repulsion of the electrons. This mechanism only works if the speed of the lattice movement (sound velocity) is much slower compared to the electron's speed (Fermi velocity).

Now as can be seen from the jump in the specific heat (Figure 1.1) upon entering the superconducting state, in $CeCu_2Si_2$ superconducting pairs are formed from quasiparticles with very high effective mass, so called heavy fermions. The heavy quasiparticles carrying one elementary charge arise from the Kondo interaction of the localized $4f$ electrons with conduction electrons. The latter are oriented preferably antiparallel to a localized moment, screening it. This is the reason why in $CeCu_2Si_2$, despite its considerable density of magnetic moments, no magnetic order is observed. On the other hand the possibility of an f electron jumping into the conduction band while another conduction electron with opposite spin enters the f shell gives rise to a sharp many particle resonance in the

density of state just below the Fermi energy. This is expressed in terms of the hybridization matrix element V in the Anderson lattice Hamiltonian, which was originally introduced for d electrons [4]):

$$H = \sum_{\vec{k},\sigma} \epsilon(\vec{k}) c^*_{\vec{k}\sigma} c_{\vec{k}\sigma} + \sum_{i,\sigma} \epsilon_f f^*_{i\sigma} f_{i\sigma} + \frac{U}{2} \sum_{i,\sigma,\sigma'} f^*_{i\sigma} f_{i\sigma} f^*_{i\sigma'} f_{i\sigma'} + \\ + \frac{1}{\sqrt{N_s}} \sum_{i,\vec{k},\sigma} \left[V e^{-i\vec{k}\cdot\vec{R}_i} c^*_{\vec{k}\sigma} f_{i\sigma} + c.c. \right]$$

where $c^*_{\vec{k}\sigma}$ creates a conduction electron with wave vector $\vec{k}$ and spin σ; $f^*_{i\sigma}$ creates a localized f electron at the position $\vec{R}_i$; N_s is the total number of unit cells and U the Coulomb repulsion of two f electrons at the same lattice site, representing the strong correlation.

The sharpness of the resonance implies a high effective mass, in this case of $m^* \approx 380 m_0$. The Fermi velocity of such a heavy quasiparticle is comparable with the sound velocity, making a BCS phononic pairing scenario impossible.

Both of these points, as well as phenomenological similarities with the superfluidity of ^{3}He, gave rise to early speculations [5, 6] about a magnetic pairing mechanism in the heavy fermion superconductors, which nowadays include a whole family of Ce- or U-based alloys. On the other hand it should be noted that, with the huge variety of low temperature behavior observed in heavy fermion materials, there is no necessity to expect an universal explanation for superconductivity in these compounds.

Remarks on Terminology

Pairs of charge carriers giving rise to superconductivity are also referred to as *Cooper* pairs in non classical superconductors. So will be done in this work. The reason is, Cooper showed that pair formation and condensation can in principle be caused by any weak attractive electronic interaction, not only by phonon exchange as in the classical case. A non-phononic pairing mechanism is referred to as *exotic*, in contrast to the term *unconventional* superconductivity, which implies an anisotropic gap parameter $\Delta(\vec{k})$ breaking the crystal symmetry.

Further, the terms superconducting *energy gap* and *order parameter* should be distinguished, although they are sometimes used nearly synonymously in the literature. In the Ginzburg-Landau (GL) theory, a complex order parameter $\psi(\vec{r})$ is

introduced, with $\|\psi(\vec{r})\|^2$ representing the density of superconducting electrons. The microscopic superconducting gap function $\Delta(\vec{r})$ describes the energy gap $\|\Delta(\vec{r})\|$ for electron-like excitations in the superconductor (here in real space, while often used in momentum space as $\Delta(\vec{k})$. Nevertheless, in a certain limiting case of the BCS theory the relation $\psi(\vec{r}) \propto \Delta(\vec{r})$ holds [7], linking the microscopic BCS theory with the more macroscopic GL theory, which proves useful in situations where the microscopic theory becomes too difficult or is completely unknown.

Excursions

It should be noted that after their discovery in 1986 [8], another class of non-classical superconductors, the "high temperature superconductors (HTSC)" attracted even greater interest [9]. The most remarkable features of these compounds, which consist of metallic layers intertwined with CuO_2 planes, are their high critical temperatures up to $T_C = 133$K at ambient pressure, making them interesting for applications. While it is agreed upon their unconventional d-wave symmetry [10], the question of the actual pairing mechanism is not finally solved [11]. There is evidence for a magnetic origin of the attractive electron pairing interaction [12], providing a link to the heavy fermion superconductors. But since the HTSC are not the topic of this work, further details will not be explained here.

Another point of recent interest not directly addressed in this work is superconductivity in the heavy fermion system $CePt_3Si$ [13]. It was believed that its non-centro symmetric crystal structure is not compatible with spin-triplet (S=1) pairing [14]. On the other hand, in $CePt_3Si$ the experimental upper critical field B_{c2} exceeds the Pauli-Clogston limit clearly, indicating spin-triplet pairing. This contradiction was resolved recently and led into the new field of Rashba superconductors [15]. The phenomenon of a spatially varying order parameter in magnetic field resembles the Fulde-Ferrell-Larkin-Ovchinnikov(FFLO)-state which, after long search, was experimentally finally observed in the heavy fermion system $CeCoIn_5$ [16]. This ongoing research demonstrates the continuing interest in heavy fermion systems, mainly for the manifold open questions concerning the interplay of magnetism and superconductivity.

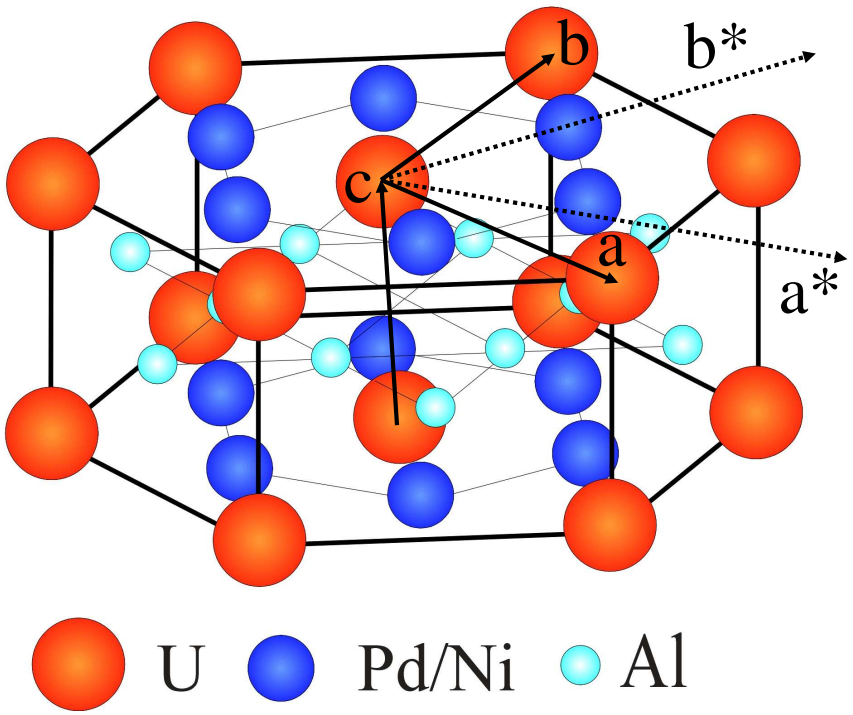

Figure 1.2: Hexagonal cell of UPd_2Al_3 and UNi_2Al_3. Lattice vectors are shown as black arrows. Directions of reciprocal lattice vectors are indicated by dotted arrows; c^* is parallel to c.

1.2 UPd_2Al_3 and UNi_2Al_3

First reports of superconductivity in UPd_2Al_3 and UNi_2Al_3 stem from *C. Geibel et al.* in 1991 [17, 18]. Most striking feature of these compounds is the coexistence of long range antiferromagnetic order and superconductivity at low temperatures. UPd_2Al_3 and UNi_2Al_3 are isostructural and isoelectronic in the sense that Ni is just above Pd in the periodic table of elements. Despite many obvious similarities, there are also significant differences between UPd_2Al_3 and UNi_2Al_3. Either will be discussed in more detail in this section.

There are reasons why scientific work has been more focused on UPd_2Al_3 than UNi_2Al_3, and therefore more experimental data, as well as theoretical work, is available. First, the preparation of UNi_2Al_3 bulk single crystals faces problems because UNi_2Al_3 decomposes peritectically into UAl_2 and melt above 1200K [19]. Further, the temperature scale, i.e. the magnetic ordering temperature T_N and the superconducting transition temperature T_c, as well as the ordered magnetic moment is considerably higher in the Pd compound, easing experiments. Last,

the realization of tunneling spectroscopy on UPd_2Al_3 in 1999 [1, 20] provided results that stirred further investigations.

Crystal Structure

UNi_2Al_3 and UPd_2Al_3 crystallize in a simple hexagonal structure (see Figure 1.2) of the $PrNi_2Al_3$ type, space group P6/mmm (No. 191), with the point group symmetry D_{6H} [19]. Lattice constants are $a = b = 5.365$Å and $c = 4.186$Å for UPd_2Al_3 while in the Ni compound the respective values are $a = b = 5.207$Å and $c = 4.018$Å [19]. The distance of two next neighbor U atoms is given by the c-axis and is slightly larger for UPd_2Al_3 compared to UNi_2Al_3. Consequently, the U $5f$ electrons in UNi_2Al_3 may be expected to have a more itinerant character compared to UPd_2Al_3, which is e.g. apparent in the smaller effective mass deduced from heat capacity measurements m* ($48m_0$ vs. $66\ m_0$ [22]). However, the actual electronic properties are complicated and far from understood in such simple terms.

1.3 UPd_2Al_3 - Electronic Properties

Fermi Surface and Itinerant vs. Dual Model

Among the heavy fermion systems, UPd_2Al_3 plays a special role. The mass enhancement, estimated from specific heat measurements (m*=$66\ m_0$ [18]) is relatively small and the ordered magnetic moment ($\mu = 0.85\mu_B$ [21]) is big and comparable to atomic values. Still, early calculations for the Fermi surface using spin-density functional theory with local density approximation (LDA) treated the $5f$ electrons as itinerant and achieved good agreement with photoemission and de Haas-van Alphen experiments [24]. However, the mass enhancement could not be reproduced in this work. The Fermi surface (shown in Figure 1.3) is divided into four parts, which are referred to as (a) "party hat", (b) "column" and "cigars" and (c) "egg".

On the other hand, there has been early evidence for the existence of two disjunct $5f$ subsystems from measurements of specific heat and conductivity under varying conditions [23]. A dual model was proposed [25, 26], in which two $5f$ electrons are localized and one is itinerant. Within this model, basically by employing LDA to only one itinerant f electron while two are kept in atomic or-

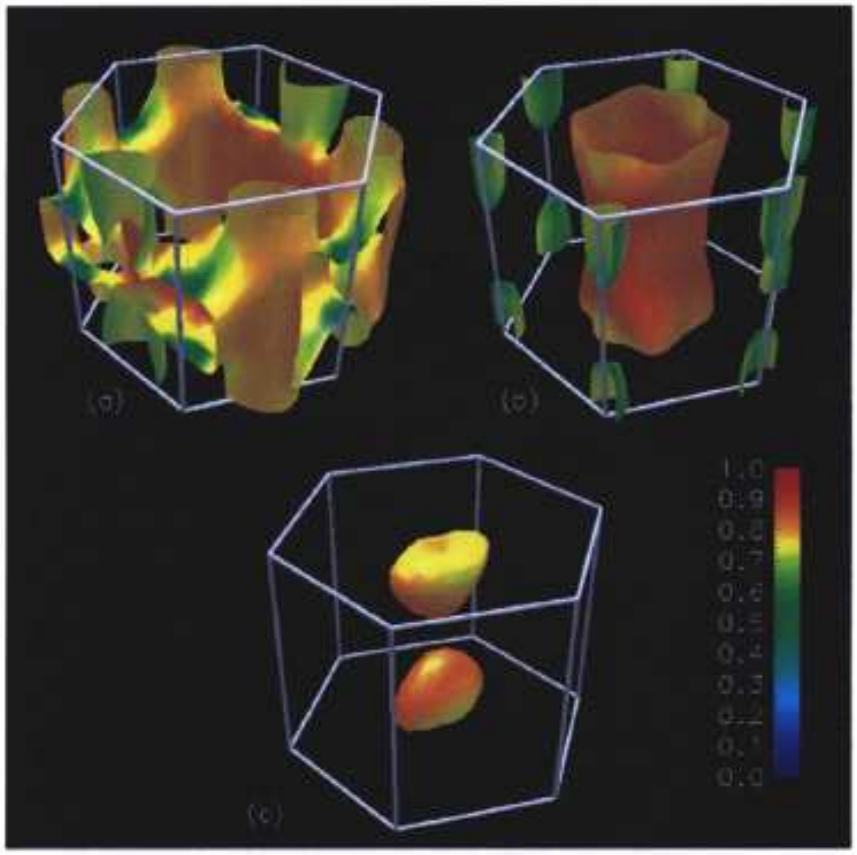

Figure 1.3: Calculated Fermi surface of UPd_2Al_3. The color represents the amount of 5f character. Graphic is taken from Ref. [24].

bitals, the Fermi surface of UPd_2Al_3 was found to resemble [25] the one calculated earlier [24]. But additionally, in this calculation there is also good agreement of the values and the anisotropies of the quasiparticle masses with experiment [25]. The decisive mechanism for the moderately heavy masses is then the interaction of the delocalized f electrons with propagating crystal field excitations associated with the localized f electrons [27], and not the hybridization of localized f electrons with conduction band (d) electrons like in the Ce-based "classical" heavy fermion systems.

Differences between the calculated Fermi surfaces concern the "party hat" part, which is found to be very sensitive to the exact Fermi energy and the "egg" part, which is substituted by a ellipsoid centered in the K-point. However, the most important part [25], the corrugated cylinder ("column") is almost not affected. Actually, in some cases the Fermi surface of UPd_2Al_3 is approximated

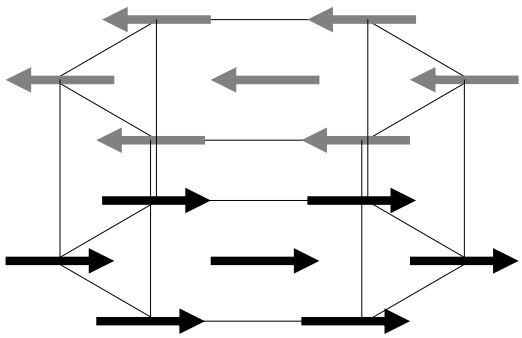

Figure 1.4: Schematic of the magnetic order in UPd_2Al_3 below $T_N = 14.3$K.

by the corrugated cylinder and is found to be sufficient to achieve agreement with experiment.

The question which model of the f electrons in UPd_2Al_3 (and other U-based systems) is more adequate is not finally decided yet. Currently the dual model is favored for UPd_2Al_3 [25, 26, 27, 28], although neutron spin-echo studies are better compatible with the itinerant model [29]. Recently, further input was provided by angle-resolved photoemission experiments (ARPES) [30], with final conclusions remaining to be drawn [31].

Magnetic Order

At low temperatures two phase transitions are observed in UPd_2Al_3. First, below $T_N = 14.3$K UPd_2Al_3 orders antiferromagnetically, characterized by an additional Bragg peak at $\vec{Q}_0 = (0, 0, 0.5)$ in elastic neutron scattering [21]. In this phase, the magnetic moments are ordered ferromagnetically in each ab-plane while neighboring planes are oriented antiparallel. The magnetic moments ($\mu = 0.85\mu_B$) are localized at the U sites [26, 32] and oriented in the ab-plane along the a-axis (Figure 1.4) [21, 33]. Excitations from the magnetic ground state have been investigated intensively by inelastic neutron scattering and play a crucial role in the following discussion about superconductivity in UPd_2Al_3.

Superconductivity

The second phase transition into the superconducting state occurs around $T_c \approx$ 2K. UPd_2Al_3 is a type-II superconductor with an anisotropic upper critical field of $\mu_0 H_{c2}(0\text{K}) \sim 4T$ (for $H \| c$) and $\mu_0 H_{c2}(0\text{K}) \sim 3.5T$ (for $H \perp c$) [34]. These

values are much smaller than the orbital upper critical field, estimated from the slope of $\mu_0 H_{c2}(T)$ at T_c after the conventional Werthamer-Helfand-Hohenberg-Maki (WHHM) theory [35, 36]:

$$H_{c2}^{orb} = 0.693(-dH_{c2}/dT|_{T_c}) \cdot T_c$$

implying the significance of Pauli paramagnetic pairbreaking. This happens to agree with the interpretation of NMR results, where a reduction of the Knight shift is observed for all orientations of the magnetic field upon entering the superconducting state [37]. Both features are widely seen to indicate spin singlet pairing, but it was pointed out, that this conclusion is not a stringent one [38][1].

Gap Symmetry

Various experiments made clear that the superconducting gap function of UPd_2Al_3 must have nodes $\Delta(\vec{k}_0) = 0$, i.e. is anisotropic. Obviously the vanishing of the energy gap for one particle excitations on parts of the Fermi surface will lead to different thermodynamical properties (in most cases to power laws instead of exponential behavior).

In NMR experiments the nuclear spin relaxation rate $1/T_1$ was found to follow a T^3 law at low temperatures [37, 39] which is characteristic for line nodes. This is in agreement with the T^2 behavior of the low-temperature thermal conductivity [40]. The results of earlier measurement of the specific heat [23], which seemed to indicate the existence of point nodes, can be explained by an additional contribution of magnetic excitations to the specific heat. However, the existence of gap nodes does not necessarily imply an unconventional gap parameter $\Delta(\vec{k})$, i.e. one that does not have the full crystal symmetry. In general, the observation of a strongly anisotropic energy gap (one with nodes) fits well with a hypothetical electronic pairing mechanism due to the strong on-site Coulomb repulsion [27].

For a more detailed analysis of the gap function symmetry, mathematical group theory is a powerful tool. To every point group, describing the crystal symmetry (D_{6H} for UPd_2Al_3), exist several different irreducible representations with known basis functions. In most cases of unconventional superconductivity the gap function $\Delta(\vec{k})$ can still be written as a linear combination of basis functions belonging to a single irreducible representation of the full point group [27, 38].

[1] The realization of an opposite-spin pair $1/\sqrt{2}(|\uparrow\downarrow> + |\downarrow\uparrow>)$ triplet state can also lead to a reduction in H_{c2}.

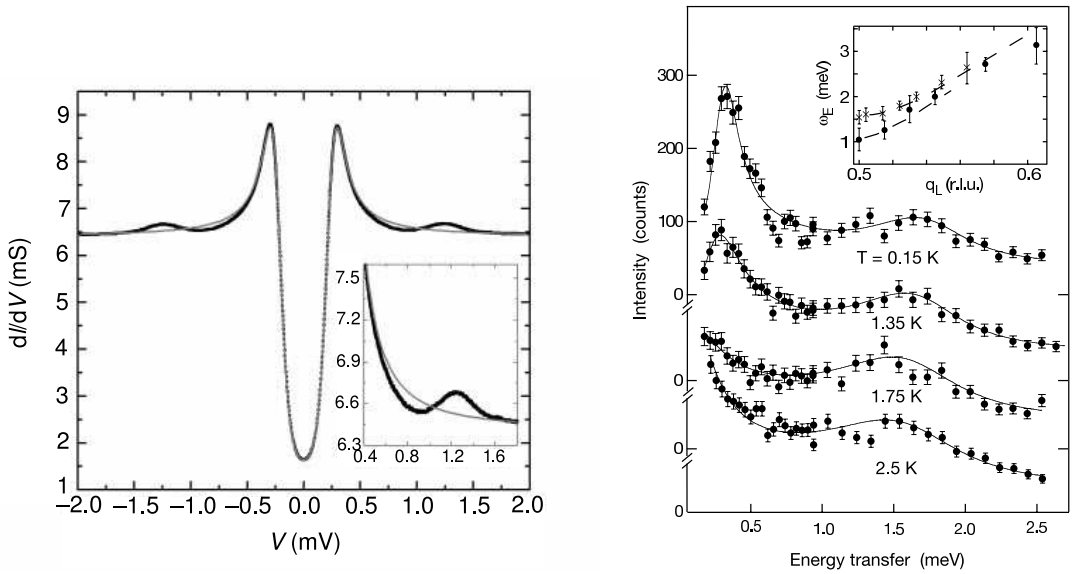

(a) (b)

Figure 1.5: Magnetic pairing: (a)Differential conductivity of an UPd_2Al_3-AlO_x-Pb planar tunneling junction at T=0.3K and μ_0H=0.3T, taken from Ref. [20]. The gray line represents a fit according to the Dynes formula for weak-coupling. Strong-coupling features are shown magnified in the inset. (b) Inelastic neutron scattering spectrum around $\vec{Q}_0$ from Ref. [43]. Dispersion relation of the magnetic exciton in the inset.

Using the possible basis functions of different irreducible representations, results of temperature and angular resolved measurements of the upper critical field B_{c2} in a UPd_2Al_3 thin films were fitted [34]. In this case, only even parity functions were considered, in accordance to the expected spin singlet pairing. While the data close to T_c could be only explained by a d-wave gap function, the best fit for low temperatures was found using an s-wave gap function, both part of the fully symmetric A_{1g} representation. Consequently, a crossover scenario between the two gap functions was proposed. Further evidence was provided by the observation of the energy gap in c-direction in planar tunneling spectroscopy [1]. All even parity irreducible representations possess a gap node along the c-axis, except for the fully symmetric A_{1g}, leaving this possibility only. The resulting gap symmetry in dependence on the polar angle Θ is then given by $\Delta(\Theta) \propto 1 - 3cos^2(\Theta)$ which is equivalent to the Y_{20} spherical harmonic.

Magnetic Pairing

The same tunneling spectroscopy experiments on a UPd_2Al_3-AlO_x-Pb planar junction led to a breakthrough in the search for the superconducting pairing mechanism in UPd_2Al_3 [1, 20]. After suppressing superconductivity in Pb by means of a small magnetic field ($B = 0.3$T , undercritical for UPd_2Al_3), the junction was investigated in a superconductor-insulator-normalconductor state (Figure 1.5.a). In this regime a deviation from the expected differential conductivity for a weak-coupling superconductor was observed for energies around 1.2 meV. The deviation can be naively interpreted as the result of an inelastic tunneling process including a boson, which mediates the pair formation. Similar strong-coupling features are found in some classical superconductors like Pb at characteristic phonon energies. While there are no phonons in the relevant energy range in UPd_2Al_3, inelastic neutron scattering reveals a magnetic excitation at around 1.5 meV (Figure 1.5.b), which indeed couples to the itinerant electrons [41, 42, 43].

Based on the assumption of such a pairing mechanism and the known magnetic order of UPd_2Al_3, general arguments allow first conclusions about the gap symmetry [44]. Since the magnetic moments are aligned and ordered ferromagnetically in the *ab*-plane, the pair partners are likely to be formed by quasiparticles in neighboring, antiferromagnetically coupled, planes. As a result, the gap function $\Delta(\vec{k})$ will be anisotropic since the spatial pair function must have a node for vanishing quasiparticle distance. Taking into account the two more three dimensional parts of the Fermi surface ("egg" and "cigar"), reasonable values for the gap size are obtained in a weak-coupling model. Further, a horizontal line node is predicted at the border of the antiferromagnetic Brillouin zone.

Subsequently, detailed analysis of the inelastic neutron scattering spectra suggested, that a particular ("egg") sheet of the Fermi surface plays the dominant role in the superconducting state [45]. Further, the neutron data was shown to be consistent with a magnetic pairing mediated by spin fluctuations. The symmetry of the gap function is required to fulfill $\Delta(\vec{k}) = -\Delta(\vec{k} + \vec{Q}_0)$.

Treating the spin fluctuations by mapping on a two-dimensional Hubbard model and solving the Eliashberg equation in perturbation theory, it was possible to predict superconductivity at the correct T_c, however these calculations involve an adjusted value for the on-site Coulomb energy U [46]. In this model only the strong interaction of the itinerant $5f$ electrons causes superconductivity while the

interaction with the localized electrons is neglected. Only one sheet ("party hat") of the Fermi surface is considered, in contrast to the neutron scattering analysis above.

Alternatively, the Eliashberg equation was treated in random-phase approximation (RPA) for a two band Hubbard model [47]. While the antiferromagnetic state is constructed from the localized f electrons, the itinerant f electrons of the more two dimensional Fermi surface parts "column" and "party hat" were considered to form the superconducting state. Two solutions were found, both possessing vertical line nodes in the gap function.

Exciton Theory

A more detailed treatment of the pairing mechanism was based on results of inelastic neutron scattering, investigating excitations in the localized f electrons system [43]. They give rise to a band of magnetic excitons, which are interpreted as propagating crystal-electric-field (CEF) excitations. Since neutrons couple mainly to the large localized moment, a peak in the scattered intensity is observed at the energy corresponding to the magnetic exciton. However, in the case of near degeneracy of the magnetic exciton and the superconducting gap energies (2Δ) and a strong on-site coupling of the itinerant electrons to the localized ones, a second peak in the spectrum is predicted due to the superconducting energy gap. The coupling causes a weight transfer and also a repulsion of the peaks, which results in a strong shift from their original positions. Using this model, it is possible to reproduce all distinctive features of the temperature and energy dependent neutron scattering data as observed in Figure 1.5.b. A value $2\Delta \approx 6k_BT_c \approx 1$meV for the superconducting energy gap (averaged over all directions in momentum space) is obtained by a fit to the experimental data. This, while in good agreement with NMR results [48], is clearly bigger than the gap observed in the tunneling experiment in c-axis direction ($\Delta \approx 235\mu$eV) [20], implying a substantial anisotropy of the gap function. Further it was shown by using an isotropic approximation, that a model of magnetic exciton mediated pairing can in principle reproduce the distinct features of the tunneling spectroscopy experiments.

A first theoretical study of this pairing mechanism [49] derived the effective nonretarded pair potential mediated by magnetic exciton exchange and solved the gap equations in a weak-coupling approach. Within these framework, the favored

superconducting state has odd parity, contrary to the experimental indications mentioned before. However, since this treatment becomes too complicated to drop the nonretarded approximation, another more simplified model for the interaction between localized and itinerant electrons was investigated [50].

The interaction was modeled by an Ising-type interaction, i.e. only the σ_z component of the conduction electron spin is relevant. Since the rotational symmetry in pseudo spin space is broken, the pairing states have to be classified in equal- and opposite-spin pairing. These states have no well-defined parity in contrast to the singlet and triplet classification of spin-rotation-symmetric models. Further, the dispersion of the magnetic exciton in the ab-plane is neglected, because it is experimentally known to have the strongest dispersion in c-direction. Consequently, the calculated pairing states have cylindrical symmetry, and only the k_z dependence can be resolved. Under these assumptions the strong-coupling formalism can be solved within the dual model of the $5f$ electrons. Finite superconducting transition temperatures result for three different gap functions. The highest T_c was found for two degenerated opposite-spin states with different parity, $cos(ck_z)$ and $sin(ck_z)$ belonging to the A_{1g} and A_{1u} irreducible representations of D_{6h}, while in the equal-spin channel, a much lower T_c is predicted for a $sin(2ck_z)$ state.

In Ref. [51] a reasonable value for the superconducting transition temperature T_c was obtained, overall providing a consistent description of the Fermi surface, heavy masses and superconductivity, thus demonstrating the possibility of exciton-mediated pairing. Taking the opposite approach, the influence of superconductivity on the magnetic excitations was studied theoretically [52] and results were found to be in good agreement with inelastic neutron scattering experiments [53], thus providing further support to the exciton mediated pairing scenario.

Magnetothermal Transport

Many studies mentioned before demonstrate the close relation between the actual microscopic pairing mechanism and the gap symmetry, a property which is in principle accessible via experiment. Accordingly, considerable effort was devoted to the further investigations of the gap symmetry.

In the last years, angle-resolved magnetothermal transport measurements have been established as an experimental means to obtain information about the gap

symmetry in unconventional superconductors [54]. The method is based on the *Volovik* effect, which influences thermodynamic properties in superconductors with line nodes in the presence of a magnetic field. The reason is, gapless quasiparticle states can tunnel from the vortex core into the inter-vortex region due to a Doppler shift in energy which they experience from the superfluid's motion (screening current) around vortices. Close to a gap node the Doppler shift, which is given by $E_{DS} = \vec{p} \cdot \vec{v}_s$ (where $\vec{p}$ is the quasiparticles momentum and $\vec{v}_s$ the velocity of the superfluid) is bigger than the energy gap $\Delta(\vec{k}) < E_{DS}$. The result is a nonvanishing zero energy density of states of quasiparticles, which determines low-temperature ($T << T_c$) heat capacity and thermal transport of the superconductor. Since the Doppler shift is given by the inner product $\vec{p} \cdot \vec{v}_s$, the zero energy density of states depends on the angle between the magnetic field and the quasiparticle momentum $\vec{p}$ at the gap nodes. Therefore a minimum in the zero energy density of states as well as the thermal conductivity will be observed for $\vec{H} \| \vec{p}$, since $\vec{v}_s \perp \vec{H}$.

Combining experimental results with a phenomenological model based on a cylindrical corrugated Fermi surface, the existence of gap nodes located perpendicular to the *ab*-plane can be excluded [55], thereby ruling out two of the proposed pairing scenarios [46, 47]. Further, at least one gap node parallel to the *ab*-plane is predicted at a position where $\vec{p}$ is in the *ab*-plane. Taking into account other experiments that indicate an even parity gap function and the symmetry requirement ($\Delta(\vec{k}) = -\Delta(\vec{k} + \vec{Q}_0)$) from inelastic neutron scattering), a gap function $\Delta(\vec{k}) \propto \Delta_0 cos(ck_z)$ was proposed, implying isotropical behavior in the *ab*-plane.

Using the same data as in Ref. [55], another evaluation suggested $\Delta(k) = \Delta_0 cos(2ck_z)$ [56], in contrast to neutron scattering results. However a third work on the same data again arrived at the original conclusion. After performing a fully quantitative analysis [27], the interpretation of Ref. [55] was supported and gap symmetries with nodal lines in off-symmetry planes could be ruled out. Among the remaining possibilities $\Delta(k) = \Delta_0 cos(ck_z)$ is favored, for the same reasons as mentioned above.

Going beyond the Doppler shift approximation, the magnetothermal conductivity was calculated using a Green's function method, including Andreev scattering at the vortex cores [57]. In this treatment, assuming already the existence of horizontal line nodes, both gap symmetries, $cos(ck_z)$ and $cos(2ck_z)$ were found to be compatible with the experiments, although the first is slightly favored.

It has to be concluded, that the existence of at least one horizontal line node in the order parameter seems assured, but their exact position along the c-axis is not finally determined. In contrast, no indication of vertical gap nodes was observed. The most likely possibility from magnetothermal transport measurements is $\Delta(\vec{k}) \propto cos(ck_z)$ (with cylindrical symmetry) which resembles the $\Delta(\Theta) \propto 1 - 3cos^2(\Theta)$ basic function deduced from group theory [2].

General Implications

Although most of the work relates to UPd_2Al_3 in particular, some general conclusions can be drawn. For example, the gap symmetry may not be influenced by the pairing mechanism alone, but also the Fermi surface can play an important role. This was demonstrated by solving the band averaged gap equation numerically over a realistic Fermi surface of UPd_2Al_3. Only one gap state with nodes was found for all different kinds of assumed pairing interaction models and varying starting configuration [58]. It belongs to the A_{1g} representation and corresponds closely to the $\Delta(\vec{k}) \propto \Delta_0 cos(ck_z)$ symmetry also favored from experiments. The influence of the Fermi surface in determining the gap symmetry is believed to be most significant in preventing gap nodes at areas of high density of states in the Brillouin zone, thus maximizing the condensation free energy.

An analogy to a BCS-like scenario, where high-frequency modes mediate pairing while low-frequency fluctuations act pairbreakingly, is observed in inelastic neutron scattering [59]. Depending on the direction of the applied magnetic field, the two resonance peaks (of Figure 1.5.b) show different behavior. The low energy peak is enhanced when the magnetic field is applied parallel b, which is the direction with a smaller upper critical field B_{c2} than the c-axis.

Recently, a similar indication of strong coupling between f-electron magnetism and superconductivity was reported in form of a resonance peak in inelastic neutron scattering for the heavy fermion compound $CeCoIn_5$ [60].

From the theory side, it was demonstrated that given the magnetic ordered structure of UPd_2Al_3, i.e. an antiferromagnetically ordered stack of ferromagnetically polarized layers, spin-singlet pairing is induced by magnetic interactions [61]. A horizontal gap node is predicted for this kind of superconductivity in coexistence with long range antiferromagnetic order. However, in this model

[2] To see this, the wave vector component k_z can be expressed in terms of the polar angle Θ, assuming a cylindrical Fermi surface.

scenario magnetic excitations are not directly causing the pairing. They are indirectly involved through an interlayer antiferromagnetic coupling term J, which originates from interlayer superexchange.

Another theoretical work found d-wave superconductivity mediated by antiferromagnetic fluctuations by a computational treatment of an Heisenberg-Kondo-Lattice model, supplemented with an antiferromagnetic interaction between localized spins [62].

In summary, non classical superconductivity in UPd_2Al_3 has attracted immense interest during the last years. Although there are still open questions which existing microscopic models cannot explain [53], UPd_2Al_3 is believed to be the best understood example of a non-phononic pairing mechanism.

Note on the Drude Response

A complete overview of the experimental work on UPd_2Al_3 must certainly include measurements of the optical conductivity [63, 64], which made it the only system in which the Drude response was observed over the complete significant frequency spectrum. Both the real and the imaginary part of the conductivity were found to follow the predictions given by the most simple model of metals from Drude in 1900 [65]. Drude derived his model treating the electrons as a classical free gas without any quantum mechanics, using the concept of a relaxation time τ between two scattering events. Owing to the mass enhancement, the Fermi velocity and the relaxation rate is reduced in UPd_2Al_3, thus shifting the relevant frequencies into a range that is accessible via microwave experiments. Adopting another point of view, the general idea of the Fermi-liquid theory, namely describing strongly correlated electrons by free quasiparticles with a renormalized mass, is nicely demonstrated, since the Drude theory is based on the assumption of free particles.

1.4 UNi_2Al_3 - Electronic Properties

The U $5f$ electrons in UNi_2Al_3 are often described as more delocalized or itinerant compared to UPd_2Al_3 [19, 26]. Indications are e.g. the smaller mass enhancement deduced from heat capacity ($48m_0$ vs. $66m_0$ for UPd_2Al_3) and a smaller magnetic

moment in the ordered state ($0.24\mu_B$[3] vs. $0.85\mu_B$) [22]. Accordingly, maxima in resistivity and susceptibility occur at higher temperatures for UNi_2Al_3, signaling more importance of the local exchange coupling between conduction and f electrons and less influence of a direct long range *f-f* interaction [19, 22]. This is also reflected in the lower magnetic ordering temperature $T_N = 4.6$K, compared to $T_N = 14.3$K in UPd_2Al_3 [22].

The reason for the difference is presumably the stronger hybridization of U $5f$ states with the Ni $3d$ states, which is predicted from band structure calculations [66] and was experimentally found to result in a small magnetic moment ($\approx$ 7% of the total ordered moment) associated to the Ni site [67]. In contrast no magnetization is found in neutron scattering at the Pd site in UPd_2Al_3.

However, there is evidence for a localized f component from photoemission [68] and the dual model ($5f^2$*(localized)* + $5f^1$*(itinerant)*) that was proposed for UPd_2Al_3 is also applied to UNi_2Al_3 [26, 31].

Up to now, no calculated Fermi surface of UNi_2Al_3 has been published, but results of a preliminary calculation carried out by Peter Oppeneer from the University of Uppsala are shown in Figure 1.6. As might be expected from the fact that UNi_2Al_3 and UPd_2Al_3 are isostructural and isoelectronic, similarities with the Fermi surface of UPd_2Al_3 are found. The first two sheets in the upper and middle panel resemble the "party hat" and the "column and cigars" parts of Figure 1.3. However, the "party hat" part of UNi_2Al_3 seems a little more 'cylindrical' compared to the one of UPd_2Al_3. Arrows in the Figure mark a region, where 'horizontal connecting areas' are less evolved compared to UPd_2Al_3. Another possible difference to UPd_2Al_3 is the vanishing of the third sheet in the lower panel, which depends sensitively on the Fermi energy, which is not known precisely enough. On the other hand, the notion of similarities between the Fermi surfaces is supported by recent observations of de Haas-van Alphen oscillations in UNi_2Al_3 [69]. They are attributed to an orbit on the cylindrical ("column") part, in equivalence to the one in UPd_2Al_3.

Magnetic Order

One important difference between UNi_2Al_3 and UPd_2Al_3 is the type of the magnetic order below $T_N \approx 4.6$K in UNi_2Al_3. The magnetic moments are modulated

[3]The magnetic order in UNi_2Al_3 differs significantly from the one in UPd_2Al_3, details are discussed below.

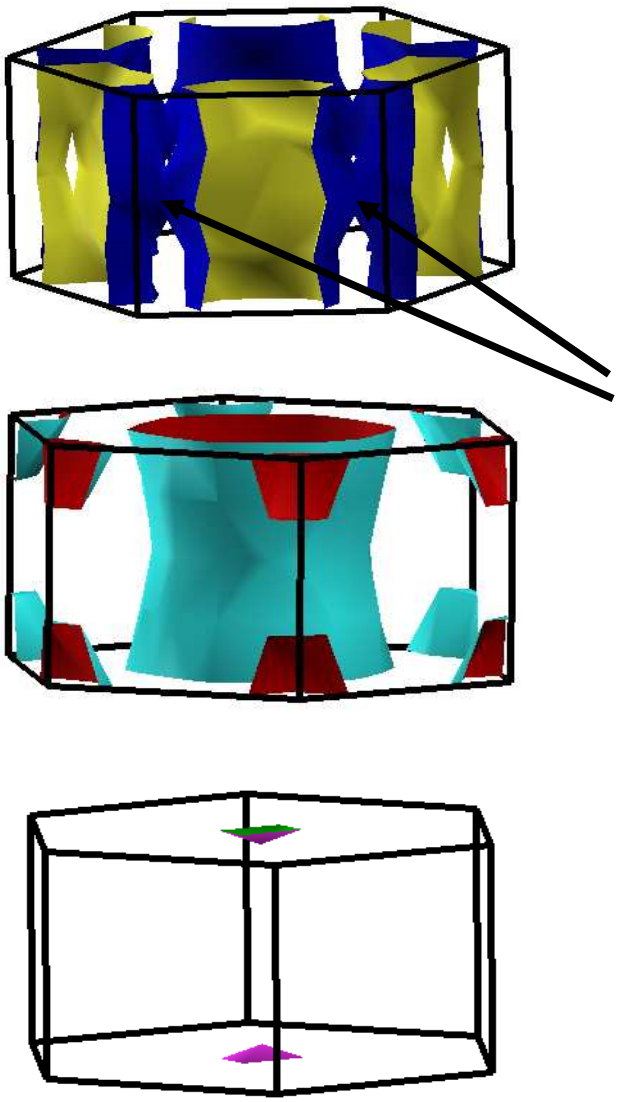

Figure 1.6: Fermi surface of UNi_2Al_3 after preliminary calculations (courtesy of Peter Oppeneer, University of Uppsala). The existence of the third sheet in the lower panel depends on the exact Fermi energy and remains open. In the region marked by the black arrows a difference compared to UPd_2Al_3 is visible.

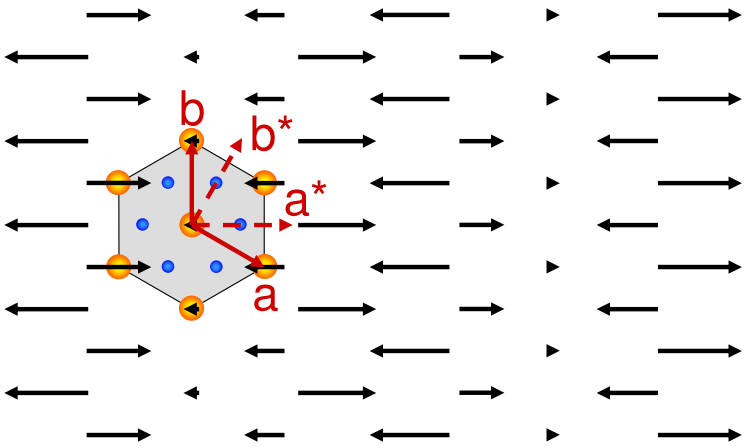

Figure 1.7: Schematic of a longitudinally polarized magnetization density wave, as realized in UNi_2Al_3 below $T_N = 4.6$K. In this two dimensional representation of the ab-plane, U sites are symbolized by red circles, Ni sites by blue ones. The lattice vectors and the direction of the reciprocal lattice vectors are indicated by red arrows.

within the *ab*-plane as a longitudinally polarized wave with the propagation vector $\vec{Q}_0 = (\pm 0.5 \pm \delta, 0, 0.5)$ with $\delta = 0.11$ in reciprocal lattice units [70]. Thus, it is incommensurate, i.e. no simple relation with regard to the crystal lattice periodicity exists. The maximum ordered moment is $\mu_{ord} \approx 0.24\mu_B$ and the moments are aligned along the a^*-direction [71]. A schematic of the magnetization in the *ab*-plane is shown in Figure 1.7. Along the *c*-axis, layers are simply antiferromagnetically stacked, like in UPd_2Al_3.

It was pointed out [71] that the a^*-vector is parallel to the real space direction between U and Ni/Pd sites, while the *a*-axis is directed between two U sites. The change of the magnetic moment orientation toward the Ni site in UNi_2Al_3 (from toward the U site in UPd_2Al_3) is another hint for a stronger hybridization of the U $5f$ electrons with Ni $3d$ states than with the Pd $4d$ states.

Stimulated by the observations in UPd_2Al_3 summarized before, an intensive search for analogous indications of a coupling between superconductivity and magnetism was carried out for UNi_2Al_3 [72, 73]. But in contrast to UPd_2Al_3, no changes in the magnetic fluctuations could be detected by inelastic neutron scattering upon entering the superconducting state in UNi_2Al_3 within the experimental resolution (0.1meV). However, a change concerning the magnetic structure was found for energy transfers exceeding the scale of the magnetic ordering temperature $T_N \sim 0.5$meV. Spectral weight is transferred from the incommensurate ordering vector $\vec{Q}_0 = (\pm 0.5 \pm \delta, 0, 0.5)$ to the commensurate ordering vector

exp.	sample	dir.	T_c [K]	H_{c2}(0K) [T/μ_0]	$dH_{c2}/dT\|_{T_c}$ [T/μ_0K]	H_{c2}^p [T/μ_0]	H_{c2}^{orb} [T/μ_0]
#1 [75] $R(T)\|_H$	poly cryst.	-	1.015	0.99	1.3	1.87	0.91
#2 [76]		$H\|a$	(0.91)*	0.9	1.14	1.8	0.79
$R(H)\|_T$	single	$H\|c$	(0.91)*	0.35	0.42	1.8	0.29
#3 [69]	cryst.	$H\|a$	0.89	0.93	1.4	1.6	0.92
$\chi(H)''\|_T$		$H\|c$	0.88	0.76	1.1	1.6	0.73
#4 [77]	thin	$H\|a$	0.98	∼1.6	>5	1.8	>3.5
$R(T)\|_H$	film	$H\|c$	0.98	∼1.6	>5	1.8	>3.5

Table 1.1: Summary of upper critical field H_{c2} measurements on UNi_2Al_3. H_{c2}(0K) are extrapolated values. The paramagnetic critical field H_{c2}^p is calculated in the Chandrasekhar-Clogstone limit, neglecting orbital interactions [7]: $\mu_0 H_{c2}^p = 1.84\text{T/K}\cdot T_c$. In the other limit, considering orbital pairbreaking only, H_{c2}^{orb} is estimated after the WHHM theory: $H_{c2}^{orb} = 0.693(-dH_{c2}/dT|_{T_c}) \cdot T_c$ (in experiment #3, the clean limit is used with the numerical factor 0.727). This is a rather rough estimation, since the WHHM theory supposes an s-wave order parameter. *: value is not given in the original publication, obviously $T_c \approx 1$K is assumed. Another publication for the same sample states $T_c = 0.91$K [78].

$\vec{Q} = (0, 0, 0.5)$, characteristic for the UPd_2Al_3 magnetic order.

Superconductivity

In UNi_2Al_3 the superconducting state is found below the critical temperature $T_c \approx 1$K. Like for UPd_2Al_3, the existence of line gap nodes is deduced from NMR experiments [74]. Assuming a $\Delta(\Theta) = \Delta_0 cos(\Theta)$ type gap function, a ratio of $2\Delta_0/k_B T_c \sim 5$ is estimated, which corresponds to $\Delta_0 \sim 0.2$meV.

There are several publications reporting measurements of the upper critical field H_{c2} in UNi_2Al_3. An overview is given in Table 1.1. Some differences are due to sample quality, reflecting the difficulties of preparing high quality UNi_2Al_3 crystals. Significant discrepancies appear in the slope of $H_{c2}(T)$ at T_c, from which the orbital upper critical field H_{c2}^{orb} is estimated. In thin films (experiment #4), H_{c2}^{orb} clearly exceeds the extrapolated H_{c2}(0K), indicating a contribution of paramagnetic pairbreaking. At the same time, these samples show the highest absolute values of the upper critical fields. In the other experiments, the reported upper

critical fields closely correspond to the estimated orbital upper critical fields. The second situation is in principal compatible with a spin triplet superconducting state, but does not require such a scenario.

However, an indication of spin triplet pairing was found in NMR experiments [78]. In contrast to UPd_2Al_3, no reduction of the Knight shift was observed upon entering the superconducting state, at least for $H \| a$ [4].

Remarkably, in UNi_2Al_3 a dependence of the resistive superconducting transition on the current direction was found recently [77, 79]. This striking observation was investigated in detail in the scope of this work. For clarity, the previous and new results as well as an interpretation are presented together in Chapter 5.

In conclusion, the magnetic exciton scenario and other models proposed for UPd_2Al_3, cannot be applied directly to UNi_2Al_3, since the magnetic state, which is supposed to give rise to the superconducting pairing in the former, is considerably different in the latter.

Possibly Related Materials

Since superconductivity in UNi_2Al_3 has to be understood in quite different terms than in UPd_2Al_3, it may prove useful to search for other systems with similar phenomenology.

Comparisons to Sr_2RuO_4 have been drawn [78], which can be grown to very high purity and consequently is well documented [80]. In Sr_2RuO_4, superconductivity evolves from a strongly two dimensional Fermi liquid with moderately increased quasiparticles masses. The Fermi surface consists of three corrugated cylinders, and incommensurate antiferromagnetic spin fluctuations have been observed, resembling the situation found in UNi_2Al_3. From polarized neutron scattering and NMR Knight shift measurements, indications for a spin triplet superconducting pair state are provided [81, 82].

The heavy fermion compound UPt_3 is another example for coexistence of antiferromagnetic order, characterized by $\vec{Q}_0 = (0.5, 0, 1)$ and a small ordered moment $\mu = 0.01\mu_B$, with superconductivity [83]. Most striking feature is the existence of three different phases in the $H - T$ phase diagram, which is assumed

[4] The Knight shift of the central peak in the NMR spectrum is due to the field generated by polarized spins of conduction electrons or quasiparticles at the nuclei in the applied magnetic field. In a superconducting singlet state, the electrons or quasiparticles form opposite spin pairs and the resulting field vanishes.

to result from the coupling of spin triplet superconductivity to the symmetry breaking magnetic order [83]. The dual model of the U $5f$ electrons as known from UPd_2Al_3 has also been applied to UPt_3, yielding good agreement of the anisotropic heavy mass and the de Haas-van Alphen frequencies with experiments [84].

Commensurate and incommensurate antiferromagnetic order in coexistence with superconductivity are also found in the heavy fermion systems $CeRh_{1-x}Ir_xIn_5$ and $CeRh_{1-x}Co_xIn_5$. In the first, for intermediate values of x, superconductivity coexists with both types of antiferromagnetic order, incommensurate ($\vec{Q}_i = (0.5, 0.5, \pm\delta)$ with $\delta = 0.297$) and commensurate ($\vec{Q}_c = (0.5, 0.5, 0.5)$) [85]. The ordered magnetic moments are of the same order of magnitude like in $U(Ni,Pd)_2Al_3$: $\mu_i = 0.73\mu_B$ and $\mu_c = 0.27\mu_B$. However, the same f electron (Ce^{3+} is in the $4f^1$ state) is responsible for all three phenomena, an important difference to the dual models proposed for UPd_2Al_3. In contrast, in $CeRh_{1-x}Co_xIn_5$ superconductivity competes with the incommensurate antiferromagnetic order, while it coexists with the commensurate order [86]. Here the proposed explanation is that areas on the Fermi surface which are active in forming the superconducting state are missing in the incommensurately ordered state due to nesting by $\vec{Q}_i$.

Chapter 2

Sample Preparation

The work presented here is based on thin film samples of UPd_2Al_3 and UNi_2Al_3. Although the successful preparation of high quality metallic thin film samples poses a challenge to experimenters, they offer considerable advantages compared to bulk samples. One main focus of thin film experiments are electronic transport measurements, which are central to this work. The main advantages of thin films in this area can be summarized as follows:

- Because of the small thickness, films have high resistances, which allows for more accurate transport measurements, since the sensitivity is usually limited by the voltage measurement in conducting materials. For example, the resistivity in the mixed state of a type-II superconductor or Hall-effect can be better observed in this case.
- Employing standard optical lithography, any desired 2-dimensional structure can be designed. This allows the investigation of directional dependent properties in (almost) any defined crystallographic direction.
- After the deposition process a fresh and smooth interface is available, which can be used e.g. for preparing in-situ tunneling contacts.
- From the technical point of view, thin film samples can be produced with high throughput and small material input.

Various methods for depositing thin metallic films exist, featuring different characteristics. Techniques most frequently employed in research include Sputtering, Molecular-Beam-Epitaxy (MBE) and Pulsed-Laser-Deposition (PLD). Without going into details here, in all these cases atoms or clusters are produced from

a reservoir of material. These particles are adsorbed by a supporting layer, the substrate, and form the thin film. From this deposition process, some critical points arise, which have to be considered for successful preparation:

- Since metallic thin films are usually reactive, an ultra-high-vacuum (UHV) environment is needed to prevent oxidation as well as the inclusion of impurity atoms in the sample. Obviously, high purity starting material has to be used as well.

- A suitable temperature in the crystal growth zone is needed to allow adatoms enough mobility to form the crystal structure. But also too high temperatures can result in defects, when the kinetic energy of the adatom is too high to stay in the right position. Further, it may lead to increased sample roughness, which presents a problem e.g. for the subsequent deposition of a homogeneous tunneling barrier.

- When using elemental sources to deposit an alloy, the relative deposition rates have to be adjusted. Since different elements can have different ad- and desorption coefficients, the evaporation rates may have to be off-stoichiometric, opening a wide parameter range.

However, even after optimization the crystal defect density in thin films usually cannot be reduced to levels comparable with the best bulk single crystals, which becomes apparent e.g. in a lower residual resistance ratio ($RRR = R(300\text{K})/R_n(0\text{K})$) or a reduced transition temperature T_c. Therefore it is necessary to check to what extent the thin film samples are representative for bulk behavior.

As another point, the same orientation of the microscopic crystal axes over the macroscopic sample, is often needed, e.g. to measure an observable in a specified direction. In polycrystalline samples with randomly oriented grains, physical properties will be averaged over all crystal directions. This essential requirement can be addressed by the right choice of substrate material which will be discussed later. However, the substrate-film interaction can also lead to strain in the thin film, resulting in changed lattice parameters or dislocations.

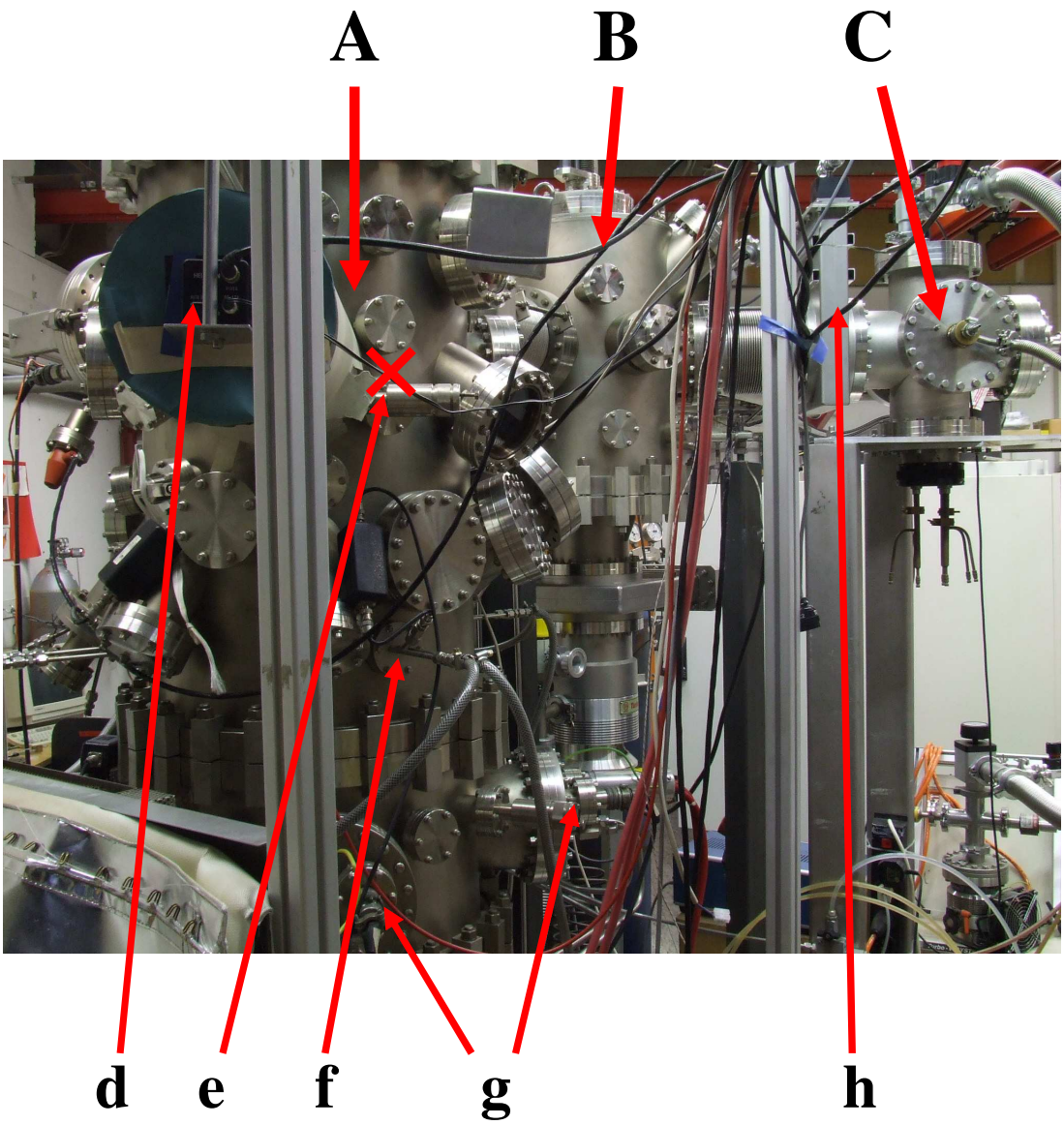

Figure 2.1: The Varian 450 picotorr MBE system. There are three parts: (A) deposition chamber, (B) transfer chamber and (C) junction preparation chamber. Exemplary features visible in the picture include: (d) RHEED system camera, (e) approximate substrate position inside the chamber during deposition, (f) oscillating crystal rate monitor (feedthrough), (g) electron beam evaporator connections and (h) gate valve between transfer and junction chamber.

2.1 UHV Deposition System

The samples for this work were prepared in the *Varian 450 picotorr* MBE vacuum system displayed in Figure 2.1, which comprises of three parts, separated by gate valves. These parts are the deposition chamber (A), the transfer chamber (B) and the junction preparation chamber (C). Manipulators allow to transfer substrates on a designated holder from one part to another without breaking the vacuum on the sample. After closing the gate valves, samples can be brought in and out of the system without venting the main deposition chamber.

Vacuum

The deposition chamber is pumped by a *Varian StarCell VacIon* iongetter pump which only operates at UHV conditions. With opened gate valve, additional pumping is provided by the turbomolecular and the roughing pump attached to the transfer chamber. After a bake-out procedure, in which the whole chamber is heated to stimulate outgassing of impurities adsorbed on the walls, a base pressure $p_{base} < 10^{-9} mbar$ is reached. However, during the deposition process the complete chamber is again heated by the electron beam evaporators and the substrate heating, reaching locally significant higher temperatures than during bake-out, and resulting in increased rest gas pressure. The deposition pressure can be improved by preoperating the sources at less than deposition power. After this typically $p_{depo} \approx 10^{-6} mbar$ was reached.

Electron Beam Evaporators

In the lower region of the deposition chamber, four electron beam evaporators (three *Leybold ESV 4* and one *Leybold ESV6*) are installed, which produce atomic beams by thermal evaporation. The working principle is to heat the evaporant by an high energetic electron beam (4 or 8 keV), which is guided by a magnetic field. The evaporant is placed in a liner to improve heat insulation against the water-cooled crucible and main block. Electrical contact between the material and the main block has to be ensured to avoid charging of the evaporant, which deflects the beam. While Uranium, Palladium and Nickel can be evaporated from conducting graphite liners, Aluminum, because of its high reactivity, requires a more inert material. Therefore, polycrystalline Al_2O_3 crucibles from the company *Degussa* under the trade name *Frialit* were used, after establishing an electrical

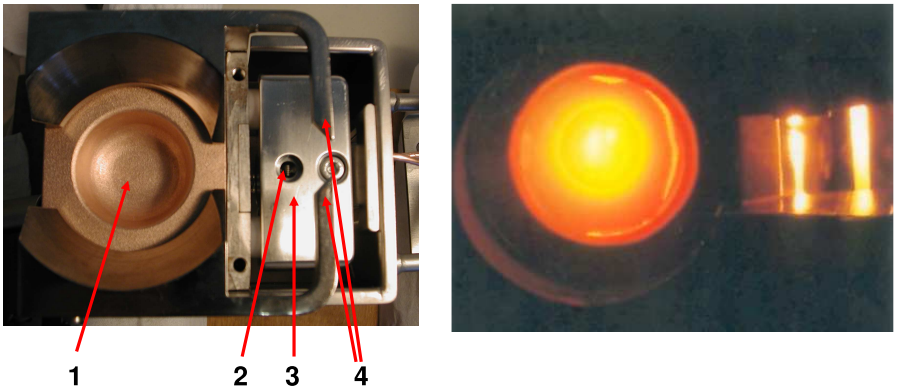

Figure 2.2: Electron beam evaporator: on the left in detail: (1) empty crucible (2) glow cathode for electron beam (3) accelerating anode (4) magnetic pole shoes for the guiding magnetic field; on the right in operation with well focused beam (right: photograph is courtesy of MBE-Komponenten GmbH).

contact through a cut by means of a Tungsten wire. Achieved deposition rates at the substrate location are of the order of 0.5Å/s with beam electrical power from 100W to 800W, depending both on the evaporant and the condition of the crucible liner. Careful beam adjustment is needed to ensure purity of the evaporated material. The electron beam should hit in the middle of the material and not heat the liner directly, otherwise additional graphite may be evaporated or alloyed into the evaporant. This was done manually by observing the beam position through a glass window in mirrors and adjusting the magnetic guiding field via the deflection coil current. Since the focus of the beam is considerably large (almost comparable to the liner size) and the deflection can be adjusted only in one (X) direction (for the *ESV 4*), not always a perfect position was accessible. The *Leybold ESV 6* installed during earlier work [87], proved a big advancement, both for its XY-deflection as well as the bigger crucible diameter.

As additional evaporation sources, the chamber allows the operation of two effusions cells, which were not used for this work.

Rate Monitoring

Evaporation rates were monitored and adjusted by means of four *Leybold XTC* oscillating crystal monitors. In these, small quartz crystals are oscillating and their resonance frequency is measured, which is a function of the mass deposited on them from the sources. Given the density of the material, the mass growth rate can be transformed into a thickness growth rate. Each crystal is placed exclu-

sively in the atomic beam of one evaporator, allowing independent measurement and control of the evaporation rate of each element. The electron beam currents of the evaporators are automatically adjusted by control units, stabilizing the desired rate. This does not allow absolute rate measurements, since the ad- and desorption probabilities of atoms are not the same on the water cooled crystals and the substrate. Instead, they strongly depend on the temperature (heated substrate) and adsorption coefficients, which are material specific. Also the distance between the source and the crystals differs from the one to the substrate, resulting in different rates of incoming atoms, due to the approximate point like character of the source. However, after rate calibration by X-ray reflectometry (see, e.g. [87]), the *XTC* monitors provide practical rate stabilization.

Substrate

The atomic beams of the evaporators converge in the upper part of the chamber. There, the thin film grows on the substrate, which is typically a small polished plate of an oxide like Al_2O_3 or $YAlO_3$. The substrate is mounted with silver paint on a substrate holder which is put with the transfer mechanism on a rotatable seating. The substrate holder can be heated by radiation from a filament to temperatures up to 1000°C. While the deposition temperature, depending on the film, is usually below that, before the deposition the substrate is heated and tempered for one hour at 1000°C. The temperature is measured with a thermoelement on the holder seating and directly with a pyrometer through a window of the chamber.

Further, a high energy electron gun and a fluorescent screen are installed in the upper part to perform Reflective High Energy Electron Diffraction (RHEED), which serves as online characterization method (please refer to Chapter 3).

Transfer and Junction Preparation Chamber

The transfer chamber is pumped by a *Varian V-300* turbomolecular and a roughing pump and functions as load lock. Through it, substrates and samples can be brought in and out of the system, without venting other parts. Attached are two rods, allowing transfer of the substrate holder into the deposition and the junction chamber. In the middle, a rotatable storage device is used to transfer the substrate holder from one rod to the other.

The junction chamber was used to prepare tunneling contacts fully in vacuum. It is pumped by an external turbomolecular pump, connected by a steel hose. In the bottom, two boat filaments are installed to evaporate e.g. Aluminum or Lead by resistive heating. There is one sputtering cathode on the side for depositing Silver or Aluminum and an oxidation cathode in the top. For the oxidation process, the chamber can be filled with a mixture of Oxygen and Argon from connected gas cylinders. The complete junction preparation will be described further below.

2.2 Deposition Process and Parameters

Before the thin film deposition, cut and polished substrates (supplied by *CrysTec GmbH* and *Crystal GmbH*) were cleaned in several steps in water, Acetone and Isopropanol in an ultrasonic bath. For cost reasons, also recycled substrates were used. In this case, used substrates were first lapped with a mixture of SiC and Al_2O_3, then fine polished with a alkaline SiO_2 colloidal suspension. Substrates were mounted with silver paint on the substrate holder and stored in rough vacuum while the paint solvent evaporated. After loading the substrate holder in the transfer chamber, this was pumped for at least one hour to keep the deposition chamber as free as possible from contamination. In the deposition chamber, the substrate was tempered for one hour at 1000°C to clean the surface from adsorbents and allow surface reconstruction. The electron beam evaporators were preheated to minimize the rest gas pressure during deposition, followed by predeposition time of approximately 5 min to remove any oxidized material from the crucible liners. Materials used for evaporation are:

- Uranium (purity 99.9%) purchased from *Goodfellow*,
- Palladium (99.95%) from *W. C. Heraeus*,
- Nickel (99.99%) supplied by *Advent Research Materials*,
- Aluminum (99.999%) also from *Advent Research Materials* and Aluminium (99.99%) from *Balzers*

Films between 200 and 2000 Å were deposited with an growth rate of 0.6 Å/s.

Optimization Process

The optimization process involved systematic variation of the substrate temperature and the relative evaporation rates with characterization of the resulting films. Several methods of characterization were employed, most prominently RHEED and X-ray diffraction, but also Rutherford backscattering spectroscopy (RBS) as well as temperature dependent resistivity measurements were included. Details and exemplary results of the characterization are given in the next chapter. On the substrate side, the search for an epitaxial substrate is most important, actually the finding of an epitaxial substrate is a prerequisite for the preparation of 3-dimensionally ordered thin films. This is explained extensively further below. Optimized deposition parameters are given in Table 2.1.

It has to be noted that the stoichiometry of the atomic beams at the substrate giving best results differs significantly from the nominal ratio of the compound, which is 1:2:3. The reason is that adsorbed atoms at the substrate have different probabilities to desorb again, depending on both, the atom type and the temperature. Another influence is the growth direction of the sample. While e.g. for UPd_2Al_3 (001) less Aluminum than the nominal content is needed, for UPd_2Al_3 (100) and UNi_2Al_3 (100) the Uranium rate has to be decreased.

Problems in optimizing the parameters were caused by a poor reproducibility. Wrong parameters always resulted in low quality films, but depositions with the optimized parameters did not always yield a good sample. Other, partially unknown parameters, like rest gas pressure, bad electron beam focusing and impurities in the liner (sometimes flakes peeling off and falling down from the inside roof of the chamber) are most likely the reason for this. Another critical point detected during this work is the dependence of the crystal oscillating monitor reading from the electron beam evaporator operating power. Especially the crystal controlling the Uranium evaporator, which requires high power levels, depending on the liner condition and fill level, showed sensitivity in this aspect. Variations in temperature of the crystal monitor are a possible reason, arising from radiative heating by the evaporator. The temperature will influence the ad- and desorption probability at the crystal and also the acoustic impedance of the system, resulting in substantial errors in rate control. Discrepancies of up to 50% (!) have been observed under extreme circumstances.

Film	Substrate	T_{thermo} (°C)	T_{pyro} (°C)	rel. evaporation rates[1] at monitors (U:Pd:Al)
UNi_2Al_3 (100)	$YAlO_3$ (112),(010)	860	750	1 : 2.62 : 4.33
UPd_2Al_3 (001)	$LaAlO_3$ (111)	710	605	1 : 1.95 : 2.5 (1 : 1.73 : 2.48)
UPd_2Al_3 (100)	$LaAlO_3$ (110)	750	640	1 : 2.5 : 3.61

Table 2.1: Optimized depositions parameters for UPd_2Al_3 and UNi_2Al_3 thin films used in this work. In the last column the atomic ratio is given, which deviates from the stoichiometric 1:2:3 (please refer to the text). The optimization for UNi_2Al_3 was done by *A. Zakharov* [97], values in the first line of UPd_2Al_3 (001) are from *M. Jourdan* [1], while the parameters for UPd_2Al_3 (100) are an outcome of this work. Values in brackets for UPd_2Al_3 (001) have been used in this work with good results. ([1]refer to Appendix A.1)

2.3 Epitaxial Growth and Substrate Choice

Usually the right ratio of incoming material of the constituting elements and a suited substrate temperature is sufficient to stimulate growth of the wanted microscopic crystals structure. Additional temper steps may help to improve the microscopic order. Up to this point, only two requirements are made on the substrate: It should be chemically inert to avoid alloying or diffusion into the film and it should be polished smooth enough to allow the growth of a homogeneous, flat film. Further, to investigate the properties of the film, e.g. the resistivity, insulating substrates are needed. These demands are met by a wide range of crystalline metal oxides like Al_2O_3, $SrTiO_3$, MgO and many more.

But, as mentioned before, to fully exploit the opportunities of thin film samples, a macroscopic order of the crystallographic axes in the sample is also needed. For this, the substrate-film interaction plays a crucial role. To understand how the substrate can induce long range crystalline order in a thin film, some simple considerations can lead to qualitative understanding.

In principle three different growth modes are possible for thin films: layer growth, island growth and Stranski-Krastanov growth which can be described as island growth on a mono layer. Atomic force microscopy (AFM) investigations reveal island morphology of UPd_2Al_3 and UNi_2Al_3 films (see Figure 2.3) and show that layer growth is not realized in the parameter range of this work. Relevant parameters that favor the island forming growth modes are the high growth

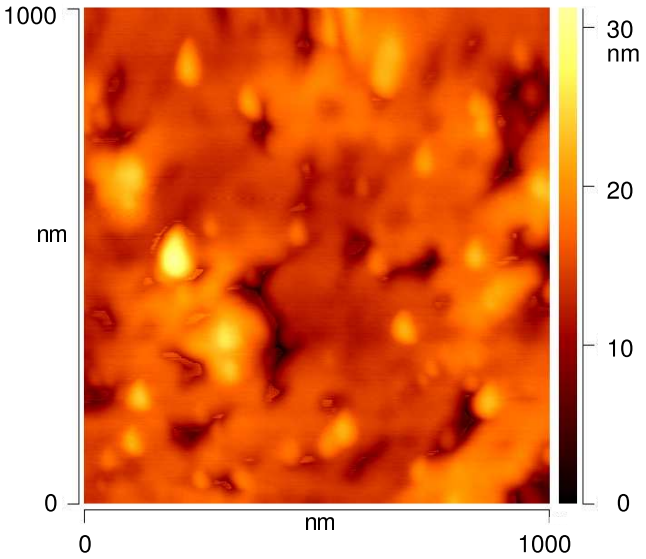

Figure 2.3: Topography of a UPd_2Al_3 (100) thin film measured by AFM consisting of coascelented islands. Total film thickness is around 100nm.

rate and the comparatively low (with reference to the melting point) substrate temperature, resulting in a small mobility of adatoms on the surface.

To obtain a macroscopically ordered sample, the islands should have the same 3-dimensional crystallographic orientation already before they grow together, forming the film. Three cases of order can be distinguished in the crystal growth process (compare Figure 2.4). If the islands are completely randomly oriented, a polycrystalline sample is obtained (A). However, the out-of-plane crystallographic axis is often determined by an intrinsically preferred growth direction, which is a property of the material, resulting from bond enthalpies and specific surface energies of different possible directions. In this case, most parts of the film will have the same crystal axis perpendicular to the film orientation and the film is *layered* (B) (sometimes also referred to as textured).

When the substrate defines a preferred 3-dimensional orientation of the islands, a 3-dimensionally ordered, *epitaxial* film will grow (C). Preferred in-plane orientation occurs often when a lattice constant of the film nearly matches one of the in-plane constants of the substrate. The similar periodicity of film and substrate allows to place many film atoms in positions of maximal binding energy, no matter where this position actually is, since there will always be one. The subsequent layers will then follow the orientation given by the first one. However, it should be noted that even a complete 3-dimensional order does not imply

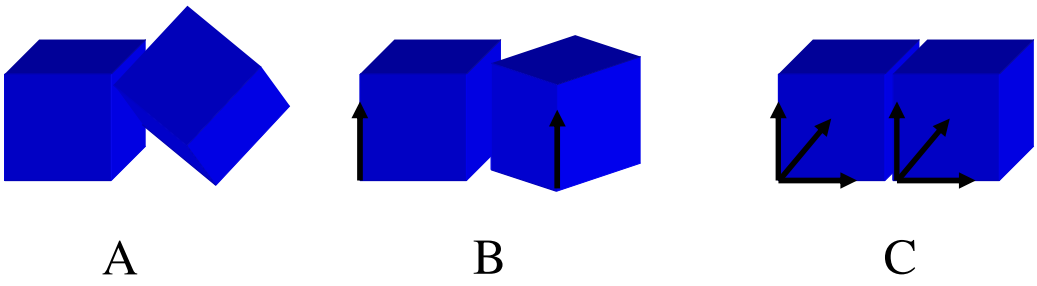

Figure 2.4: Schematic representation of: (A) polycrystalline, (B) layered, (C) epitaxial order. Alligned crystal axes are represented by arrows

monocrystallicity in thin films. The mechanisms that cause dislocations include steps on the substrate surface whose height does not fit with the film material and the eventual relaxation of an accumulated lattice mismatch. Instead of being one big single crystal, the sample rather consists of equally oriented parts.

A more detailed understanding of the substrate-film interaction is difficult for several reasons: it is a priori neither clear which of the different possible atomic layers of the substrate will form the interface nor if the surface is indeed oriented in the macroscopic cutting direction. If there are different crystal planes of minimum energy, facets or terrace structures will be formed instead. The former was reported e.g. for Al_2O_3 (100) (sapphire m-plane), where after high temperature annealing facets in the range of 100nm in lateral dimensions are observed [88]. Another example for surface reconstruction, is the 7x7 reconstruction on Si (111) [89]. Also on the film side is not clear which atomic layer will be at the interface. Additionally the microscopic interactions at the (unknown) interface are not to be understood in simple terms, i.e. it is unclear which neighboring atom will be favored or disfavored. Further, the interaction will surely include more than just the top layer.[2]

In general the surface structure of a crystal may differ significantly from the volume structure, but the surface periodicity is usually a multiple of the volume one [90], keeping the basic explanation valid. It should be noted, that a close match of lattice constants is not always sufficient to trigger epitaxial growth, but rather serves as an explanation of experimentally found facts. Predictions based upon lattice constants are rather a guess, and one is limited to trial and error.

[2]One experimental technique that in principle can give insight into details at the interface is Transmission Electron Microscopy (TEM) with atomic resolution.

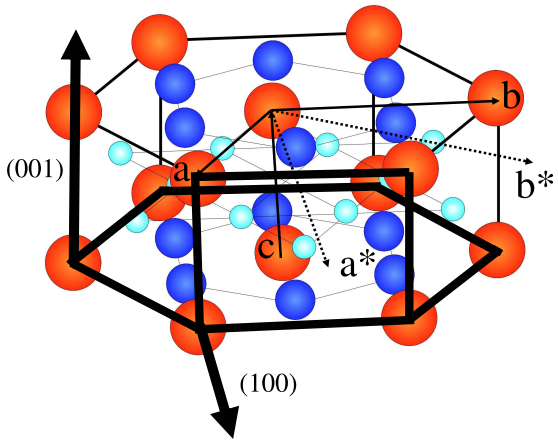

Figure 2.5: Different crystal planes in the hexagonal $U(Ni,Pd)_2Al_3$ structure. The in-plane symmetry of (001) is hexagonal, while for (100) results a rectangular symmetry.

Epitaxial Growth of UPd_2Al_3 and UNi_2Al_3

Remarkably, different intrinsic growth directions have been observed for the isostructural compounds UNi_2Al_3 and UPd_2Al_3, e.g. on Al_2O_3 cut in an non-symmetry direction (sapphire random cut), UPd_2Al_3 grows in (001) direction, i.e. with the crystallographic c-axis of the hexagonal unit cell perpendicular to the film surface. Thus, the in-plane symmetry is hexagonal with a lattice constant of $a = b = 5.365$Å. For UNi_2Al_3 (100), the c-axis is oriented in-plane, while the reciprocal a^*-vector is perpendicular to the surface. Consequently, the in-plane structure consists of the b and the c-axis including a 90° angle (compare Figure 2.5).

Based on this, several substrates with small lattice mismatches in the appropriate cutting directions had been tried, amongst others Al_2O_3, $YAlO_3$, $LaAlO_3$, $MgAl_2O_4$, ZnO and $LiAlO_2$. Epitaxial growth in the intrinsic growth direction was found, for UPd_2Al_3 (001) on $LaAlO_3$ (111) [92] and for UNi_2Al_3 (100) on both $YAlO_3$ (010) and (112) [93]. The corresponding in-plane order was proved by 4-circle X-ray diffraction, which will be discussed for other cases in detail in the next chapter.

The rhombohedral crystal structure of $LaAlO_3$ is most conveniently described by a pseudo cubic cell with $a = b = c = 3.79$Åand $\alpha = \beta = \gamma = 90.9°$ [91]. $LaAlO_3$ undergoes a phase transition to the cubic perovskite structure at around 800K, so at deposition temperature the structure is cubic. [3] From the (111)

[3]Due to the strain associated to the phase transition, in the low temperature rhombohedral phase of $LaAlO_3$, (010) twins occur.

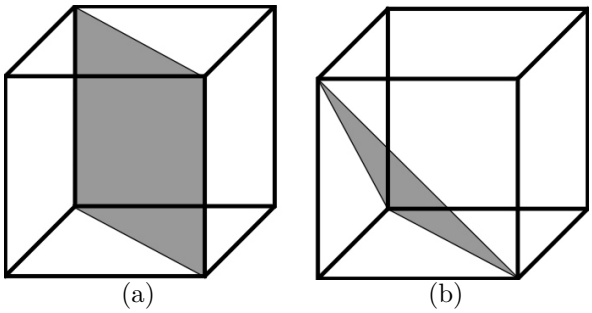

Figure 2.6: Different crystal planes in a cubic system: (a) (110) plane, with rectangular symmetry. (b) (111) plane with hexagonal symmetry (only a triangle is shown).

cut (compare Figure 2.6(b)), and approximating $\alpha \approx 90^o$, results a hexagonal in-plane symmetry with lattice constant $a' = \sqrt{2}a = 5.360$Å, that fits the ab-plane of UPd_2Al_3 good enough to induce epitaxial oriented (100) growth. The mismatch $(a_{UPA} - a')/a' \approx 0.1\%$ is quite small[4].

For the orthorhombic $YAlO_3$ ($a = 5.1790$Å, $b = 5.330$Å, $c = 7.370$Å [94]) cut in (010) direction, the in-plane symmetry is rectangular with a small mismatch $(a_{UNA} - a_{YAO})/a_{YAO} \approx 0.5\%$ in one direction, fitting to the ac-plane of UNi_2Al_3 which also posesses rectangluar symmetry. In this case, a near match of the lattice constants in only one direction is sufficient to induce epitaxial growth, since in the orthogonal direction lattice parameters are significantly different.

A similar situation is found on $YAlO_3$ (112), where the length of the (almost orthogonal: ϕ=91.6°) in-plane vectors $[1\overline{1}0]$ and $[11\overline{1}]$ are 7.432Å and 10.467Å respectively, resulting in mismatch of about $\left(2a_{UNA} - |[11\overline{1}]_{YAO}|\right)/|[11\overline{1}]_{YAO}| \approx 0.5\%$.

Comparison

To discuss the similarities of the two different cutting directions of $YAlO_3$ and compare this with UPd_2Al_3 on $LaAlO_3$, it is useful to introduce another, monoclinic pseudo cell for $YAlO_3$. It derives from the cubic perovskite structure through distortion: $a = c = 3.716$Å, $b = 3.685$Å, $\alpha = \gamma = 90^o$, $\beta = 91.6^o$ and thus is very similar to $LaAlO_3$, only with a slightly smaller lattice constants. If one neglects the distortion, the cell can be approximated by a cubic one, with the following relations:

$$[100]_{orth} \leftrightarrow [110]_{cub}$$

[4]For the lattice mismatch, always values at room temperature are compared

crystal	cell	a [Å]	b [Å]	c [Å]	α[°]	β[°]	γ[°]
$LaAlO_3$	rhombohedral	5.357	5.357	5.357	60.06	60.06	60.06
<800K	pseudo cubic	3.790	3.790	3.790	90.09	90.09	90.09
$LaAlO_3$	cubic	3.811	3.811	3.811	90	90	90
>850K							
$YAlO_3$	orthorhombic	5.179	5.330	7.370	90	90	90
	pseudo cubic	3.716	3.685	3.716	90	91.6	90
UPd_2Al_3	hexagonal	5.365	5.365	4.186	90	90	120
UNi_2Al_3	hexagonal	5.207	5.207	4.018	90	90	120

Table 2.2: Overview of relevant crystal structure data [95, 91, 94]. The difference in the lattice constants for the two $LaAlO_3$ phases is not due to the phase transition, but thermal expansion between room temperature and 850K.

$$[010]_{orth} \leftrightarrow [\bar{1}10]_{cub}$$
$$[001]_{orth} \leftrightarrow [002]_{cub}$$

In this approximated cubic cell, $(010)_{orth}$ and $(112)_{orth}$ are both equivalent to $(110)_{cub}$. This is shown in Tab.2.3, where the surface structure of selected substrates is summarized in both systems (where appropriate).

It should be noted that for UNi_2Al_3 on $YAlO_3$ (112) and (010) as well as for UPd_2Al_3 (001) on $LaAlO_3$ (111), always an in-plane $a(\equiv b)$-axis is parallel to an equivalent of (pseudo)cubic [110]. The misfit of the lattice constants is comparatively small, with $YAlO_3$ fitting the Nickel compound while $LaAlO_3$ fits with the Palladium compound. The cutting direction of the substrate defines the second in-plane vector and therefore the in-plane symmetry. For $LaAlO_3$ (111) the second in-plane vector is also of the [110] type, including an 60° angle and matching the hexagonal ab-plane of UPd_2Al_3. In the case of $YAlO_3$ $(112)_{orth} \approx (010)_{orth} \approx (110)_{cub}$, the other in-plane vector is [001], including an 90° angle and fitting with the rectangular ac-plane of UNi_2Al_3.

Changing the Growth Direction

Since different intrinsic growth directions are observed in crystallographic similar systems, it may be concluded that both directions are energetically comparable and the favor for one or the other is not very strong. This, and the above analysis

Substrate	in-plane vectors$_{orth}$	in-plane vectors$_{cub}$	orien-tation$_{cub}$	sym.	in-plane constants [Å]
$LaAlO_3$ (111)	-	$[1\overline{1}0]$; $[10\overline{1}]$ $[01\overline{1}]$		hex.	5.360
$LaAlO_3$ (110)	-	[001] $[1\overline{1}0]$		rect.	3.790 5.360
$YAlO_3$ (010)	[100] [001]	[110] [002]	$(1\overline{1}0)$ $\equiv(110)$	rect.	5.179 7.370
$YAlO_3$ (112)	$[1\overline{1}0]$ $[11\overline{1}]$	[200] $[02\overline{2}]$	(011) $\equiv(110)$	$\sim$ *rect.*	7.432 10.467
$YAlO_3$ (101)	[010] $[11\overline{1}]$; $[1\overline{11}]$	$[\overline{1}10]$ $[02\overline{2}]$; $[20\overline{2}]$	(111)	$\sim$ *hex.*	5.330 10.467

Table 2.3: In-plane vectors of selected substrates. Lattice constants are calculated for room temperature, for $LaAlO_3$ approximating cubic symmetry. For $YAlO_3$, the lattice constants are determined using the correct orthorhombic cell, while the approximated symmetry is easier seen in the pseudo cubic system.

gave rise to the assumption [87], that epitaxial films in other than the intrinsic growth direction may be grown using appropriately oriented substrates. Therefore, UPd_2Al_3 films were deposited on $LaAlO_3$ (110) in analogy to the situation for UNi_2Al_3 on $YAlO_3$. Indeed epitaxial UPd_2Al_3 (100) films can be prepared, for which optimized deposition parameters were determined in this work (Table 2.1). The influence of the growth direction on the film stoichiometry is remarkably strong, as the optimized evaporation rates differ significantly for UPd_2Al_3 (001) from the ones of UPd_2Al_3 (100). This was confirmed by Rutherford backscattering (RBS) results which are given in the next chapter.

Since for (100) directed growth the in-plane axes are given by the a and the c-vector, such films offer excellent opportunities to investigate the anisotropic transport properties, for all angles between (100) and (001). For these directions much bigger anisotropy can be expected than in the ab-plane, where for the hexagonal symmetry only weak anisotropy is expected. These results may be viewed in connection with the Fermi surface topology, since there exist quasi 2-dimensional parts around the c-axis. Further, based on these films tunneling spectroscopy may be performed in a-direction, e.g. giving valuable information

about the superconducting gap symmetry (together with the results on c-axis tunneling [20]).

Correspondingly, also for UNi_2Al_3 the growth direction can be changed by the use of $YAlO_3$ $(011)_{orth}$ substrates, equivalent to the pseudo cubic $(111)_{cub}$. Optimized deposition parameters still need to be determined, however, it is reasonable to expect similarities with the situation for UPd_2Al_3, i.e. a smaller Uranium evaporation rate for (001) growth compared to (100). Experimental use of the (001) samples seems more limited than for (100), still they offer additional possibilities for future investigations, e.g. tunneling spectroscopy in c-axis direction.

Summarizing the epitaxial growth of $U(Ni,Pd)_2Al_3$ on $(Y,La)AlO_3$, it is remarkable that by the use of an appropriate substrate orientation, differently oriented films can be deposited for both compounds. However, the situation does not represent a 3-dimensional epitaxy relation like observed e.g. for Nb on Al_2O_3 [96], where the relative orientation of film and substrate is always the same. For $U(Ni,Pd)_2Al_3$ on $(Y,La)AlO_3$, instead one in-plane vector is fixed by the small lattice mismatch, while the substrate symmetry favors one or the other growth direction. While for (001) oriented growth, all in-plane directions have a small mismatch, in the case of (100) growth there is no fitting periodicity in the second direction. Thus epitaxial substrates for both compounds are available in two growth directions. The ideal growth conditions, i.e. the relative evaporation rates, can vary significantly for different orientations.

2.4 Lithography

Thin film samples were patterned by standard optical lithography to measure direction dependent transport properties. For this, the film is homogeneously coated with a photoresist, then baked to harden the resist. Then the sample is covered by a mask defining the geometry, and exposed to UV light from an Hg vapor lamp. Where exposed, the resist is chemically solved in a developer (diluted NaOH). In the subsequent ion beam etching step all of the film is removed except for the parts where it is still covered by remaining, not exposed photo resist. The complete lithography process is performed in a class 100 clean room, to guarantee constant conditions (temperature, humidity) and to avoid pollution by small dust particles. An exemplary measurement geometry is shown in Figure 2.7, while the detailed lithography parameters are given in Appendix A.3 .

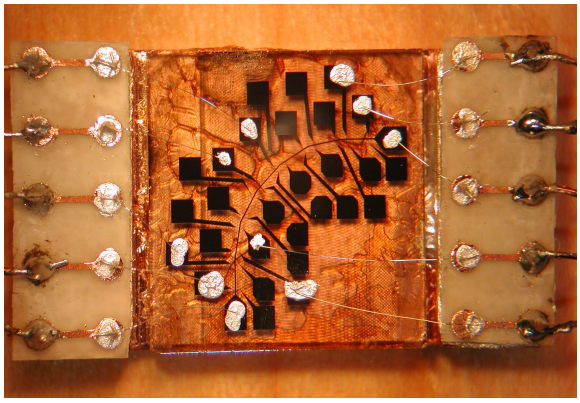

Figure 2.7: Patterned UNi_2Al_3 thin film for resistivity and Hall effect measurements, mounted on a cryostat sample holder and contacted.

2.5 Junction Preparation

An overview over the preparation and characteristics of different planar tunneling junction types is given e.g. in [97]. In this section only the preparation of mesa tunneling junctions, as used in this work, will be sketched. Mesa tunneling junctions have proved to combine high reliability and good compatibility with the thin film deposition as well as comparatively easy processing [98, 97].

First step in preparing a mesa tunnel junction is the deposition of a stack comprising of the desired contact on the complete substrate. The heavy fermion compound (UNi_2Al_3 or UPd_2Al_3) is deposited on the substrate in the deposition chamber, typical thickness is $d \approx 900$Å. After slowly (around 1 hour) cooling down from the deposition temperature to 100°C, a thin Aluminum layer, typically 40-60Å, is deposited with an electron beam evaporator. Then the sample is transfered to the junction preparation chamber. The chamber is filled with a mixture of 0.4 mbar Oxygen and 0.4 mbar Argon from attached high purity gas cylinders. By applying high voltage ($U \approx -300$V) to the oxidation cathode, a plasma discharge in the gas is started. The oxidation cathode simply is a cylinder made of Aluminum, opposite of an earthed aluminum plate, which stabilizes the plasma. Through the plasma discharge the reactivity of the Oxygen is increased, to ensure complete and homogeneous oxidation of the Aluminum layer, forming the tunneling barrier. Oxidation time was 60-90s with a plasma current of 10mA. Subsequently, the junction preparation chamber is pumped down and partially refilled with Argon (0.15 mbar) for the following sputtering process. As final layer, the counter electrode, typically 2000Å Silver is sputtered onto the barrier.

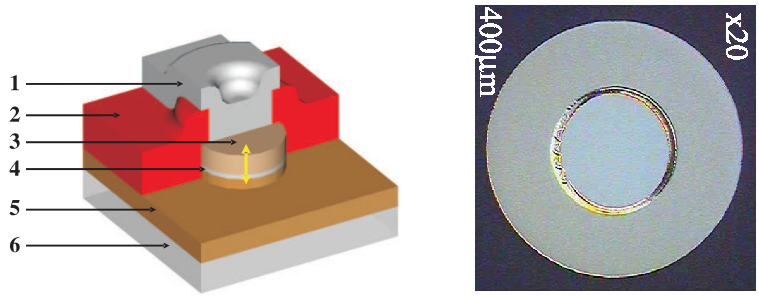

(a) (b)

Figure 2.8: (a) Schematic drawing of a mesa structure (courtesy of A. Zakharov): (1) silver paint top contact, (2) negative photoresist, insulating, (3) top silver electrode, (4) AlO_x tunneling barrier (5) $U(Ni,Pd)_2Al_3$ ground electrode, (6) substrate; current direction is along the yellow arrow (b) mesa structure with negative photoresist and opened window, top view from a optical microscope.

Thus, the whole $U(Pd,Ni)_2Al_3$-AlO_x-Ag stack is fabricated in vacuum to assure clean interfaces. Complete technical details are given in the Appendix A.2 .

In the second step, the sample is patterned by optical lithography in the way described above, only the etching is stopped after the top silver electrode and the AlO_xtunneling barrier have been removed. The structure consists of six columns, two with diameter 600μm, 400μm and 200μm (or 400μm, 200μm and 100μm) respectively. After cleaning the sample from remaining resist with Acetone, it is covered with a negative[5] photoresist, that is sturdy and functions as electric insulation in the finished device. From this layer, small windows (400μm, 200μm and 100μm or 200μm, 100μm and 50μm) in the center of the columns and contact pads to the base electrode are removed (again the complete process parameters can be found in the Appendix, section A.4). By attaching small copper wires with silver paint on the top of the columns and on the contact pads, a current can be sent through the mesa stack, effectively measuring the conductivity of the $U(Pd,Ni)_2Al_3$-AlO_x-Ag tunneling junction. This constitutes a three point contact measurement, since only one wire is connected to the silver top electrode for spatial reasons, while two separate wires are attached to the ground electrode. However, because the resistance of such a small contact in the tunneling regime ($R \sim$kΩ) clearly dominates over the small wire and the silver paint contact resistance ($R \sim \Omega$), this disadvantage is considered acceptable.

[5]When a negative photoresist is used, the parts not exposed to UV light will be removed in the developing step and hence the remaining photoresist is the negative of the mask that was employed.

Chapter 3

Characterization

Characterizations of prepared thin film samples serve two main purposes: First, information about the crystalline quality of the samples is needed for the optimization of the deposition process as described in the previous chapter. This is done mainly by X-ray diffraction, which provides information about the degree of microscopic order, the distribution of the crystallografic orientation and potential lattice strain.

Second, it has to be assured that the prepared samples are indeed representative for the compound, in particular that the electronic properties are not strongly influenced by perturbations like lattice imperfections, impurities or strain. Here, the first approach is to compare the temperature dependent electrical resistivity with the known characteristics of high quality bulk single crystals. Especially the occurrence of superconductivity and a value of the critical temperature T_c close to the bulk values, is seen as an indication of typical electronic behavior and high crystalline quality, since the formation of *Cooper pairs* is extremely sensitive to scattering on lattice imperfections. Additionally, the existence of magnetic order can be proved by neutron scattering or resonant magnetic X-ray scattering.

To some extend, the boundaries between characterization and new investigations overlap, since the properties of a new kind of sample may be regarded as new results per se. In addition, already existing material specific data e.g. for bulk samples can be accompanied by more precise thin film methods.

While the methods introduced here are exemplary for all investigated samples (and thin film preparation in general), the focus in the results presented is on UPd_2Al_3 (100), since extensive description for UPd_2Al_3 (001) and UNi_2Al_3 (100) already exist elsewhere [20, 97]. Another reason is that establishing the

preparation of UPd_2Al_3 (100) thin film samples was one of the objectives of this work.

3.1 RHEED

Reflection high energy electron diffraction (RHEED) provides in-situ information of the sample's surface structure during the deposition process. This is a unique possibility in the sense that information about the sample structure is obtained during deposition and therefore the influence of changes in the deposition conditions may be directly observed. The RHEED system comprises of an electron gun (E=10keV), mounted in a small angle of incidence ($\alpha \sim 1^o$) to the sample and a photoluminescent screen converting incident electrons into visible light. The RHEED pattern on the screen may be observed by eye or more conveniently with a CCD camera, which also allows recording.

Because of the small angle of incidence, RHEED is very surface sensitive and samples only the first few atomic layers. Consequently, the diffraction problem can be approximated in two dimensions. The reciprocal lattice of a two dimensional ordered structure consists of continuous rods, perpendicular to the surface. Reflections will be observed where the rods intersects the Ewald sphere, implying elastic scattering. As illustrated in Figure 3.1, one obtains several sets (*orders*) of reflections, which are arranged on rings with different diameters on the screen.

While the diameter of the rods is zero for a perfect, infinite crystal, it is determined by the in-plane correlation length for a real sample and therefore is finite. The in-plane correlation length is limited by the crystallite's grain size and tilt with respect to each other, crystal defects and thermal lattice vibrations, as well as the energy width of the beam. Since for 10keV electrons the Ewald sphere is almost flat ($k = 512\text{nm}^{-1}$) compared to the reciprocal lattice dimensions ($\sim 1\text{nm}^{-1}$), the intersections of the extended reciprocal rods with the Ewald sphere become streaks instead of points. Further broadening may appear due electron energy loss in the sample, mainly by plasmon excitation, resulting in a finite width of the Ewald sphere. Extensive information about RHEED during crystal growth may be found e.g. in Ref. [99].

Although not used quantitatively, RHHED observations played an important role in the optimization of the deposition process. The existence of a diffraction pattern like in Figure 3.2 indicates good crystalline quality of the sample. In contrast, if the surface of the sample is not ordered, only a diffusive background

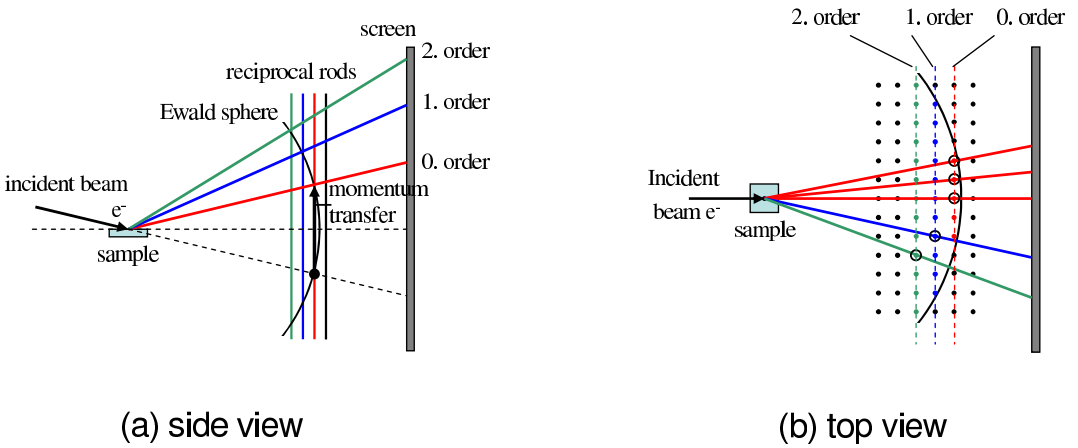

Figure 3.1: Schematics of RHEED seen from the side (a) and top (b). Maxima of intensity are determined by intersections of the three dimensional Ewald sphere with the reciprocal rods. The arrangement of the maxima on distinct rings is given by summarizing rods in planes with different distance to the center of the Ewald sphere. (For clarity the radius of the Ewald sphere is strongly reduced in these figures.)

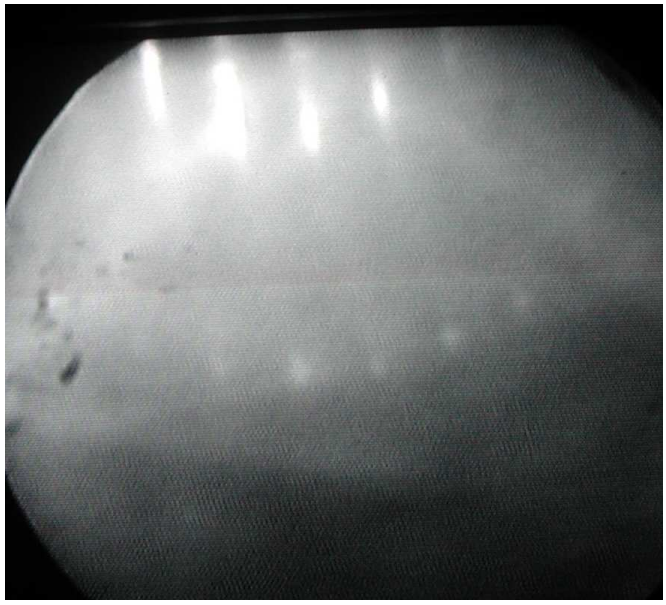

Figure 3.2: RHEED pattern of an UPd_2Al_3 (100) thin film directly after deposition (Nr.71). The reflections are of 0th (inner) and 1st order (weak, outer ring).

is observed. For more detailed structural investigations including the complete sample volume, X-ray diffraction was employed, which will be discussed later.

3.2 Morphology

UPd_2Al_3 thin film morphologies obtained on $LaAlO_3$ (110) substrates were observed by means of an Atomic Force Microscope (AFM). The topography of a superconducting sample is shown in the previous chapter (Figure 2.3). The film consist of coascelented islands with a relatively rough surface. The film roughness, in the order of 10-20nm (total thickness around 100nm) is bigger than for UPd_2Al_3 (001) oriented films, but smaller than for equivalent UNi_2Al_3 (100) samples.

3.3 Rutherford Backscattering Spectroscopy

As mentioned in the last chapter, the sample stoichiometry is not simply given by the relative evaporation rates. Thus, the determination of the sample composition is desirable for the optimization process. However, quantitative analysis methods for thin films were not available as standard technology[1]. Therefore, Rutherford Backscattering Spectroscopy (RBS) was performed at the 7 MeV van-der-Graaf accelerator of the University of Frankfurt. For this, the sample was placed in a high energetic beam (E_0=1.6 MeV) of He-ions and the energy of backscattered (backscattering angle 171°) He-ions was resolved in a surface barrier detector with an energy resolution of $FWHM = 25$keV.

Physical Principles and Spectra Characteristics

The basic physical ingredients to understand RBS spectra are:

- The scattering of the He-ion on the target nucleus can be treated as elastic two body collision since the coulomb repulsion is not overcome in this energy range. Therefore, the energy loss of the projectile by the backscattering

[1] A standard analysis technique that was available, but in this case is not applicable, is Energy Dispersive X-ray spectroscopy (EDX). For this, inner shell excitations are created in the sample by an high energetic electron beam and element specific X-ray radiation is observed. However, quantitative analysis of thin films is not possible when substrate and film have common elements.

process is simply given by energy and momentum conservation. It can be expressed by the kinematic factor k, which solely depends on the projectile mass M_1, target mass M_2 and the scattering angle θ:

$$k = \frac{E_1}{E} = \left[\frac{(M_2^2 - M_1^2 sin^2\theta)^{1/2} + M_1 cos\theta}{M_1 + M_2}\right]^2$$

where E (E_1) is the projectile's energy before (after) the collision. The M_2-dependence of k allows target mass identification and thus sample composition analysis.

- For calculating the sample composition from the number of scattered He-ions with a given energy, the element specific scattering cross section has to be taken into account. In the case of the Coulomb interaction it is given by the Rutherford cross section in the laboratory frame of reference:

$$\frac{d\sigma}{d\Omega} = \left(\frac{Z_1 Z_2 e^2}{16\pi\epsilon_0 E}\right)^2 \frac{4}{sin^4\theta} \frac{\left\{\left[1 - \left((M_1/M_2)\, sin\theta\right)^2\right]^{1/2} + cos\theta\right\}^2}{\left[1 - \left((M_1/M_2)\, sin\theta\right)^2\right]^{1/2}}$$

  with the projectile and target atomic numbers Z_1, Z_2 and E the energy of the projectile immediately before scattering. From the first factor, the cross section increases with decreasing energy.

- Further, the projectile loses energy ΔE on the distance Δx travelled through the target before and after the backscattering event, which allows depth perception of the sample. The specific energy loss $dE/dx(E) = lim_{\Delta x \to 0} \frac{\Delta E}{\Delta x}$ depends on the projectile's energy as well as the projectile and target composition. On this point, the necessary input for data analysis and simulation is taken from semi empirical tables, since theoretical calculations (e.g. the Bethe-Bloch formula) of the stopping cross section $\epsilon = (1/N)(dE/dx)$ (with N the target atomic density) prove to be not accurate enough.

- The statistical nature of the energy loss dE/dx upon passing the sample smears out the He-beam energy distribution. This process is called energy straggling and limits (amongst others) the mass and depth resolution of the experiment.

For a detailed discussion of the RBS method please refer to Ref. [100]. From the above mentioned points, the following characteristics are expected for an RBS spectrum (He-ion counts vs. energy) of a film with finite thickness:

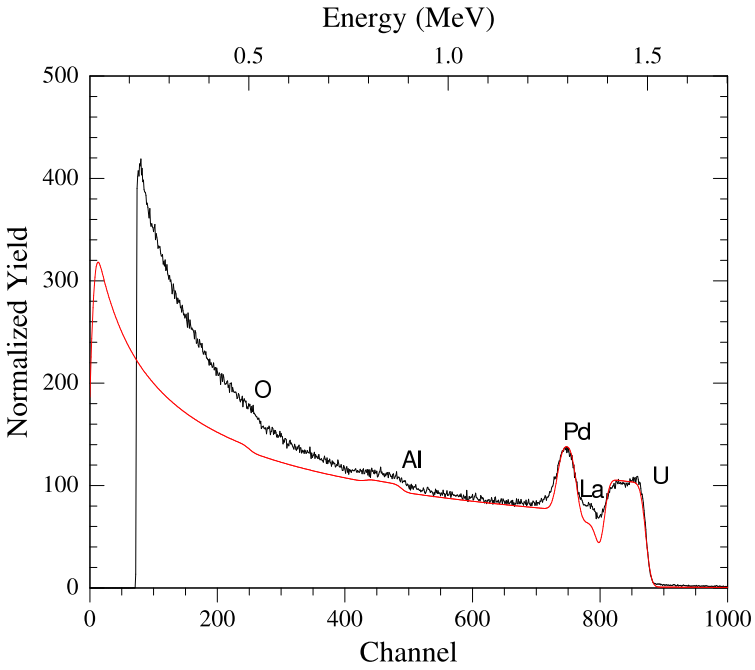

Figure 3.3: RBS spectrum of an UPd_2Al_3 film in (001) growth direction on a $LaAlO_3$ (111) substrate. The red line corresponds to a simulation with the RUMP software.

- Each element (or more precise: atomic mass) backscatters with an characteristic energy at the film surface.
- Scattering events inside the sample result in a smaller energy, since the particles lose energy while passing the sample. Thus, the energy scale becomes a depth scale for scattering on a specified atomic mass.
- For constant target concentration, the count rate increases with depth, because of the increase of the cross section with decreasing energy.
- Light elements will produce small count rates, since the cross section depends on $(Z_2)^2$.

Results

A RBS spectrum obtained on a UPd_2Al_3 film is shown in Figure 3.3. Characteristic steps at positions corresponding to the energy for backscattering at certain elements (on the surface and on the substrate) are visible. The energy scale of the detector is calibrated by using the positions of the steps for U and Pd. For comparison, a simulated spectrum obtained by the RBS simulation software

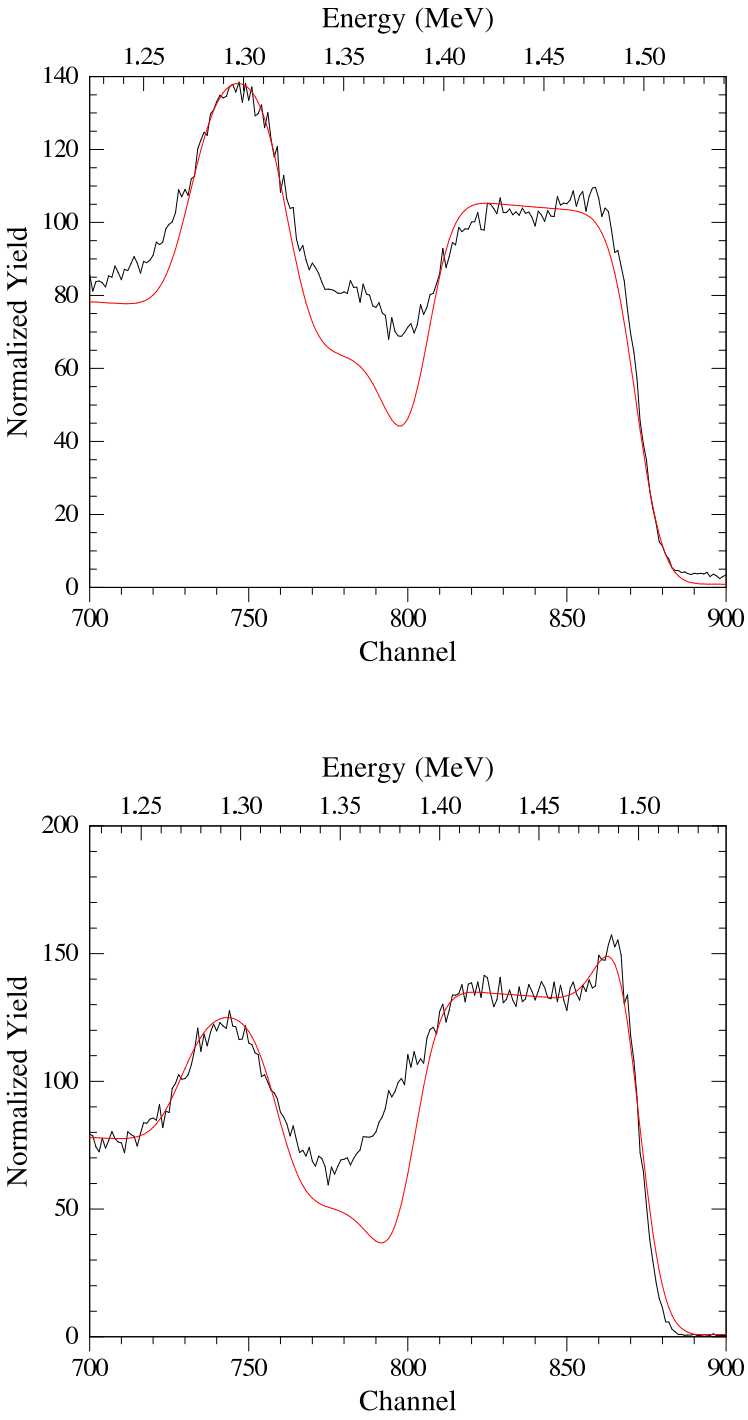

Figure 3.4: Details of the RBS spectra of two UPd_2Al_3 films, grown simultaneously in different growth directions. Top: On $LaAlO_3$ (111), resulting in (001) oriented growth. Below: On $LaAlO_3$ (110), resulting in (100) oriented growth. The red lines correspond to simulations with the RUMP software. Please refer to text for detailed explanation.

Sample:	UPA112 (001)	Fig.3.3(b)	UPA 112 (100)	Fig.3.3(c)
Layer	Composition	Thickness	Composition	Thickness
1	-	-	U	40Å
2	U:Pd:Al 1:2.35:3	1050Å	U:Pd:Al 1:1.45:2.5	1050Å
3	La:Al:O 1:1:3	∞	La:Al:O 1:1:3	∞

Table 3.1: Parameters used for the simulation of RBS spectra.

RUMP [101] is shown in red. Practical restrictions of the method, as employed here, become clear: First, the scattering in greater depth on the substrate is not well described. The most likely reason is a mistake in the beam energy loss in the sample in the simulation, which uses a superposition of elemental stopping powers. Second, the superposition of scattering from different elements from different depths, like in the example for La (in the substrate) and Pd (in the film), complicates quantitative analysis. Further, analysis for a light element like Al is limited by the small scattering cross section. On the contrary, a more reliable information about the U/Pd ratio can be obtained from the relative heights of the elemental peaks.

In Figure 3.4, details of the RBS spectra of two UPd_2Al_3 films are shown. Both films were deposited simultaneously on $LaAlO_3$ substrates, cut in (111) and (110) direction, resulting in (001) and (100) oriented growth respectively. The observed scattering intensity ratio for U and Pd is clearly different. In the last spectra an additional peak appears at the U edge, indicating a thin U rich top layer, which may be formed as segregation during the growth process.

Again, simulated spectra (red) were calculated using the RUMP software. They agree reasonable well with the measured data in the region of interest. For the simulation, the sample composition given in Table 3.1 was assumed:

While it cannot be claimed that the given values represent accurately the real U:Pd ratios in the samples, a clear difference in the film composition becomes evident, depending on the growth direction for otherwise identical deposition parameters. This confirms the (surprisingly) big difference in the deposition parameters for different growth directions as given in Table 2.1, which are the result of optimization by X-Ray diffraction and transport measurements. Further,

evidence for an actual difference in the sample composition is provided, since the existence of segregations in form of not ordered impurities cannot be excluded by the other employed methods.

3.4 X-ray Diffraction

X-ray diffraction (XRD) in various forms play a central role in thin film sample characterization. The methods discussed here concern investigations of the crystal structure, sample homogeneity, possible crystalline impurities, orientation of the crystal with respect to the substrate and thickness determination by reflectometry. Measurements were performed on a *Philips X'pert-MPD* two-circle diffractometer and a four-circle diffractometer equipped with a *Nonius* rotating anode and a *Stoe* goniometer in Eulerian cradle configuration. Both devices employ Cu-K$_\alpha$ radiation with wavelengths $\lambda_{K_{\alpha_1}} = 1.5406$Å and $\lambda_{K_{\alpha_2}} = 1.5444$Å respectively.

Diffraction Condition

In XRD, the incoming and the outgoing beam define a plane, in which the momentum transfer of an diffracted X-ray photon lies. The condition for the observation of diffracted intensity on a periodic structure (constructive interference) is that the X-ray photon momentum transfer $\Delta\vec{k}$ must equal a reciprocal lattice vector $\vec{G}$:

$$\Delta\vec{k} = \vec{G}$$

Considering the scattering on equivalent parallel planes (orthogonal to the momentum transfer) this takes the well known form of Bragg's law:

$$2dsin\theta = n\lambda$$

where d is the distance of neighboring planes, θ the incoming angle with respect to the surface, n an arbitrary integer number and λ the X-ray wave length.

Measurement Geometries

In the two-circle diffractometer, the sample normal lies in the plane defined by the incoming and outgoing beam (Figure 3.5). The sample is mounted in the way that the offset, which is the difference between $2\theta/2$ and ω is minimized.

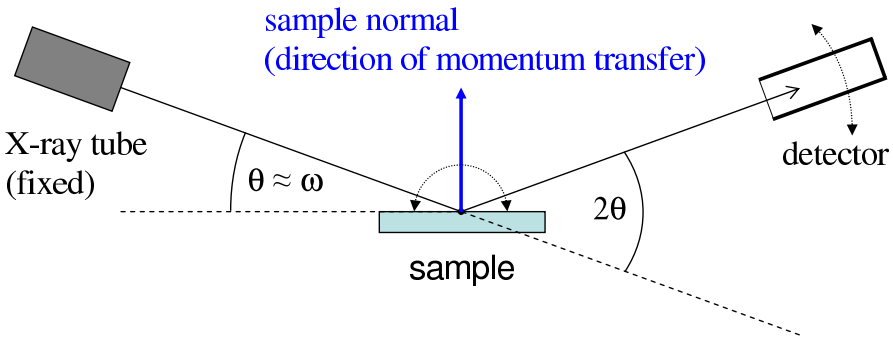

Figure 3.5: Schematic of two-circle XRD experiment.

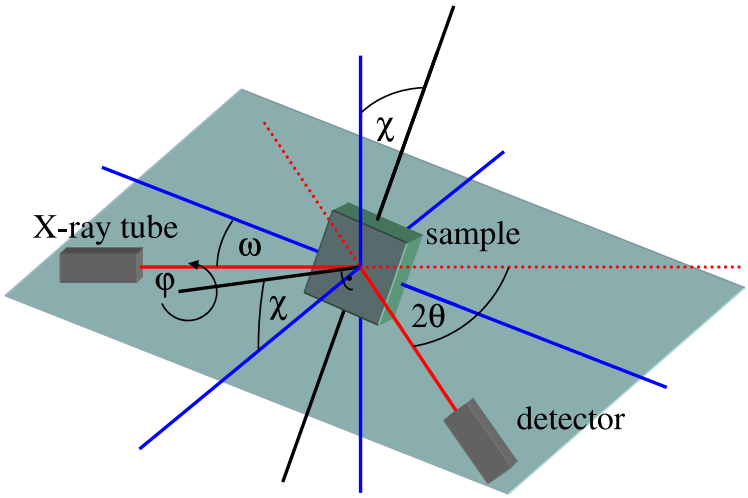

Figure 3.6: Schematic of a four-circle XRD experiment. Compared with a two-circle experiment, two additional angles occur: χ, the angle between the diffraction plane (blue) and the sample normal, and ϕ, the rotation angle around the sample normal.

Thus, only reflections (reciprocal lattice vectors) perpendicular to the sample surface can be observed. After height adjustment and offset correction, an accuracy of $\Delta 2\theta < 0.1^{\circ}$ is reached.

However, since the accessible reflections in a two-circle experiment are limited to one direction in reciprocal space, only few conclusions about the in-plane crystalline order and orientation can be drawn. Additional information are provided by a four-circle experiment (Figure 3.6), where the sample orientation is free, allowing the observation of various reflections over a wide range of spatial directions. While in principle all directions are accessible, some restrictions are due to the maximum position of the goniometer, which for the used setup is limited to $-40^{\circ} \leq \omega \leq 40^{\circ}$ and $-180^{\circ} \leq \chi \leq 0^{\circ}$.

Two-circle Diffraction

In an ω-scan or rocking curve the sample orientation ω is varied for a fixed angle 2θ between X-ray source and detector, which translates to a fixed periodicity perpendicular to the sample surface. Thus, the distribution of orientation of crystalline parts (mosaicity) with the specified lattice constant given by Bragg's law is measured. In Figure 3.7, a rocking curve of the (100) reflection of an epitaxial UPd_2Al_3 thin film on $LaAlO_3$ (110) is shown. The measured X-ray intensity as a function of ω displays two components of different widths. On top of a relatively broad ($\approx 0.5^{\circ}$) peak, a more narrow peak (down to 0.05°) of increased intensity is observed. Line shapes of that type are frequently found in epitaxial systems [102] and are indicative of a long range structural coherence in the film arising from the substrate. Rotational disorder on a shorter length scale produces the broad, diffusive component. For UPd_2Al_3 (100) on $LaAlO_3$, samples exhibiting a strong narrow component in the rocking curve proved to be of high crystalline quality regarding high count rates and the absence of impurity phases in XRD, as well as comparatively high residual resistance ratios (RRR) and the frequent occurrence of superconductivity in transport measurements.

If the sample is oriented with the twin walls of $LaAlO_3$ perpendicular to the diffraction plane, the twin micro structure of $LaAlO_3$ substrates is reflected in the film rocking curve. Two narrow components of reduced intensity are observed (Figure 3.8), with an approximate angle $\Delta\omega = 0.17^{\circ}$, which is the twinning angle of $LaAlO_3$ [91].

Another objective of measuring a rocking curve is to determine the offset,

which is given by the difference of the sample position with highest intensity ω_{max} and the Bragg angle θ. It represents the deviation from the perfect sample positioning in the mounting procedure.

For a $2\theta/\omega$-scan, the angles ω and 2θ are varied simultaneously. The offset was calculated from the rocking curve of the UPd_2Al_3 (100) reflection and automatically corrected. Thus, the sample is scanned for periodicities parallel to the UPd_2Al_3 (100) plane. Typical results for a well ordered UPd_2Al_3 (100) thin film are shown in Figure 3.9. Besides the film peaks, only substrate reflections and a weak Uranium oxide phase are detected. Experimental peak positions are found to agree well with the expected values for UPd_2Al_3, excluding a possible strain along the (100) direction:

Reflection	(100)	(200)	(300)	(400)
$2\theta_{measured}$	19.13°	38.77°	59.65°	83.05°
$2\theta_{expected}$	19.086°	38.729°	59.652°	83.083°

However, the two-circle diffraction as described here is only sensitive to out-of-plane crystallographic properties, i.e. the order perpendicular to the sample surface. Further, non ordered impurities cannot be observed directly by diffraction methods, only indirectly as they cause a reduction in the intensity of the film reflections.

Four-circle Diffraction

Investigations of the in-plane crystallography were performed on a four-circle diffractometer, as sketched before in Figure 3.6. Results of a scan of the reciprocal (1KL) plane of a UPd_2Al_3 (100) thin film are shown in Figure 3.10. The observation of all (allowed) reflections prove the 3-dimensional order of the sample, including in-plane order.

By measuring many different reflections, the complete set of lattice parameters can be determined for both, film and substrate. Exemplary results obtained by a fitting process are given in Table 3.2, with the data of the $LaAlO_3$ substrate serving as reference. In parentheses, the possible error of the fitting process is given for the last digit. All parameters are found to agree reasonable with bulk values within the accuracy of the measurement. Thus, there is no indication of any significant growth induced strain.

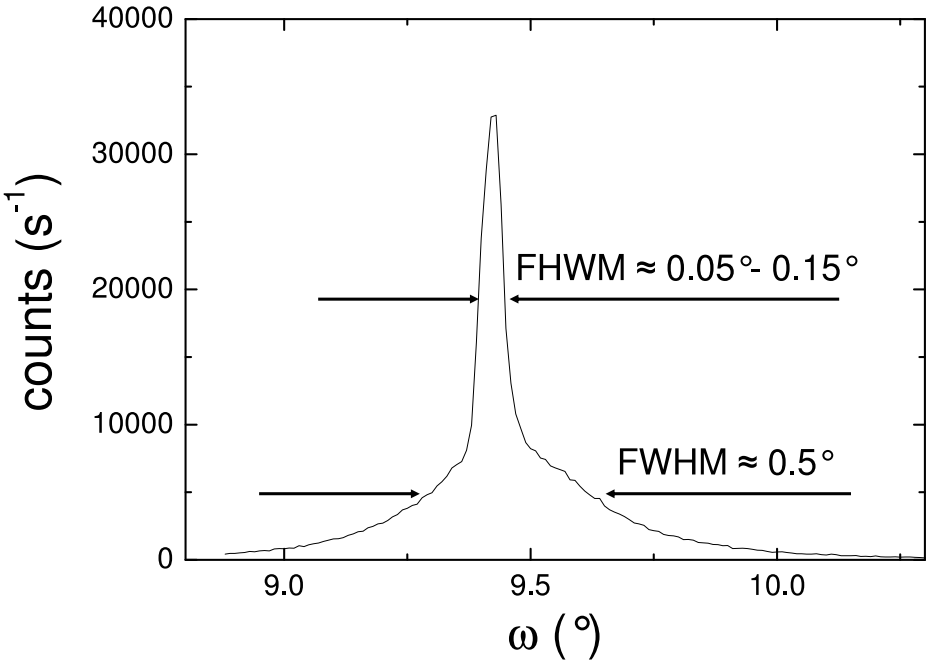

Figure 3.7: ω-scan of the (100) reflection of an UPd_2Al_3 thin film on $LaAl_3$ (110). Two components with different widths are observed.

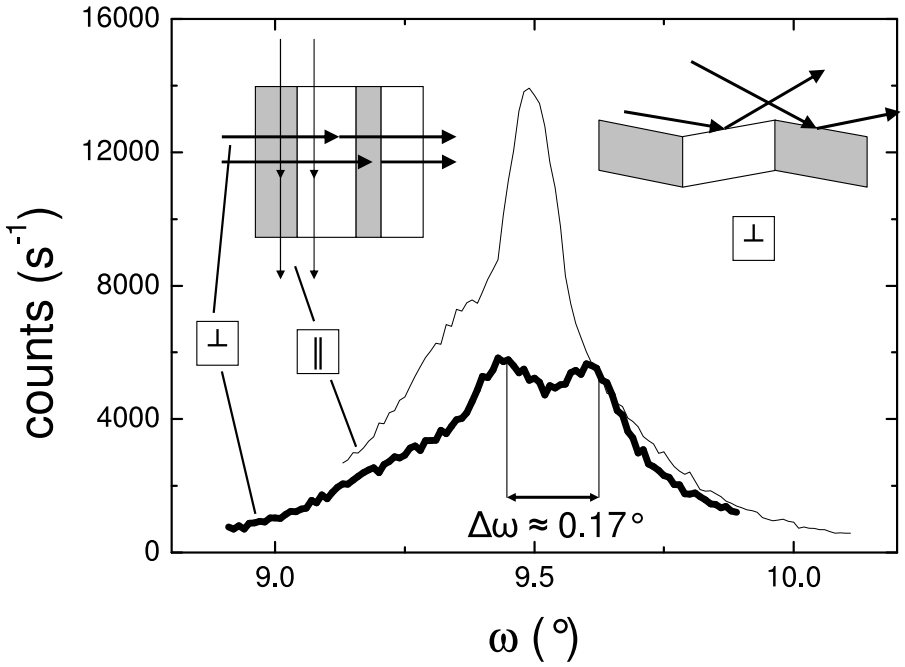

Figure 3.8: ω-scans of the (100) reflection with the substrate twin walls parallel (thin line) and perpendicular (thick line) to the diffraction plane. In the second case, two narrow components are observed which correspond to the two twin domains of the substrate. The two sample orientations are sketched in the left inset, the right inset illustrates the origin of two narrow structures in the rocking curve.

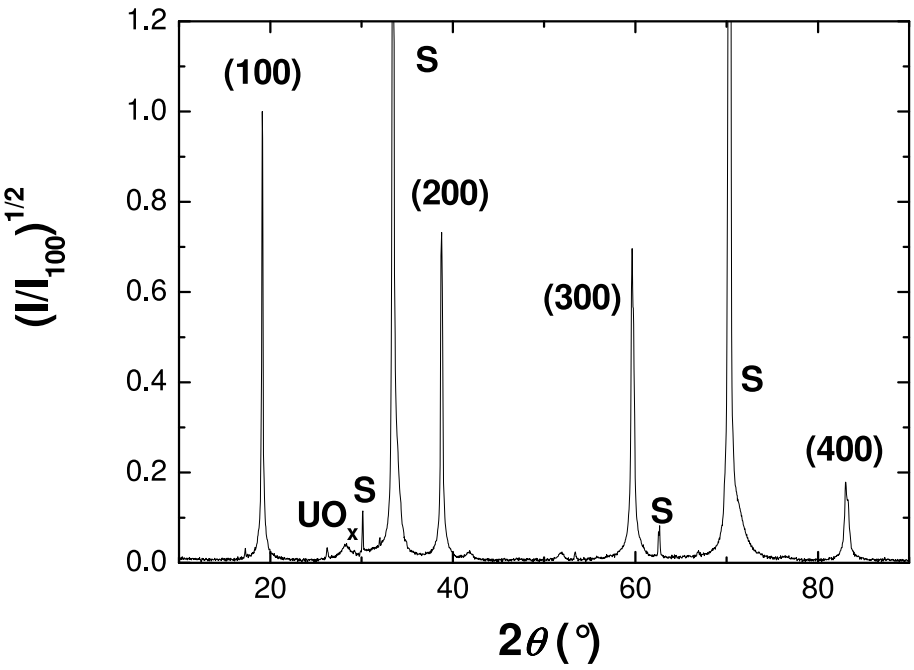

Figure 3.9: $2\theta/\omega$-scan of an epitaxial UPd_2Al_3 (100) film on $LaAlO_3$. Labeled are: film reflections (n00), substrate reflections (S) and reflections from Uranium oxide impurities (UO_x).

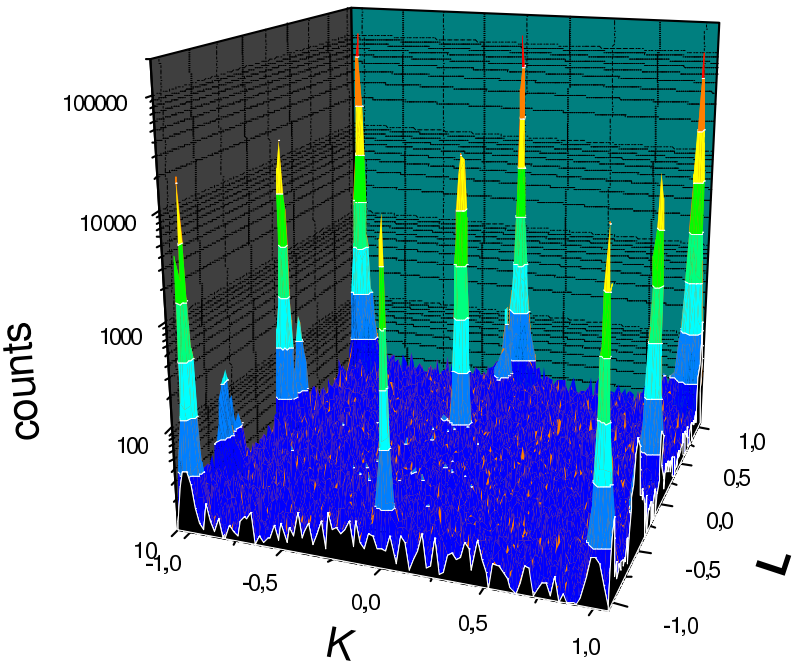

Figure 3.10: Four-circle XRD of an UPd_2Al_3 thin film. Scan of the reciprocal (1KL) plane: Counts in logarithmic scale vs. the momentum transfer in reciprocal lattice units.

	a (Å)	b (Å)	c (Å)	α	β	γ
UPd_2Al_3 *film*	5.362(3)	5.375(5)	4.186(2)	89.99(5)	90.02(4)	120.02(5)
UPd_2Al_3 [19]	5.365	5.365	4.186	90	90	120
$LaAlO_3$ *sub.*	3.789(1)	3.789(1)	3.785(1)	89.93(3)	89.94(3)	90.05(2)
$LaAlO_3$ [91]	3.790	3.790	3.790	90.09	90.09	90.09(5)

Table 3.2: Lattice constants of a UPd_2Al_3 (100) thin film and the $LaAlO_3$ substrate determined by four-circle XRD in comparison with values taken from the indicated references.

Further, the epitaxial relation that was suggested in the previous chapter is confirmed by analyzing the in-plane angle ϕ of suitable reflections [2]. Indeed, the basal b-vector of UPd_2Al_3 is parallel to the $[1\overline{1}0]$ direction of $LaAlO_3$ and the c-axis is parallel to [001] of $LaAlO_3$:

$$[010]_{UPd_2Al_3} \| (\overline{1}20)_{UPd_2Al_3} \| (1\overline{1}0)_{LaAlO_3} \| [1\overline{1}0]_{LaAlO_3}$$
$$[001]_{UPd_2Al_3} \| (001)_{UPd_2Al_3} \| (001)_{LaAlO_3} \| [001]_{LaAlO_3}$$

where brackets refer to real space vectors and parentheses to reciprocal lattice vectors.

Thickness Determination by Reflectometry

X-ray reflectometry is a useful method for thickness determination of thin films, e.g. for deposition rate calibration. For this, the reflected intensity for small angles $2\theta \leq 5^o$ is measured in two-circle geometry. Typical oscillations (Figure 3.11) of the intensity as a function of 2θ arise from the interference of parts of the incoming beam reflected at either the air-film or the film-substrate interface, where small changes in the diffraction indices occur. Therefore, the position of local intensity maxima is given by the Bragg formula (see above), when the total film thickness is inserted as the plane distance d (while minima are found for $n = integer + 1/2$)[3]. The most useful range for observing this oscillations depends on the sample

[2] In-plane reflections are not direct accessible, since the incoming and outgoing beam would be parallel to the film surface. Instead, linear combinations of the out-of-plane reflection and in-plane reflections are observed, because the combinations have the same in-plane angle ϕ as the in-plane reflections.

[3] Here the real part of the refractive index of the film for X-ray radiation is approximated to be 1. The typical deviation from this value is small $\delta \sim 10^{-6}$ [103]

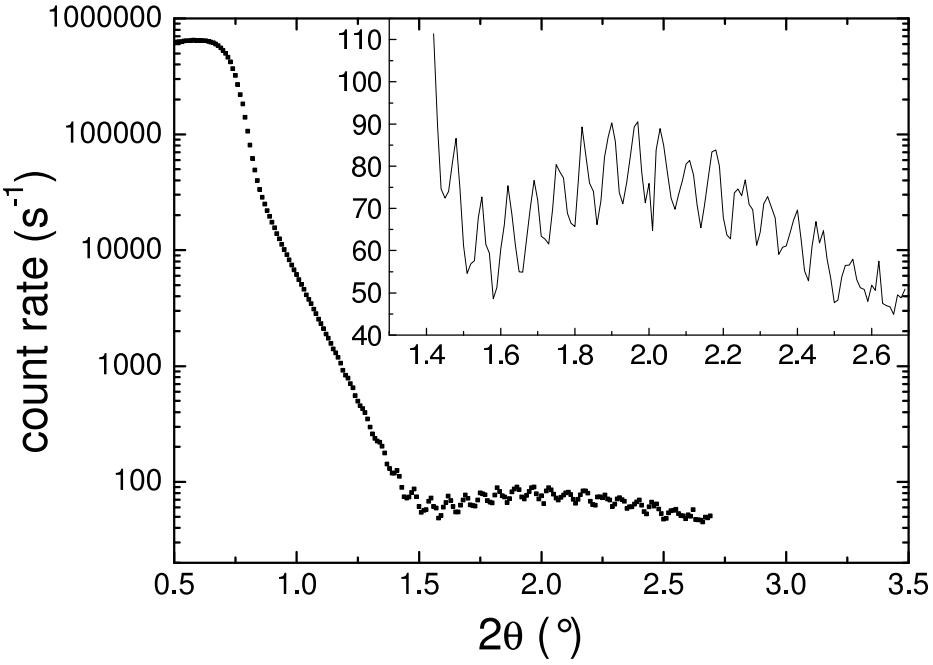

Figure 3.11: Small angle $2\theta - \omega$-scan of an UPd_2Al_3 thin film. From intensity oscillations between 1.4° and 2.6° (inset), the film thickness can be determined (please refer to the text).

characteristics, especially the total thickness and the surface roughness.

A straightforward and precise method of calculating the thickness of a mono layer from the oscillations is to extract the maxima (minima) position in $2\theta_n$ [4]. At this point the absolute value of n is generally not known, but it increases by one with each subsequent maxima (minima). However, when $sin(2\theta_n/2)$ is plotted as a function of n (or $n + 1/2$ for minima) and fitted by a linear function A*n+B, a mistake in n results only in an error of the y-axis intercept B, and therefore is irrelevant for the film thickness d, which is given by: $d = \lambda/(2A)$. For a check of the systematics, the maxima and minima are evaluated independently and should result in a similar thickness, as well as reducing the y-axis intercept B for corresponding n values. In the example of Figure 3.11 the results are (fitting uncertainties in parentheses):
maxima: $A = 6.191(35) * 10^{-4}$ and $B = 1.4(1.0) * 10^{-4}$,
resulting in a thickness of $d = 1244(7)$Å[5]

[4]Alternative methods exist; e.g. by comparing experimental data with simulations of designated programs like *Parrat* [104], also information about thickness and roughness of several layers (when appropriate) may be obtained.

[5]Technical deposition parameters: (rate(Å/s)/XTC-density(g/cm^3)/nominal thickness(Å)):

minima: $A = 6.186(32) * 10^{-4}$ and $B = 1.1(0.9) * 10^{-4}$,
resulting in a thickness of $d = 1245(6)$Å
while the maxima at $2\theta = 1.48^{o}$ corresponds to $n = 21$. Thus, the reached accuracy ($\approx 0.6\%$) is close to the systematic errors, e.g. the one ($\approx 0.25\%$) which arises from the uncertainty of the X-ray radiation wavelength (Cu-K$_\alpha$: $\lambda_{K_{\alpha_1}} = 1.5406$Å and $\lambda_{K_{\alpha_2}} = 1.5444$Å). Also the error from approximating the refractive index with 1 is, roughly estimated, in the same range (Appendix A.5).

3.5 Resonant Magnetic X-ray Scattering

For the investigations of the magnetic order in UPd_2Al_3 (100) thin films, a diffraction method with magnetic contrast was needed. Since neutron diffraction is not suitable for thin films because of the small sample volume, resonant magnetic X-ray scattering was used.

In principle, the total coherent elastic scattering amplitude for X-ray scattering on an atom consists of three parts [105]. First the usual Thomson contribution for scattering on the electronic charge, second a contribution for magnetic scattering and third a contribution from dispersive and absorptive processes. The former two do not provide sufficient magnetic contrast, because the first is insensitive to magnetic moments, while the second is comparatively small. However, the third contribution from absorptive processes can be significant if the X-ray photon energy is tuned in resonance with an electronic excitation from a core level to an unfilled atomic shell or narrow band. While the transition is of low order electric multipole, still magnetic contrast can be provided, if the final state of the transition is in a partially filled f or d band. Since the exclusion principle allows only transitions to unoccupied states, an exchange interaction results, which is sensitive to the magnetization of the f and d bands.

Therefore, by using synchrotron radiation, magnetic structures may be resolved in resonant magnetic X-ray scattering. Experiments on UPd_2Al_3 (100) thin films[6] were performed at the XMaS-CRG beamline of the European Synchrotron Facility (ESRF) in Grenoble in $\sigma - \pi$-geometry [108] with the X-ray energy tuned to the Uranium M$_4$ absorption edge ($E \approx 3.73$keV). At low temperatures, the observation of the purely magnetic (2,0,0.5) reflection proves the

Al(1.0/5.35/1683) Pd(1.0/14.67/1680) U(1.2/10.88/2000) , all ESV 4

[6]Corresponding experiments on UNi_2Al_3 are described elsewhere [106, 97]. For results on UPd_2Al_3 (001) films refer to [107].

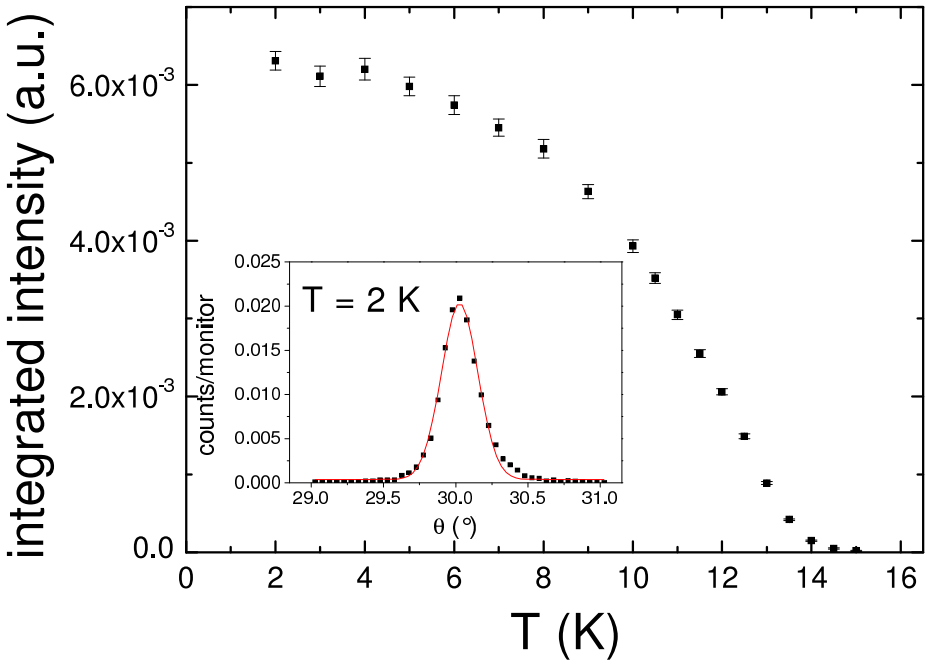

Figure 3.12: Integrated magnetic resonant scattered X-ray intensity of the (2,0,0.5) reflection in a UPd_2Al_3 (100) thin film at different temperatures. For this, the intensity was measured as a function of θ and fitted with a Gaussian function whose area represents a measure of the total reflected intensity. In the inset, the result of an exemplary $2\theta - \omega$-scan at 2K is shown.

existence of antiferromagnetic order in the sample, at least on the resonant probe time scale ($10^{-15} - 10^{-14}$s).

Results are presented in Figure 3.12. In the main part, the integrated intensity of ω-scans of the (2,0,0.5) reflection for different temperatures is given, while in the inset the ω-scan at $T = 2$K is shown. Significant magnetic scattering is observed below the ordering temperature $T_N \approx 14$K, which is slightly below values reported for the best bulks samples ($T_N \approx 14.3$K), indicating the representative character of the prepared thin film samples for the UPd_2Al_3 compound.

3.6 Temperature Dependent Transport

Last step in the standard characterization procedure of the UPd_2Al_3 thin films is the measurement of the temperature dependent electric resistance $R(T)$. For this preliminary measurement, four contacts are placed in the corners of the approximately square sample. Since the whole film area contributes to the transport process, neither the current direction nor path is clearly defined. Consequently,

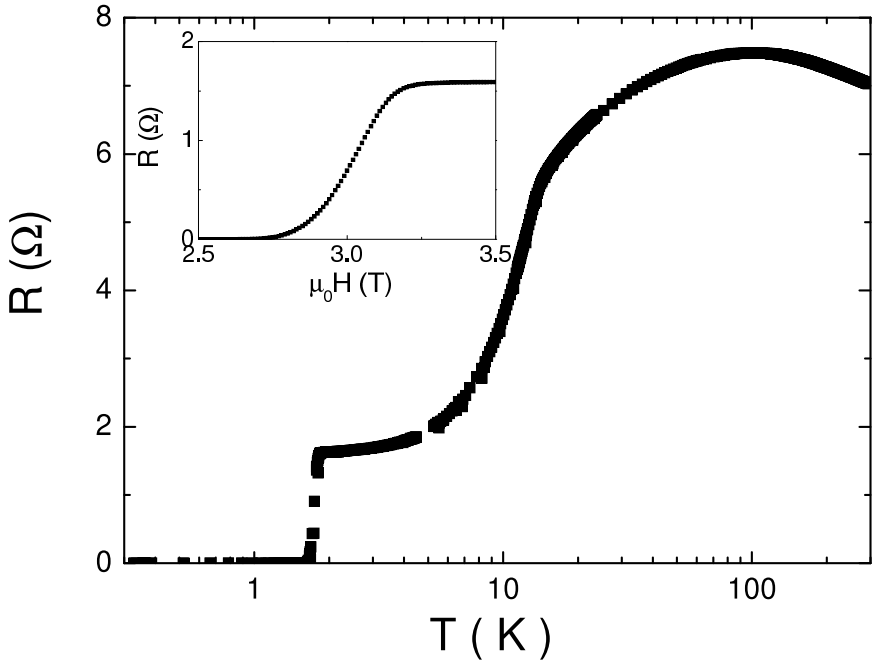

Figure 3.13: Temperature dependent resistance of a non structured UPd_2Al_3 (100) thin film. In the inset, the sample resistance as function of applied magnetic field at T=0.3K is displayed.

as shown in Figure 3.13, the resistance is measured in absolute units. Measurements were performed in a *Oxford Instruments, Kelvinox TLM* toploading ^{3}He cryostat ($T_{min} \approx 0.3$K).

In samples with a high degree of crystalline order as deduced from X-ray diffraction (e.g. like in Figure 3.9), characteristic behavior of UPd_2Al_3 was found. A relatively broad maximum in the resistivity is observed around 100K, i.e. above this point, the resistivity increases with decreasing temperature. This kind of feature is commonly found in heavy fermion systems and is caused by scattering of conduction electrons on independent, localized f-electrons, a phenomenon known as single ion Kondo scattering [110].

Below the magnetic ordering temperature $T_N \approx 14$K, the decrease of resistivity becomes more steep, producing a kink around T_N. Compared to best bulk single crystals ($T_c = 2$K [109]) and (001) oriented films ($T_c = 1.98$K [1]), the resistive superconducting transition occurs at a reduced temperature $T_c \approx 1.75$K while the transition width is increased ($\Delta T_c \approx 0.1$K). This and the relatively small residual resistance ratio of $RRR \approx 4.3$ indicates a comparatively high defect density in the (100) thin film samples. A reduced value for $B_{c2}(0.3\text{K}) \approx 3$T (Figure 3.13, inset) agrees with this picture.

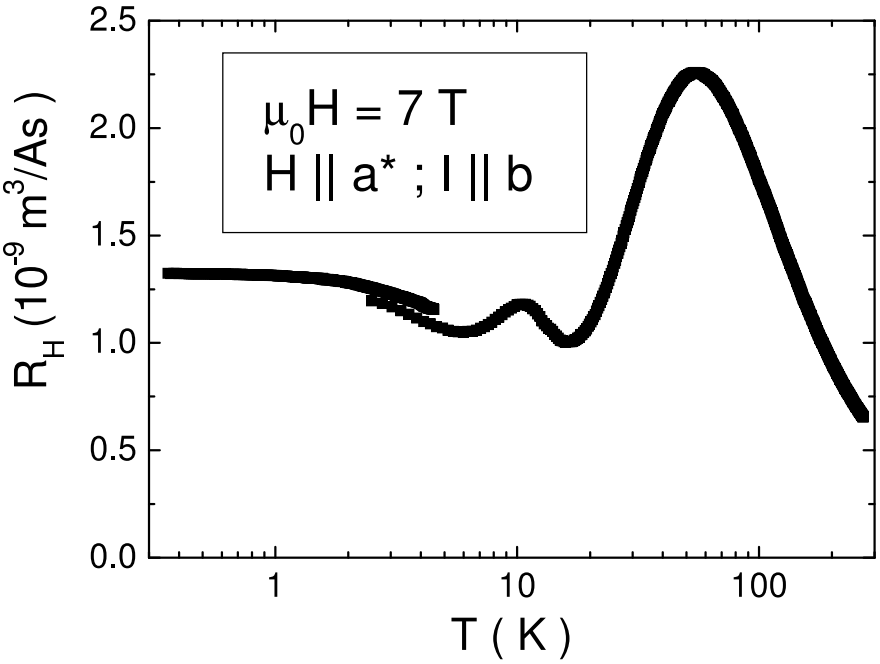

Figure 3.14: Temperature dependent Hall resistivity $R_H(T)$ in a UPd_2Al_3 (100) thin film. The magnetic field was applied perpendicular to the thin film surface, parallel a^*. Current direction was along (010), in the hexagonal system equivalent a. The discontinuity between 2K and 5K is due to the fact that two separate measurements were taken in different cryostats.

3.7 Hall Effect

Further agreement with UPd_2Al_3 (001) samples is found in Hall resistivity measurements of (100) oriented thin films. In Figure 3.14, the temperature dependent Hall resistivity in a UPd_2Al_3 (100) film is shown with the magnetic field applied perpendicular to the thin film surface, parallel a^*. A current was sent along the b-axis, equivalent to the hexagonal a-axis. The curve $R_H(T)$ displays two minima at around 6K and 16K respectively. The first was also observed in earlier measurements on UPd_2Al_3 (001) thin films where the magnetic field was applied parallel to the c-axis and the current direction was also along a [111]. The occurence of this first minimum was attributed to the superposition of a contribution due to coherence effects and another one due to skew scattering.

However, the second feature close to T_N was much weaker evolved in the previous experiment. The reason for this may be, that while the field is applied along the c-axis, the quasiparticles are moving on closed orbitals on the cylindrical part of the Fermi surface [24]. With an applied field along a, the orbitals are open

resulting in a bigger sensitivity to the onset of the antiferromagnetic order.

3.8 Summary

By combination of several characterization methods, it can be concluded that the prepared UPd_2Al_3 (100) thin film samples on $LaALO_3$ substrates show all characteristics (crystalline order, magnetic order and superconductivity) which are typical for the UPd_2Al_3 compound. A small residual resistivity ratio and the slightly reduced phase transition temperatures indicate a higher defect density in the samples compared with bulk single crystals and films grown in (001) direction. The most likely explanation for this is the alternative (100) growth direction which is not the energetically favored, *intrinsic* (001) growth direction (on randomly oriented sapphire). However, it is this new growth direction, with the a and c axes laying in-plane, which enables more detailed studies of the anisotropic transport properties.

Even after all precautions, variations in sample quality occur which are detected in X-ray diffraction and resistivity measurements. Most probable reason for the poor reproducibility are problems with the evaporation process of the Uranium and the increasing contamination of the deposition chamber with Uranium oxide. This is supported by the fact, that during the end of this work also the well established preparation of UPd_2Al_3 (001) thin films proved difficult.

To gain a more complete picture of the transport properties in UPd_2Al_3 and UNi_2Al_3, further samples were used. Especially the comparison with UNi_2Al_3 (100) thin films is fruitful. Detailed information on these films can be found in the work of *A. Zakharov* [97].

Chapter 4

Tunneling Spectroscopy on UPd_2Al_3 (100) Thin Films

In the understanding of superconductivity, tunneling spectroscopy played a central role. With this technique, pioneered by *Giaver*, the predictions of the BCS theory concerning the superconducting density of states and the temperature dependence of the energy gap $\Delta(T)$ was confirmed [112].

In strong coupling superconductors like e.g. Pb, the tunneling spectrum reveals additional structures, which are explained by the Eliashberg theory. Starting from a more realistic electron-phonon interaction, which is based on the phonon density of states $F(\omega)$ (known from neutron scattering) and a coupling parameter α, the Eliashberg theory gives a complex, energy dependent gap function $\Delta(\vec{k})$. Clear evidence for a phonon mediated electron pairing mechanism is provided by the perfect agreement of observed tunneling spectra with the predictions of the Eliashberg theory [113]. Taking the opposite approach, the phonon spectra $F(\omega)$ was successfully reproduced from tunneling data [114].

Also for the heavy fermion superconductor UPd_2Al_3, which had been considered to have a non-phononic pairing before [22], strong coupling features were found in the tunneling spectra [20]. Results from inelastic neutron scattering [43] allowed to ascribe these features to magnetic excitations, again shedding light on the pairing mechanism.

It can be concluded that tunneling spectroscopy is an extremely powerful tool for investigations of electronic states in superconductors. However, the experimental realization often enough proved to be very challenging. In the following chapter, basic principles of tunneling spectroscopy and measurement techniques

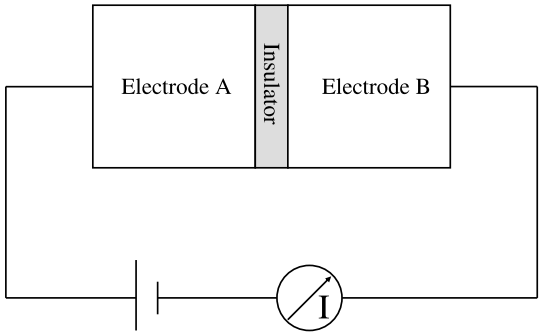

Figure 4.1: Schematic of a tunneling experiment.

will be explained. A short overview over previous related experiments on UPd_2Al_3 and UNi_2Al_3 is given, before results on UPd_2Al_3 (100) tunnel junctions, obtained during this work, are presented. These experiments complement the previous work, since a new crystallographic direction is probed and hence conclusions about the anisotropy of the gap function $\Delta(\vec{k})$ may be drawn.

4.1 Theory of Tunneling Spectroscopy

The method is based on the quantum mechanical tunneling phenomenon, i.e. the fact that a quantum mechanical object, e.g. an electron, has a non-zero probability of passing a classically forbidden zone, provided this zone is small enough. Object of investigation is a tunnel junction as sketched in Figure 4.1: Two conducting electrodes are separated by a thin insulating layer. The charge transfer between the electrodes by electron tunneling can be expressed by a transfer Hamiltonian:

$$H = \sum_{\sigma \vec{k} \vec{q}} T_{\vec{k}\vec{q}} c^*_{\vec{k}\sigma} c_{\vec{q}\sigma} + h.c. \tag{4.1}$$

where the index $\vec{k}$ refers to one electrode (A), while $\vec{q}$ refers to the other (B). The spin is given by σ and is assumed not to change in the tunneling process for a non magnetic barrier. All further barrier properties are reflected in the tunneling matrix element $T_{\vec{k}\vec{q}}$. In the expression above, the first term describes the transfer of one electron from electrode B to electrode A, while the hermitian conjugate does the reverse.

Up to now, the character of the electrodes have not been specified. For this work, the case where one electrode is in the superconducting state and

the other is normalconducting has to be considered (superconductor-insulator-normalconductor or S-I-N). In the superconducting electrode, the one electron states have to be written in terms of quasi-particle excitations (Bogoliubons):

$$c^*_{\vec{k}\uparrow} = u_{\vec{k}}\gamma^*_{e\vec{k}0} + v^*_{\vec{k}}\gamma_{h\vec{k}1} \tag{4.2}$$

However, assuming a nearly constant matrix element $T_{\vec{k}\vec{q}}$ close to the Fermi surface, it can be shown that the BCS coherence factors $u_{\vec{k}}$ and $v_{\vec{k}}$ drop out when the sum over $\vec{k}$ is taken [7]. Thus, the tunneling probability (and hence the current) is simply proportional to $\left|T_{\vec{k}\vec{q}}\right|^2$.

The Semiconductor Model

The vanishing of the BCS coherence factors allows to consider a tunneling process, which transforms one electron on the normalconducting side into a quasi-particle excitation on the superconducting side. This can be described in the semiconductor model, illustrated in Figure 4.2. [1] The effective density of states for one electron tunneling into the superconductor is then simply given by the density of (independent) one quasi-particle excitations from the BCS ground state:

$$\frac{N_s(E)}{N(0)} = \begin{cases} \frac{E}{(E^2-\Delta^2)^(1/2)} & for\ E > \Delta \\ N_s = 0 & for\ 0 < E < \Delta \end{cases} \tag{4.3}$$

For tunneling out of the superconductor, the picture has to be completed by the density of potential one-particle holes for negative chemical potential μ, which is the reflection of the excitation density above. The reason is, that when creating a hole, the remaining electron of the *Cooper pair* (with momentum $\vec{k}, -\vec{k}$) has to transfer to one of the excitations. Thus the effective density of states for the superconductor becomes a semiconductor one with the energy gap 2Δ, reducing to the normalconducting case as $\Delta \to 0$.

On the other side, the density of states for the normalconductor is taken to be constant, which is a good approximation since the energy scale involved ($\sim \Delta$) is

[1] The semiconductor model is a simplification, and does not always provide a good description. For example in some cases, interference effects between different degenerate $\vec{k}$ values can occur, resulting in an oscillation of the tunneling current with voltage or sample thickness [115]. Also it fails do describe charge-imbalance systems, and obviously ignores pair processes which are important e.g. in the Josephson effect. However, in the framework of this work, the semiconductor model proves to be sufficiently accurate. For a more detailed treatment please refer to Ref. [116].

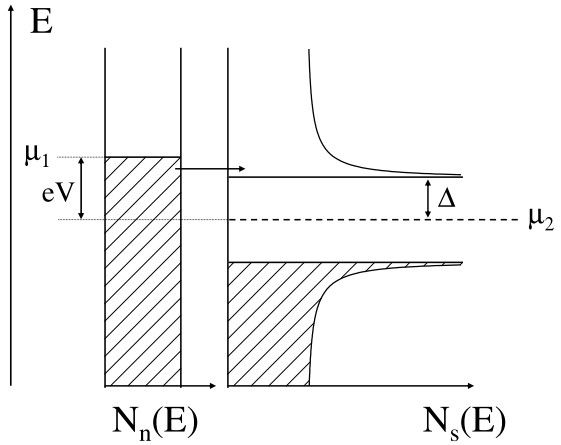

Figure 4.2: Diagram of the semiconductor model applied to a Superconductor-Insulator-Normalconductor (SIN) tunnel junction at $T = 0$K (occupied states are shaded). The density of states is plotted horizontally against the energy vertically. The difference in chemical potential μ is given by the applied voltage V multiplied with the electron charge e and here slightly exceeds the energy gap Δ. By the horizontal arrow, the tunneling process of one particle is symbolized.

small compared to the normalconducting band structure features. [2] As usually, the occupation probability of the fermionic states (on both sides) is given by the Fermi-Dirac statistics.

Differential Conductance and Density of States

Applying Fermi's golden rule to the semiconductor model, the tunneling current from the metallic electrode to the superconducting one is proportional to:

$$I_{N\to S} \propto \int_{-\infty}^{\infty} |T|^2 \, N_n(E+eV) f(E+eV) N_s(E) \, [1-f(E)] \, dE \qquad (4.4)$$

where N_n is the metallic and N_s the superconducting density of states, so $N_n f$ equals the density of occupied initial states and $N_s(1-f)$ the density of empty final states. The chemical potential on the two sides are shifted with respect to each other by eV, with V is the applied voltage across the junction (Bias voltage V_{bias}).

After subtracting the corresponding expression for the reverse and assuming a constant tunneling matrix element T, the net current is found:

[2] This assumption may have to be reviewed in the case of a superconductor driven normal-conducting by an applied magnetic field [117].

$$I \propto |T|^2 \int_{-\infty}^{\infty} N_n(E+eV) N_s(E) \left[f(E) - f(E+eV) \right] dE \tag{4.5}$$

As mentioned before, on this scale also the metallic density of states can be assumed constant. Taking the derivative with respect to the applied voltage, it follows:

$$\frac{dI}{dV} \propto \int_{-\infty}^{\infty} N_s(E) \left[-\frac{\partial f(E+eV)}{\partial (V)} \right] dE \tag{4.6}$$

which relates the differential conductance of the tunnel junction with the superconducting density of states. The integral $\int_{-\infty}^{\infty} dE$ becomes easy for $T \rightarrow$ 0K, since the derivative of the Fermi function $\partial f(E+eV)/\partial V$ approaches the Dirac δ distribution. Hence, the dependence becomes a strict proportionality, while at finite temperatures the conductance measures a density of states which is smeared out by $\pm 2k_B T$.

Thus, measuring the differential conductance of a S-I-N tunneling junction provides direct access to the superconducting density of states. For strong-coupling superconductors, the density of states takes a more complex form which is described by the Eliashberg theory, but the above connection between differential conductance and superconducting density of states remains the same.

Exemplary for this method, in Figure 4.3, the differential conductance of an Al-AlO_x-Pb tunnel contact is shown. Detailed explanations of the observed features are given in the figure caption.

BTK-Theory

When the tunnel barrier is relatively weak, the tunneling current can become big enough to disturb the thermal equilibrium of states in the electrodes; in other words, the occupation of states is no longer governed by the Fermi-Dirac statistics. In this case, additional processes which involve excited states contribute to the transport current.

The BTK-theory [118] was developed to describe all situations from a perfect tunneling barrier to a metal-superconductor (S-N) interface. Therein, the barrier is modeled by a repulsive box potential $H\delta(x)$. The barrier strength is expressed in terms of a dimensionless parameter $Z = k_F H / 2\epsilon_F$. Transmission and reflection coefficients are calculated depending on the incoming wave vector, using the appropriate quasi-particles in the superconducting material.

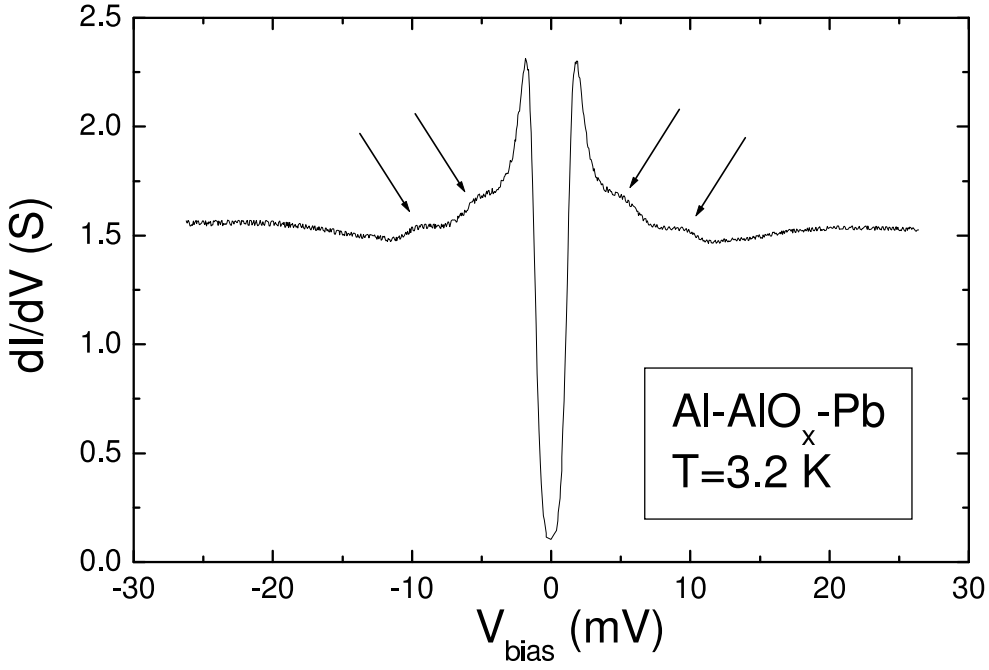

Figure 4.3: Differential conductance of an Al-ALO$_x$-Pb tunnel junction in the S-I-N regime at $T \approx 3.2$K. This temperature is well below the critical temperature T_c of Pb, but clearly above the one of Al. Smearing occurs in the range of $4k_BT \sim 1$mV due to thermal occupation of states above the Fermi energy. Typical superconducting features are reduced conductance at low bias voltages inside the range $|V| < \Delta$ and conductance peaks at $V \approx \pm\Delta$. In the ideal case, values of $dI/dV|_{|V|<\Delta} = 0$ and $dI/dV|_{V=\pm\Delta} \rightarrow \infty$ are expected. Arrows mark characteristic Pb strong coupling deviations from the BCS density of states, which appear at $eV_{bias} \approx \pm(\Delta + E_{ph})$, with E_{ph} the energies of Pb phonon resonances.

For values of $Z >> 1$, which correspond to a high tunneling barrier, the results of the treatment in the previous section are recovered. However, for values $Z < 1$, implying a small or not existing barrier, a completely different behavior is found. One example is the *Andreev* reflection occurring on a metal-superconductor interface, where an incoming electron is transformed into a *Cooper* pair in the superconductor, while a hole is reflected. By this, the conductivity for bias voltages inside the energy gap is increased by a factor of two, since two elementary charges are transferred in the process. In contrast, in the tunneling process, a reduced conductivity is observed.

Experimentally, tunnel contacts (of the planar type) with small or vanishing barrier cause problems due to their small resistance, which results in increased influence of heating effects and voltage drop across the electrodes in the junction area. Consequently, this situation is studied as point contacts, realized by

pressing a thin needle into a bulk sample. If the contact radius is sufficiently small (compared to the electron mean free path), the electronic density of states can be directly studied. However, with this method it proved difficult to obtain unambiguous results, since observed spectra characteristics may be attributed to the electronic structure, barrier properties or remaining heating effects.

4.2 Related Tunneling Experiments on UPd_2Al_3 and UNi_2Al_3

Spectroscopy on planar UPd_2Al_3 tunneling junctions was successfully carried out by *M. Jourdan et al.* [20]. The samples comprised of a UPd_2Al_3 (001) thin film base electrode, covered with a thin AlO_x tunneling barrier. On this, an insulating Ge layer with a central trench was deposited by thermal evaporation combined with a shadow mask. Crossing the trench, a stripe of Pb served as counter electrode, likewise prepared by thermal evaporation with another shadow mask. Thus, the junction area was defined by the overlap of the trench in the Ge and the Pb stripe.

By applying a magnetic field $\mu_0 H = 0.3$T which is overcritical for Pb but relatively small compared to the upper critical field of the type-II superconductor UPd_2Al_3, the contact was measured at $T \approx 0.3$K in the S-I-N regime, with UPd_2Al_3 constituting the superconducting electrode. In the tunneling spectra, i.e. the differential conductance as function of bias voltage, the superconducting energy gap $\Delta \approx 235\mu$eV of UPd_2Al_3 was observed in the crystallographic c-direction. Additionally, deviations from a weak coupling fitting function (after Dynes [119]) were found, which were identified as strong coupling signatures of the superconducting pairs to magnetic excitations.

The existence of an energy gap in c-direction allows conclusions about the gap symmetry, since the A_{1g} representation of the D_{6H} point group of UPd_2Al_3 is the only one[3] to exhibit this feature. However, this representation implies that the energy gap is maximal in the c-direction, which stands in contrast to the findings from NMR experiments [48], indicating a maximal value of about $\Delta \sim 470\mu$eV.

In another experiment, *A. Zakharov et al.* studied extensively the properties of UNi_2Al_3 tunneling junctions, based on (100) oriented UNi_2Al_3 thin films [97]. Several concepts of preparation have been tried, but no clear signature of

[3] with even parity, please refer to Chapter 1.3

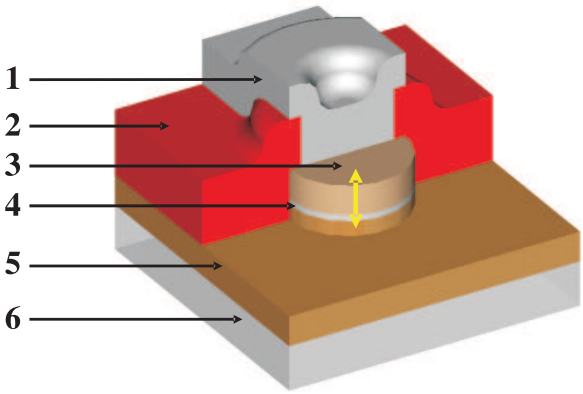

Figure 4.4: Schematic of a mesa structure (courtesy of A. Zakharov): (1) silver paint top contact, (2) negative photoresist, insulating, (3) top Ag electrode, (4) AlO_x tunneling barrier (5) UPd_2Al_3 base electrode, (6) substrate; current direction along the yellow arrow.

superconductivity in UNi_2Al_3 was observed. Most likely explanation for the lack of superconducting features in the tunneling spectra are experimental problems, related to the comparatively high film roughness. Under these circumstances it proved difficult to obtain a closed, completely oxidized tunneling barrier. Basically, the same problems occur that were encountered in this work and discussed further below (in the Section *Possible Junction Defects*). However, an intrinsic origin like a pairbreaking effect at the interface or a gap node in the investigated a^* direction cannot be excluded.

In this context, tunneling spectroscopy of UPd_2Al_3 in the (100) direction is of high interest, mainly for two reasons. First, bearing in mind the similarities between UPd_2Al_3 and UNi_2Al_3, the interpretation of results gathered on UNi_2Al_3 (100) can be aided by comparing with data obtained from UPd_2Al_3 (100) using the same techniques. Second, the measurement of the energy gap in the a^*-direction would help to establish the actual energy gap symmetry, which is crucial in further understanding the pairing mechanism.

4.3 Experimental Details

Tunneling Junction Preparation

For this work, tunneling contacts were prepared based on UPd_2Al_3 (100) thin films. Onto this a thin AlO_X tunneling barrier and a Ag counter electrode are

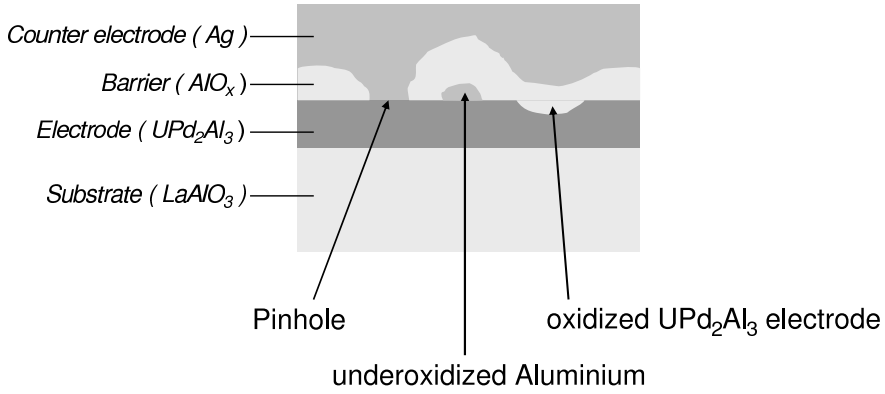

Figure 4.5: Schematic of possible defects occurring at the junction interface (cross section, not to scale).

deposited, before the sample is structured by optical lithography. All preparation details and specifications are given in Chapter 2 (and the Appendix). The final mesa structure after deposition and photolithographical patterning is again shown in Figure 4.4.

Possible Junction Defects

Crucial points in the preparation of the tunneling junction are the barrier's properties. The barrier is formed by plasma assisted oxidation of a thin Al layer which is deposited by electron beam evaporation. Figure 4.5 sketches the possible defects that may occur in this process. First, there may be pinholes in the deposited Al layer, resulting in shortcuts in the barrier, which will dominate electrical transport. If the Al layer is too thick, it may not be fully oxidized. In this case the tunneling current will pass from Al into the counter electrode and become less or not sensitive to the density of states in the intended UPd_2Al_3 base electrode. On the other hand, if the Al layer is to thin, the top part of the base electrode may be oxidized too, changing the base electrode's electronic properties.

Thus, the deposition of a homogeneous Al layer of appropriate thickness and controlled oxidation conditions are key to the successful junction preparation. Critical influences are the base film roughness and stability against oxidation, as well as the wetting properties of Al on the film.

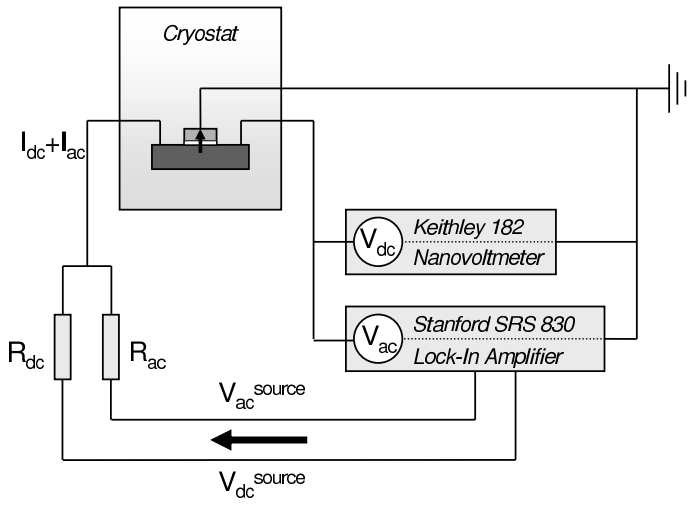

Figure 4.6: Set-up for the differential conductance measurement. Voltage outputs of the *Stanford SRS-830* Lock-In amplifier are connected via preresistances $R_{ac}, R_{dc} >> R_{junction}$ to realize a virtual current source. The voltage dropping over the junction is analyzed by the same Lock-In amplifier (V_{ac}) and a *Keithley 182* Nanovoltmeter (V_{dc}).

Measuring dI/dV

After mounting on the sample stage of a *Oxford Instruments, Kelvinox TLM* toploading ^{3}He cryostat, the junction is contacted with silver paint and thin copper wires. While two separated wires (for current feed and voltage sense) are connected to the ground electrode, the voltage and current contacts attached to the top of the mesa are connected in the same drop of silver paint, since the diameter of the mesa junction is small (typically 200 μm). Thus only a three point measurement geometry is realized, however, because the resistance of the tunneling junction is typically two orders of magnitude higher (several hundred Ω compared to Ω) than the resistance of the wire and the silver paint, the drawback on the measurement is considered negligible.

An ac-modulation method is employed for the direct measurement of the differential conductance (without need of numerical differentiation of an V-I curve). For this, a direct current I_{dc} modulated with a small alternating current $I_{ac} = \hat{I}sin(\omega t)$ is fed through the junction while the direct and alternating component of the voltage are measured separately. A schematic of the set-up used in this work is shown in Figure 4.6.

Employing a Taylor expansion for the voltage dropping over the junction:

$$V(I_{dc} + \hat{I}sin(\omega t)) = V_{dc} + V_{ac} = V(I_{dc}) + \left.\frac{\partial V}{\partial I}\right|_{I_{dc}} \hat{I}sin(\omega t) + ... \tag{4.7}$$

it follows that the differential conductance dI/dV can be approximated by the ratio of the amplitudes of the source alternating current I_{ac} and of the measured alternating voltage $V_{ac} \approx \hat{V}sin(\omega t + \varphi)$:

$$\left.\frac{dI}{dV}\right|_{V(I_{dc})} \approx \frac{\hat{I}}{\hat{V}} \tag{4.8}$$

Here the differential conductance is not taken at exactly $V_{dc} = V_{bias}$), but averaged over $V_{dc} + V_{ac}$, resulting in a resolution of approximately $\hat{V}$. Consequently, $\hat{I}$ should be kept as low as the sensitivity the of V_{ac} measurement allows. In the experiment, $\hat{V}$ was kept in a range of 15-20 μV by using it as a feedback parameter to adjust $\hat{I}$. Further points about this experimental approach to be mentioned are the following. Since the resistance of the junction is non-ohmic, V_{ac} is not of a pure *sin* shape. Also, a small phase shift φ between current and voltage occurs because the junction represents also a capacitance. Both effects are small enough to be neglected. Regions with negative differential conductance are not accessible with this current driven method, however in the case of a S-I-N junction they are not expected (while this is relevant for S-I-S junctions).

4.4 Results

Tunneling spectroscopy was performed on UPd_2Al_3 (100)-AlO_x-Ag mesa tunnel junctions. Unfortunately, it proved extremely difficult to obtain samples that both have a superconducting UPd_2Al_3 electrode and can be assumed to be in the tunneling regime. For once, the reproducibility of the UPd_2Al_3 deposition was low for reasons discussed in Chapter 2. Additionally, in many junctions the barrier was obviously defect, e.g. showing very low area resistivities in the order of $\rho_A = 0.1\Omega\text{mm}^2$ that decreased further with lower temperature. This behavior is typical for a metallic shortcut in the barrier. Most likely these shortcuts arise from pinholes in the barrier, but also the resputtering of film material on the sides of the mesa during ion beam etching has to be considered. Other samples showed insulating behavior, due to overoxidation.

However, spectroscopic results of a presumably intact tunnel junction could be obtained. The UPd_2Al_3 base electrode shows one of the highest critical temperatures $T_c \approx 1.73$K ever observed in (100) oriented thin films. Also the residual resistance ratio $RRR \approx 7.1$ is relatively high. As known from sample analysis (Chapter 3), these kind of samples exhibit typical electronic properties of UPd_2Al_3, even though crystalline quality is reduced compared with the best bulk single crystals and (001) oriented thin films. However, for (001) oriented films, reasonable tunneling results have been obtained from films with even lower transition temperatures in the past [1].

The thickness of the Al layer before oxidation was approximated from deposition rate measurements to be $d = 30$Å[4]. At room temperature, the total resistance of the mesa junction (diameter $D = 200\mu$m) was $R(300\text{K}) = 560\Omega$, amounting to an area resistance of $\rho_A(300\text{K}) = 17.6\Omega\text{mm}^2$. As expected for a tunneling junction, these values slightly increased for lower temperatures to $R(4.2\text{K}) = 653\Omega$ and $\rho_A(300\text{K}) = 20.5\Omega\text{mm}^2$ respectively.

The counter electrode consisted of sputtered Ag, a non superconductor, which ensures that all observed characteristics can be ascribed to the base electrode. Experience [97] showed that this assumption does not always hold when instead a type-I superconducting counter electrode (e.g. Pb) is used, in which superconductivity is suppressed by means of a magnetic field. On the other hand, the possibility of testing the tunnel junction by observing the counter electrode's superconducting features is lost when a normalconducting material is used.

To characterize the tunneling barrier, the differential conductance was measured for high bias voltages at $T = 4.2$K, well above the critical temperature of UPd_2Al_3 (Figure 4.7). From the *Brinkmann* model assuming a trapezoidal barrier [120, 121], the dI/dV curve of a N-I-N junction is known to be roughly parabolic as a function of V_{bias} with a small linear term, which corresponds to the barrier asymmetry. Following the approach of Ref. [98], the measured data was fitted in a range excluding very low and high bias voltages. Higher order contributions cause deviations from parabolic behavior at high bias voltages ($> 0.6V$) while in the low voltage region an additional v-shape structure appears. Parameters extracted from the fit are:

$\phi = 2.7\text{V} \qquad \Delta\phi = 1.4\text{V} \qquad S = 13\text{Å}$

where ϕ is the height of the model potential barrier, $\Delta\phi$ the barrier asymmetry and S the width of the model potential barrier. Keeping in mind that the pa-

[4] nominal 45s at $1\mathring{A}$/s after XTC controller; $\rho = 5.35\text{g/cm}^2$

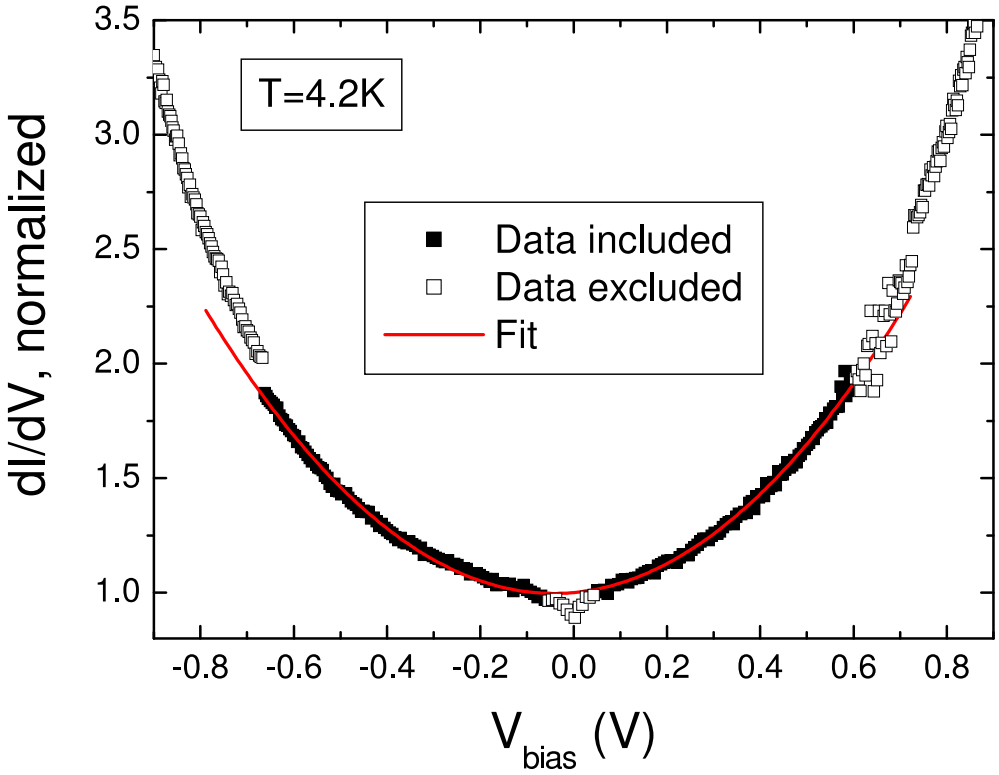

Figure 4.7: High bias voltage differential conductance dI/dV (normalized) of an $UPd_2Al_3(100)$-AlO_x-Ag mesa tunnel junction at $T = 4.2$K. Data shown as filled boxes was used for the fit represented by the red line. Open symbols denote data not included in the fit (refer to text for details).

rameters obtained from the fit apply to the model potential and not to the actual physical barrier, the agreement with the estimated thickness (30Å) and the band gap of AlO_x (6.2eV [122]) is reasonable. However, the Al layer may be underoxidized since thickness and height of the model barrier are reduced. On the other hand, no signatures of superconducting Al were found down to $T = 0.32$K.

Still, further discussion is needed. For example, it was found that a parabolic behavior of the differential conductance is not sufficient to ascertain a particular junction is in the tunneling regime [123]. In fact, even with pinholes strongly dominating the current, the model will yield reasonable barrier values. Depending on the size of the pinholes, the model parameter barrier height ϕ increases, while the effective thickness S decreases [124]. However, the increase of junction resistance with decreasing temperature is widely seen as an indication for the absence of pinholes [125]. Thus, there is good reason to assume that the sample investigated here was in the tunneling regime.

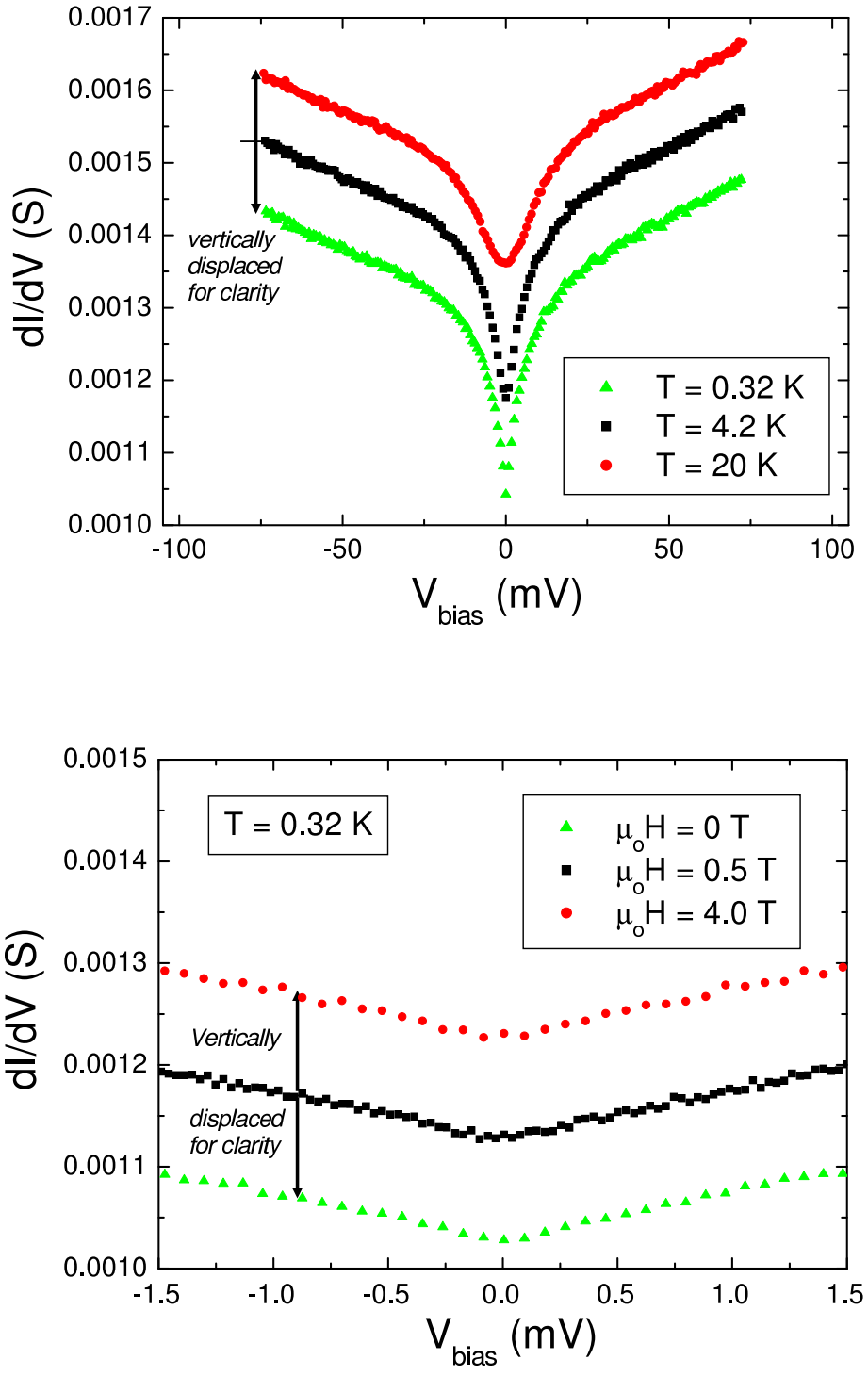

Figure 4.8: Differential conductance dI/dV of an $UPd_2Al_3(100)$-AlO_x-Ag mesa tunnel junction. Top: as a function of temperature in zero magnetic field.
Below: as a function of magnetic field at $T = 0.32$K. (Curves are vertically displaced for clarity.)

Results of measurements at different temperatures and magnetic fields are summarized in Figure 4.8. No significant influence of either temperature or magnetic field was observed. The differential conductance stayed mostly unaffected by the superconducting transition of the UPd_2Al_3 base electrode around $T_c = 1.73$K. As seen in the upper panel, a V-shape deviation from parabolic behavior inside the range of $|V_{bias}| \leq 20$mV is found, with no regard whether the temperature is below T_c or clearly above. Slightly smeared out it also prevails up to $T = 20$K, above the antiferromagnetic transition temperature T_N. No additional features were observed in the range of the expected energy gap, shown in the lower panel.

Conclusion

There are many possible reasons for the absence of any signature of superconductivity in the measured tunneling spectra. First, the current may not pass through the intended UPd_2Al_3 -AlO_x-Ag stack because of junction defects discussed further above. Although the existence of pinholes is unlikely because of the temperature dependence of the contact resistance, it cannot be completely excluded. Tunneling from not oxidized Al into Ag is quite unlikely, since Al is expected to exhibit superconductivity below $T_{c,Al} = 1.14$K, of which features should be visible at least for measurements at $T = 0.32$K.

Second the superconducting state may not be fully developed in the UPd_2Al_3 electrode. For example the superconducting transition was deduced from the vanishing of the electric resistance. However, this can be due to a superconducting percolating path through the sample, without need for a transition taking place in the sample volume[5]. Also superconductivity may be suppressed in a degraded surface layer of the UPd_2Al_3 thin film, the area which is actually probed by the tunneling spectroscopy. Surface degradation may be due to both, oxidation before or during formation of the tunneling barrier or segregation during the growth process of the film.

While reasons discussed up to now correspond to experimental failures, also intrinsic reasons for the absence of superconducting features in the tunneling

[5]Concerning volume sensitive measurements, from the observation of the purely magnetic $(00\frac{1}{2})$ reflection in resonant magnetic X-ray scattering (in Chapter 4), at least the existence of antiferromagnetic order was proved in the volume of a very similar sample (concerning residual resistance ratio RRR and critical temperature T_c). Although this indicates a relatively homogeneous crystalline quality of the sample, it constitutes only a weak hint for the volume character of the different order mechanism superconductivity.

spectra have to be discussed. While the existence of a gap node in the (100) direction is quite unlikely, the surface itself can have an intrinsic pairbreaking effect in the unconventional superconductor UPd_2Al_3, without further relation to the sample crystalline quality. Also a possible influence of the counter electrode may have to be taken into account since recently a significant influence of the actual counter electrode material was predicted theoretically [126].

For the lack of clear signatures and the multitude of possible explanations for this, it has to be concluded that based on the existent tunneling measurements reliable conclusions about the superconducting properties of UPd_2Al_3 in the (100) direction cannot be drawn. Further experiments are needed to either confirm or correct the present results.

Chapter 5

Electronic Transport Anisotropy in UNi_2Al_3 and UPd_2Al_3

Although not as direct as tunneling spectroscopy, conventional electronic transport measurements can give valuable insight into both, the normal and the superconducting state. In the case of UNi_2Al_3, the transport properties allow conclusions about the Fermi surface and are strongly indicative of weakly coupled multiband superconductivity. After a review of the previous results, this topic will be discussed in more detail based on new experimental data. Indications of the intrinsic and unique nature of the observed features are pointed out, e.g. by comparison with UPd_2Al_3. Further, evidence is provided that the ordered magnetic moments have to be assigned to one particular, cylindrical sheet of the Fermi surface.

5.1 Experimental Techniques

All data presented in this Chapter were taken in an *Oxford Instruments, Kelvinox TLM* toploading ^{3}He cryostat with a base temperature of $T_{base} \approx 0.3$K. Transport measurements on thin film samples structured[1] in different geometries were performed. Standard current sources was a *Keithley* 224 but also the voltage outputs of a $Stanford\ SRS-830$ Lock-In amplifier were used in connection with preresistances (in a similar setup to the one shown in Figure 4.6). The voltage dropping across the sample part of interest was measured with a *Keithley* 182 *Nanovoltmeter* and the Lock-In amplifier. Sample resistance was determined as

[1] Please refer to Chapter 2

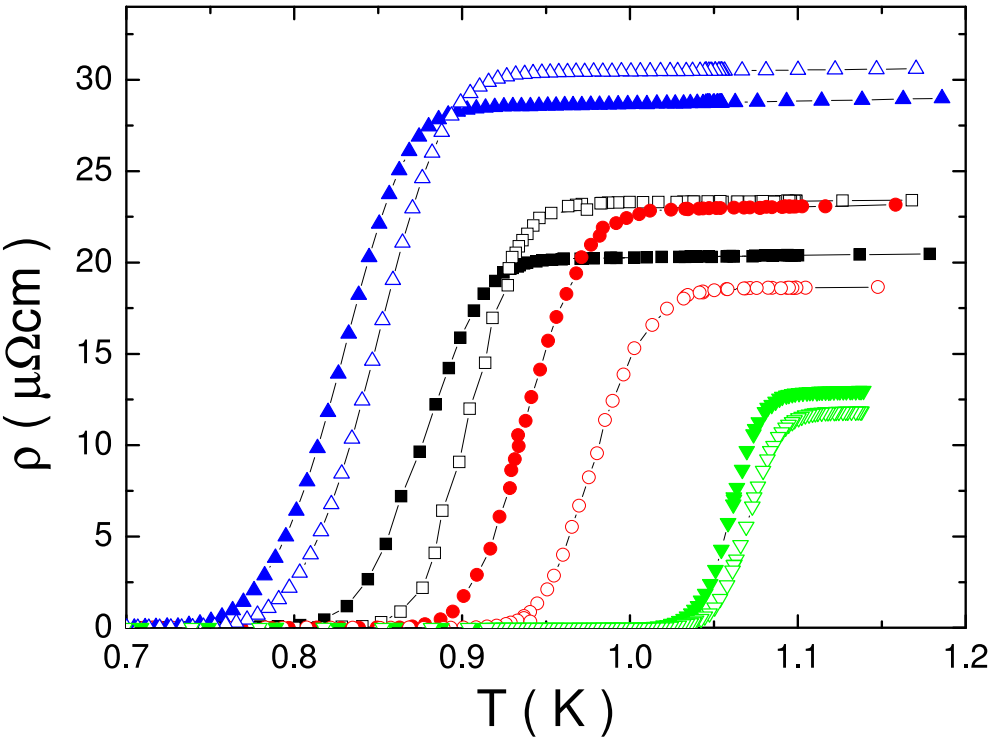

Figure 5.1: Resistive superconducting transitions for $I \| a$ (open symbols) and $I \| c$ (filled symbols) for different UNi_2Al_3 thin films (color coded).

function of current density, magnetic field and/or temperature. For some experiments, a magnetic field was generated by a superconducting solenoid built into the cryostat, which is energized by an $Oxford\ PS120$[10] magnet power supply.

5.2 Direction Dependence of the Resistive Superconducting Transition in UNi_2Al_3

A splitting of the resistive superconducting transition depending on the current direction was observed in UNi_2Al_3 (100) thin films [77, 97]. For $I \| a$, the drop of the eletrical resistivity appears at slightly higher temperatures compared to $I \| c$, as shown in Figure 5.1. This is a quite remarkable feature, since superconductivity is due to a thermodynamical phase transition at the temperature T_c. With no magnetic field applied, the resistance of the Cooper pair condensate is expected to vanish regardless of the direction.

At first, the effect was deduced from current redistribution effects in non

structured thin films [97]. The resistances measured by different (orthogonal) four point geometries showed a characteristic *drop* and *increase* behavior. The phenomenon was confirmed by measurements on samples with defined current paths along the respective directions, which were prepared by optical lithography [77, 97]. As possible origin also extrinsic reasons like sample imperfections etc. have to be considered.

Concerning the representative character of the observation, it is interesting to note that upon a closer inspection, also UNi_2Al_3 bulk single crystal data suggests a similar feature. However, the effect is close to experimental resolution and maybe therefore was not explicitly mentioned by the authors [76]. All structured thin film samples exhibited the same behavior, demonstrating that the splitting is indeed related to the crystallographic direction and is not caused e.g. by local variations in sample quality. There is no correlation to the overall sample crystalline quality as deduced from residual resistance or T_c (Figure 5.1).

A trivial reason for the splitting related to the UNi_2Al_3 thin film epitaxial growth on $YAlO_3$ can be ruled out from two sources. First, the absence of strain is proved by X-ray diffraction in two- and four-circle geometry [77, 97]. Second, the thin film morphology, measured by Atomic Force Microscopy (AFM) and displayed in Figure 5.2, is isotropic [79]. Although a pronounced island growth mode results in a considerable roughness of about 1/2 of the total film thickness, no anisotropy in the islands' shape, distribution or orientation is observed.

Two-Band Model

An explanation for the current direction dependence of T_c was proposed that is based on the existence of at least two, weakly coupled superconducting bands [77, 97]. In theory, superconductivity in two overlapping bands was considered already quite early after the formulation of the BCS theory [127]. In the case of two bands, e.g. s and d [2], the pairing Hamiltonian may be written as:

[2] The band type d is of no particular importance here. An f band may be treated the same way.

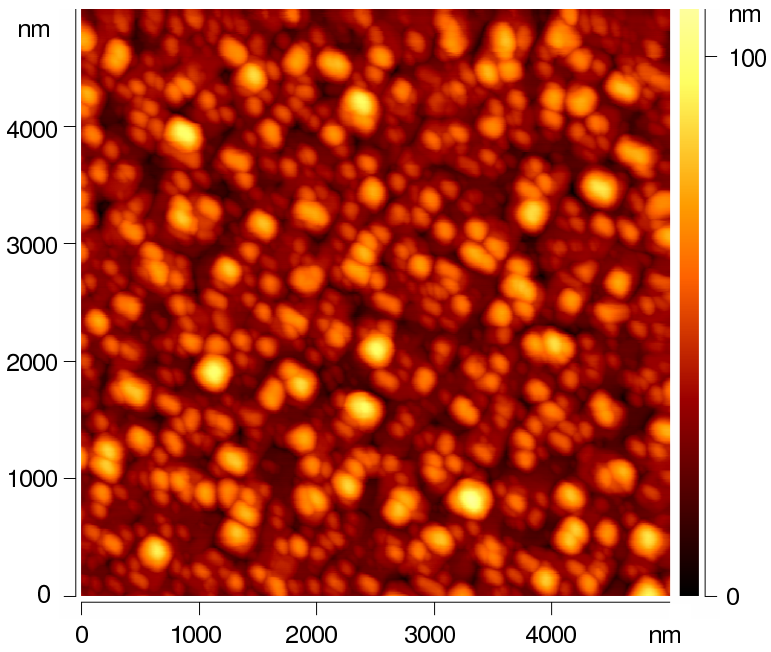

Figure 5.2: Morphology of a UNi_2Al_3 (100) thin film measured by AFM. Typical dimensions of the islands are 200-400nm in diameter and 30-80nm in height. Total film thickness is estimated 150nm from deposition rate measurements by X-ray reflectometry.

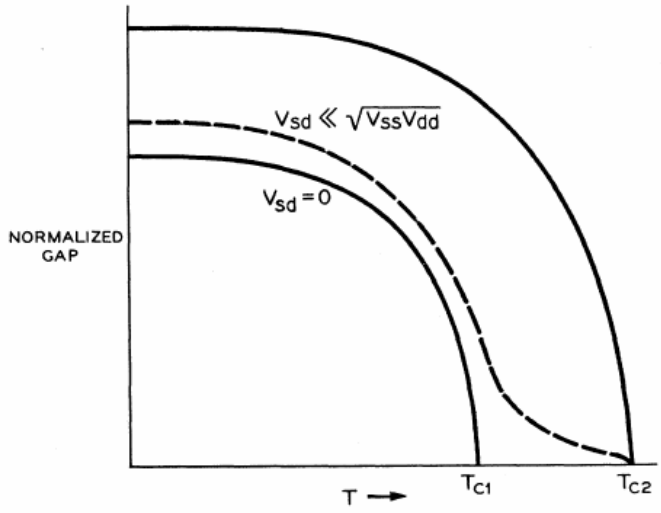

Figure 5.3: Theoretically expected, normalized energy gaps $\Delta(T)$ for two independent bands (solid lines) with only interband pairing, resulting in different T_{c1}, T_{c2}. In the more realistic case of weak coupling between the bands, two different energy gaps with one common transition temperature T_{c2} are found. The smaller gap is expected to behave as indicated by the dashed line. Figure is taken from Ref.[127].

$$H = \sum_{\vec{k}\sigma} \epsilon_{\vec{k}s} c^*_{\vec{k}\sigma} c_{\vec{k}\sigma} + \sum_{\vec{k}\sigma} \epsilon_{\vec{k}d} d^*_{\vec{k}\sigma} d_{\vec{k}\sigma}$$
$$-V_{ss} \sum_{\vec{k}\vec{k}'} c^*_{\vec{k}\uparrow} c^*_{-\vec{k}\downarrow} c_{-\vec{k}'\downarrow} c_{\vec{k}'\uparrow} - V_{dd} \sum_{\vec{k}\vec{k}'} d^*_{\vec{k}\uparrow} d^*_{-\vec{k}\downarrow} d_{-\vec{k}'\downarrow} d_{\vec{k}'\uparrow}$$
$$-V_{sd} \sum_{\vec{k}\vec{k}'} \left(c^*_{\vec{k}\uparrow} c^*_{-\vec{k}\downarrow} d_{-\vec{k}'\downarrow} d_{\vec{k}'\uparrow} + d^*_{\vec{k}\uparrow} d^*_{-\vec{k}\downarrow} c_{-\vec{k}'\downarrow} c_{\vec{k}'\uparrow} \right)$$

where V_{ss}, V_{dd} are the averaged intraband interaction energies and V_{sd} is the averaged interband interaction energy. In this Hamiltonian, the first two terms represent the band energies, while the next two terms cause the intraband pair formation. Finally, the last term describes the interaction between pairs in different bands.

Depending on the relative strength of the coupling energies, different outcomes of the above equation are possible. The resulting gap functions $\Delta(T)$ are shown in Figure 5.3. Assuming different values for $N_s V_{ss} \neq N_d V_{dd}$ and the unphysical case of zero interband coupling $V_{sd} = 0$, two gap functions of different size appear at different temperatures $T_{c1} < T_{c2}$ (solid lines). In the more realistic case of weak, but finite interband coupling ($V^2_{sd} << V_{ss} V_{dd}$), the smaller gap function is expected to behave as indicated by the dashed line. The splitting in T_c vanishes, and instead two gaps of different size open at the same temperature $T_c = T_{c2}$. However, close to the originally higher temperature T_{c2} the smaller gap is reduced drastically and only increases significantly around the original T_{c1}.

Now consider a scenario, in which the band with the bigger energy gap contributes only to the current in some specific direction. Any current in another direction has to be carried by the other band with the much smaller gap. In this case, already a small current density in the direction corresponding to the smaller gap may prove overcritical while the same current density is undercritical in the band with the bigger gap. Consequently, two different resistive transition temperatures will be observed.

The presumed Fermi surface of UNi_2Al_3 as shown in Figure 1.6 exhibits a pronounced anisotropy, with two sheets of cylindrical character around the *c*-axis and one more isotropic sheet. However, the existence of the latter is not certain. It should be noted that at least in the normalconducting state a perfect cylinder around *c* will contribute only to transport in the *ab*-plane since the Fermi velocity is perpendicular to the Fermi surface. In the *ab*-plane the higher resistive T_c is found.

Thus, the existence of two weakly coupled, anisotropic bands with different energy gaps in UNi_2Al_3 provides an plausible explanation for the experimental observation. In this framework, the splitting of the resistive transition temperature is due to critical current effects hiding the tiny energy gap. The band with the bigger gap is considered not to contribute to transport along the c-direction. This applies to the cylindrical sheet(s) around c.

Current Reduction

According to the two-band model, the splitting in T_c is expected to vanish for sufficiently small current densities corresponding to the size of the smaller energy gap close to T_{c2}. However, in the standard resistance measurement the lower limit for the current density is determined by the sensitivity of the voltage measurement. Consequently, a special *meander* structure (Figure 5.4) was developed containing long, narrow current leads to achieve highest possible absolute resistance. Reducing the current density from $j = 5\text{A/cm}^2$ down to $j = 0.1\text{A/cm}^2$ no shift of the transition in either direction was found [79, 97]. Both values are several orders of magnitude below the critical current density $j_c(0.4\text{K}) > 40000\text{A/cm}^2$. Although this experiment fails to provide direct support for the two-band model, it does not necessarily contradict it either. The temperature dependence of the critical current density might be weak. The reason is that in the range between T_{c1} and T_{c2} in Figure 5.3, the smaller gap changes only little as function of temperature.

Comparison with UPd_2Al_3

The dependence of the resistive transition on the current direction in UNi_2Al_3 has been a remarkable and unique observation. Searching for other examples exhibiting the same feature, the isostructural and isoelectronic UPd_2Al_3 is a obvious candidate. Although single crystals of UPd_2Al_3 have been available for quite some time, previous directional dependent measurements are not conclusive on this point, since two different samples were used [128]. Consequently, variations in the transition temperature are attributed to sample dependence.

With the availability of UPd_2Al_3 (100) thin films during this work (Chapters 2&3), it became possible to clarify this topic [129]. A UPd_2Al_3 (100) thin film sample was structured by optical lithography (Chapter 2) to measure resistance along the a- and c-axis, respectively. In Figure 5.5, the temperature dependent resistivity $\rho(T)$ of a structured UPd_2Al_3 thin film is shown for $I \| a$ and $I \| c$.

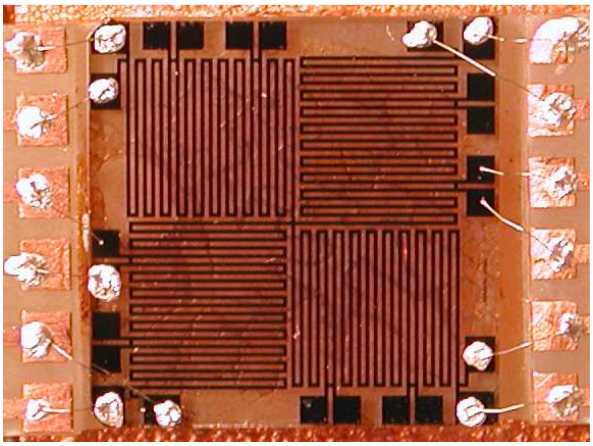

Figure 5.4: UNi_2Al_3 film in meander geometry for low current density measurements and other experiments requiring long current paths for both directions, $I\|a$ and $I\|c$, in one sample. Total respective length in the main direction is $L = 168$mm while the orthogonal connections amount to $l = 4$mm ($\equiv 2.4\%$) and the width is $b = 100\mu$m. Since the presumably best UNi_2Al_3 thin film sample ever made (highest T_c) was structured in this manner, further measurements were performed in this geometry.

The behavior in the normalconducting state agrees with data obtained on bulk single crystals before [128]. A relatively broad maximum of the resistivities is found around 100K. Above, the slope is more steep for $I\|c$ than for $I\|a$. In further agreement, the kink which is observed close to $T_N \approx 14$K is more pronounced for $I\|a$ than for $I\|c$. However, the ratio of the resistivities $\rho_{I\|c}(100\text{K})/\rho_{I\|a}(100\text{K})$ which is close to 1 in the thin film experiment, is approximately 1.4 for the bulk samples. This might be related to problems in measuring absolute values for bulk samples, e.g. arising from determining the exact sample geometry. Also variations between samples may play a role since two different volume single crystals were used.

In contrast to UNi_2Al_3, the temperature of the superconducting transition does not depend on the current direction in UPd_2Al_3 thin films (inset of Figure 5.5). The superconducting transition occurs for both current directions at the same temperature, which is slightly reduced compared to best bulk single crystals and (001) oriented thin films. The reduction of the transition temperature $T_c \approx 1.75$K, as well as the bigger transition width and the higher residual resistivity indicate a reduced sample crystalline quality concerning purity and homogenity. However, the directional dependence in UNi_2Al_3 is independent from the sample crystalline quality (see Figure 5.1). Therefore, it seems implausible that the

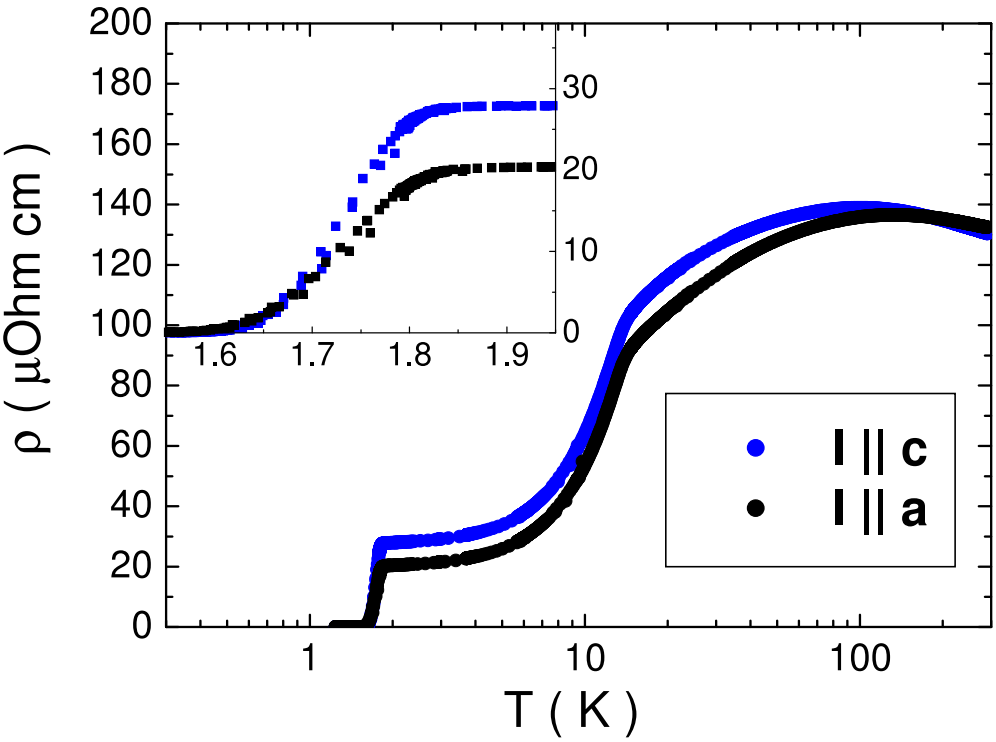

Figure 5.5: Temperature dependent resistivity $\rho(T)$ of a UPd_2Al_3 (100) thin film along the a- (open symbols) and c-axis (filled symbols). In the inset, the superconducting transition is shown in detail.

absence of such feature in UPd_2Al_3 should be related to the reduced crystalline quality of the (100) oriented thin films. Instead the splitting of the resistive transition has to be regarded a unique feature of UNi_2Al_3 until further examples are discovered.

On the other hand, the absence of the splitting in UPd_2Al_3 (100) thin films prove that the observation for UNi_2Al_3 is not an artifact connected to the specific experimental procedures. Deposition, lithography and measurement techniques are equivalent in both cases.

Evidence for Depairing at Low Current Densities

As was mentioned before, the superconducting resistive transition is not influenced by the current density at lowest levels. However, in an intermediate region ($5\mathrm{A/cm^2} < j < 5000\mathrm{A/cm^2}$) a dependence of both, the transition temperature and width on the current density is found. Exemplary resistive transitions for different current densities are shown in Figure 5.6. For high current densities

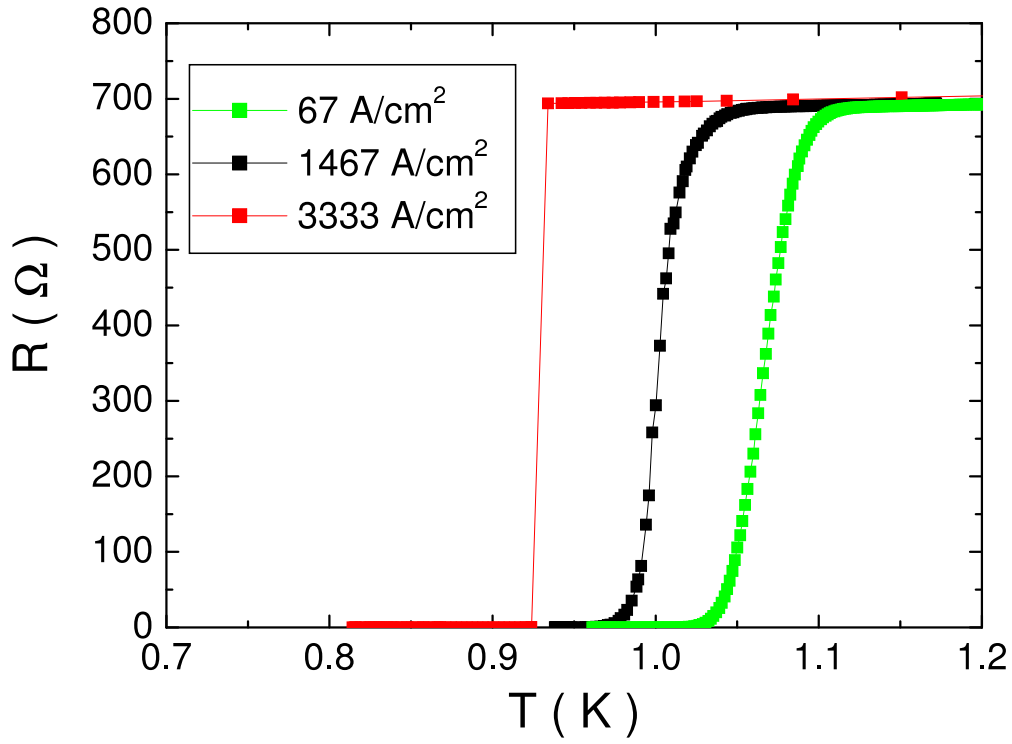

Figure 5.6: Superconducting resistive transitions in a UNi_2Al_3 thin film for different current densities. The behavior is equivalent for both current directions, $I\|a$ and $I\|c$, with the known shift in absolute temperature.

($j = 3333\mathrm{A/cm^2}$), there is an obvious change in the shape of the transition. For a quantitative study, the width of the superconducting transition, taken as the temperature difference between the 90% and 10% values of the resistance $R(T)$ is used (Figure 5.7). Concerning the transition shape, both current directions, $I\|a$ and $I\|c$, display the same behavior with the known directional splitting.

Above $j \sim 500\mathrm{A/cm^2}$, the transition width decreases rapidly. This can be ascribed to sample inhomogenities. At high current densities the whole conductor path crosssection is needed to carry the transport current. But there are parts of the sample where superconductivity is most weakly evolved due to crystal defects or impurities. When these parts start to become normalconducting either heat is generated by ohmic transport or the current is redistributed into other parts. Both effects can drive the whole sample that is already close to a critical state normalconducting instantly because the local cooling power is limited. Below $j = 500\mathrm{A/cm^2}$, the transition width increases slightly with j as expected due to the current dependence of the vortex dynamics.

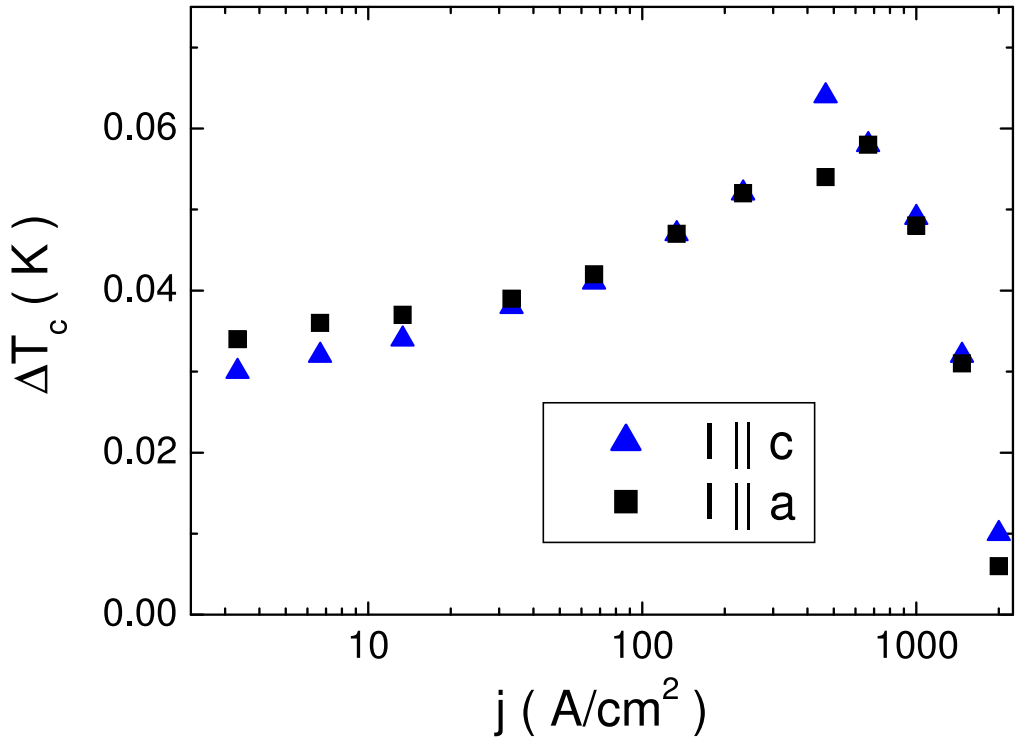

Figure 5.7: Width of the resistive superconducting transition in a UNi_2Al_3 thin film.

Additional to the broadening, the transition temperature is shifted by the current densitiy j, i.e. $T_c(j) < T_c(0)$. Because the shift is of similar size for $I\|a$ and $I\|c$, the directional splitting stays widely unaffected at current densities $j < 500\text{A/cm}^2$ (Figure 5.8, inset).

The splitting vanishes at highest current densities ($j \sim 2000\text{A/cm}^2$). This is probably due to the measurement geometry, which is the same meander structure (Figure 5.4) as used for lowest current densities. The conductor path contains small segments of the orthogonal direction. Thus, the original slightly higher T_c for $I\|a$ can be suppressed by the ohmic heating of the small connections where $I\|c$. Then the whole sample is driven normalconducting in a similar manner as discussed before for the transition shape.

No shift can be measured below $j = 5\text{A/cm}^2$ within the experimental resolution. Therefore, the shift of the midpoint of the resistive transition is taken with respect to $T_c(5\text{A/cm}^2) \approx T_c(0)$ (plotted in Figure 5.8). The shift can be understood to result from the temperature dependent critical current density $j_c(T)$. From Ginzburg-Landau (GL) theory, considering the intrinsic current dependence of the order parameter and assuming uniform current distribution (terms in $|\nabla\Psi|$

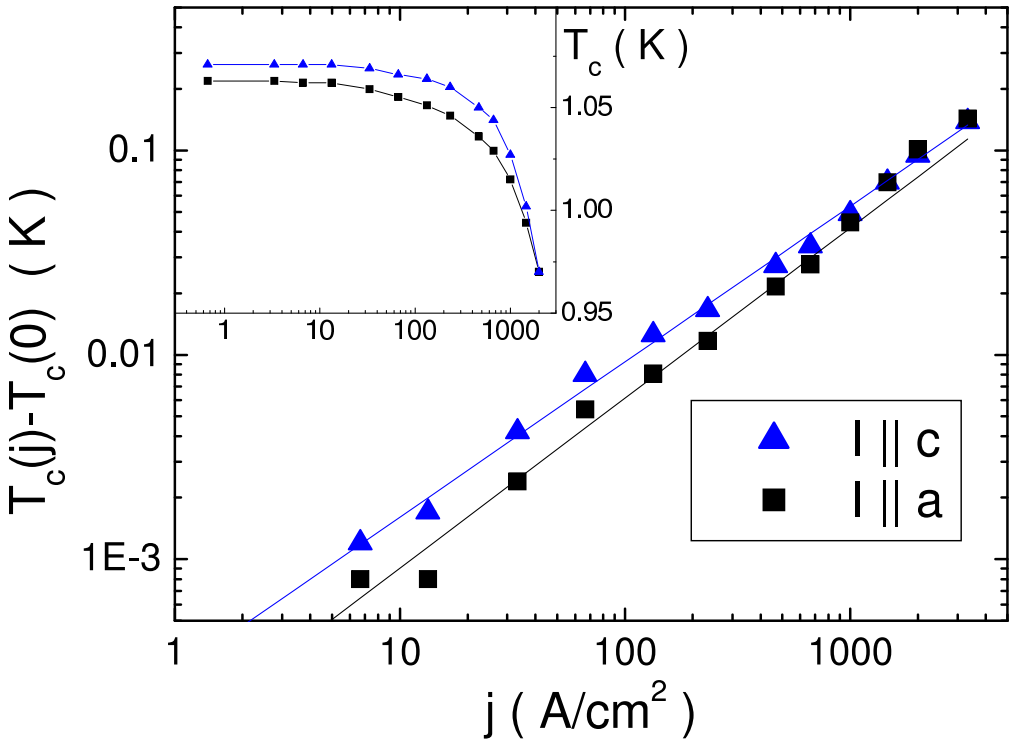

Figure 5.8: Shift of the resistive transition temperature of a UNi_2Al_3 thin film due to finite current densities in an intermediate range. The lines represent fitting functions as described in the text. Absolute values of T_c (midpoint) in the inset (here lines are guide to the eye only).

are neglected), the resulting shift follows a power law:

$$\frac{T_c(0) - T_c(j)}{T_c(0)} \propto j^z$$

with the exponent $z = 2/3$ for critical current depairing [7].

Fitting to the data for $j < 500\mathrm{A/cm}^2$ yields exponents $z = 0.83$ for $I \| a$ and $z = 0.76$ for $I \| c$. The difference to the GL value may be related to the fact that sample dimensions are not small enough compared to the coherence length χ to ensure a uniform current distribution. While the width of the conductor path in the experiment is $w = 100\mu m$, the coherence length is only $\chi_0 = 24nm$. But since $\chi(T)$ is expected to increase and finally diverge at T_c the starting assumption of $w \sim \chi$ is not completely unreasonable in the transition range. Additionally, the ohmic resistance of the sample in the transition region results in heating. However, if this heating was the dominant process, an exponent $z = 2$ would be expected [130], which deviates strongly from the experiment in this range. The high current density range, where heating is expected to play an important role,

was not further investigated to avoid damage to the sample. But an increase of the slope is already visible in the upper region of Figure 5.8.

In conclusion, the shift of T_c as function of current density indicates an intrinsic, critical current pairbreaking mechanism in the low and medium current density range. This also implies an intrinsic origin of the directional splitting in the resistive T_c. Heating contributions are only relevant for high current densities.

Vortex Dynamics

The directional splitting of the resistive transition in UNi_2Al_3 is small compared to the transition width (refer to Figure 5.1). Consequently, for most of the transition region the resistivities for both $I \| a$ and $I \| c$ are reduced with respect to the normalconducting values. The effect of the splitting is that the degree of the reduction for the two orientations is different at the same temperature. Since a finite resistance in the superconducting state can arise from the vortex dynamics in a type-II superconductor like UNi_2Al_3, an origin of the splitting related to the vortex dynamics might be considered.

In a magnetic field H, with $H_{c1} < H < H_{c2}$, a type-II superconductor is penetrated by magnetic flux vortices with normalconducting cores. For this mixed state, a current passing through the material results in *Lorentz* type forces acting on the vortices. In turn, movement of the vortices leads to a finite voltage drop along the superconducting current path.

In a real sample, the normalconducting vortex cores are pinned to crystal defects, minimizing the loss of condensation energy. Therefore, in the Anderson-Kim model [131, 132] the vortex dynamics are described based on the assumption of thermally activated jumps of parts of the vortex lattice against a pinning potential U_P. It results an electric field E:

$$E(j) = 2\rho_c j_c e^{-U_P/k_B T} sinh\left[\frac{jU_P}{j_c k_B T}\right]$$

with the current density $j_c = \frac{U_P}{BVl}$ and the resistivity $\rho_c = \rho(j_c)$, where V is the moved vortex lattice's volume and l the distance of one jump. In general, the properties V and l cannot be determined easily. While in reality a spectrum of values for the pinning potential U_P is expected, the exponential dependence will lead to a dominant contribution of the lowest value, thereby justifying the assumption of a single value.

Depending on the current density, typical ranges can be identified for the above relation $E(j)$. In the intermediate *flux creep* region $j \sim j_c$, the voltage depends exponentially on the current density $E(j) \propto exp(j/j_0)$. [3]

In Figure 5.9 the voltage-current characteristics $V(I)$ of a UNi_2Al_3 thin film for two current directions are shown for various magnetic fields at $T = 0.4$K. Since the resistivity caused by vortex dynamics is expected to be small, the meander structure (Figure 5.4) was used to achieve the biggest possible measurement range concerning current density. On the other hand, the orthogonal connections in the structure imply that for both parts of the structure superconductivity is limited by the crystallographic direction with originally lower critical current density. Consequently, the current densities where an abrupt transition to normalconductivity occurs are almost identical for $I\|a$ and $I\|c$ in Figure 5.9.

Below the transitions, finite resistances due to vortex dynamics are observed. In Figure 5.9 the red lines correspond to exponential fits $E(j) \propto exp(j)$, which characterize the flux creep regime. For $I\|c$ and intermediate magnetic fields ($\mu_0 H = 0.6$ and $\mu_0 H = 0.7$T) the identification of such regime is most clear. For higher magnetic fields and $I\|c$ as well as for $I\|a$, an identification of a flux creep regime in the experimental data is less obvious. In magnetic fields smaller than $\mu_0 H \sim 0.5$T, the transition to the normalconducting state appeared instantaneously in this experiment, driven by high current densities.

The clearly different slopes for $I\|a$ and $I\|c$ indicate an anisotropic pinning potenial U_P. Possible reasons for qualitively different pinning behaviors for the two current directions are morphological or an anisotropy in the order parameter itself. However, the pinning anisotropy is not strong enough to explain the current direction dependence of the resisitive T_c by vortex dynamics driven current density effects.

It should be kept in mind, that the circumstances under which these vortex dynamic effects can be identified are high current densities and a considerable applied magnetic field. Still only a small resistance results, orders of magnitude below the normalconducting one. On the other hand, the directional splitting of T_c is found at zero field, small current density and on a resistance level comparable to the normalconducting one. This makes an origin of the splitting related to vortex dynamics improbable.

[3] The other ranges are the region of thermally activated flux flow (TAFF) with ohmic characteristic at low current density and the flux flow (FF) regime at high current density, which reveals an approximately ohmic characteristic as well. [133]

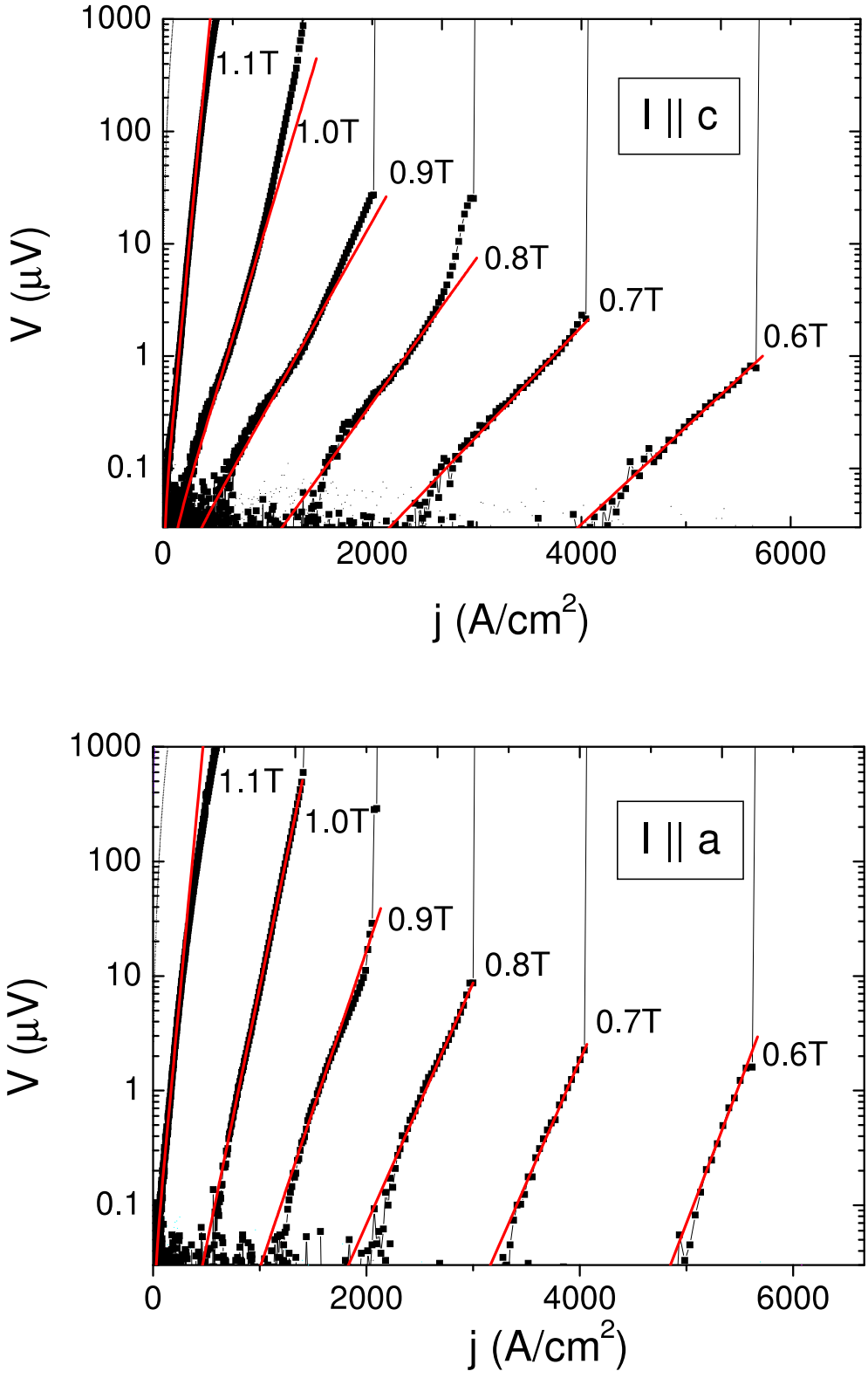

Figure 5.9: V(I) curves for a UNi_2Al_3 thin film at 0.4K for $I \| c$ (top) and $I \| a$ (bottom) in various magnetic fields. Fits represented by red lines correspond to exponential behavior of V(I).

5.3 Transport Anisotropy and Fermi Surface

In the previous section, the directional splitting of the resistive T_c in UNi_2Al_3 thin films is discussed. The two-band model provides a sound explanantion for this phenomenon, but a direct proof for it's validity is lacking. However, evidence against possible alternative explanations based on crystal defects or vortex dynamics is presented above.

One key assumption of the two-band model, namely the decoupling of electric transport along the a and c-axis, concerns the Fermi surface of UNi_2Al_3. Unfortunately, only a preliminary, unpublished calculation for the Fermi surface of UNi_2Al_3 exists to the author's knowledge (compare Chapter 1.4). The calculations indicate the existence of at least one, strongly two-dimensional sheet, which in principle allows for the decoupling mentioned before. Still, further arguments to justify this key assumption are highly desirable. They may be provided, if additional investigations of the transport anisotropy in either normal or superconducting state show indeed a decoupling of currents $I \| a$ from $I \| c$.

Angle Dependence of the Transition

Additional to the crystallographic a and c-axes, the resisitive superconducting transition was observed for further directions, using a specialized measurement geometry (Figure 5.10, inset). In this sample, it was found that absolute values of T_c are not reproducible in subsequent experiments for the same sample part and current density. On the other hand, the splitting of T_c and the shape of the transitions are reproducible. Apparently all temperatures values are shifted by the same magnitude. Two sources of variance occured. First, following high current driving ($j \approx 1000\mathrm{A/cm^2}$), a reduction in T_c was observed, which may be related to sample degradation. Second, after remounting and cooling down, T_c was slightly higher than in the beginning, but was again reduced after feeding high current densities.

The data shown in Figure 5.10 for $\alpha = 90^o$, 60^o, 30^o, 10^o and 0^o, where α denotes the angle with the c-axis, was taken simultaneously. For experimental constraints the data at 80^o had to be taken in additional measurements, hence it involves a correction. A shift of the absolute temperature was calculated from comparing the corresponding 90^o measurements with the reference 90^o measurement. Two data sets of 80^o from two different additional experiments are included, with good agreement. The corrections are 8mK and 19mK, respectively,

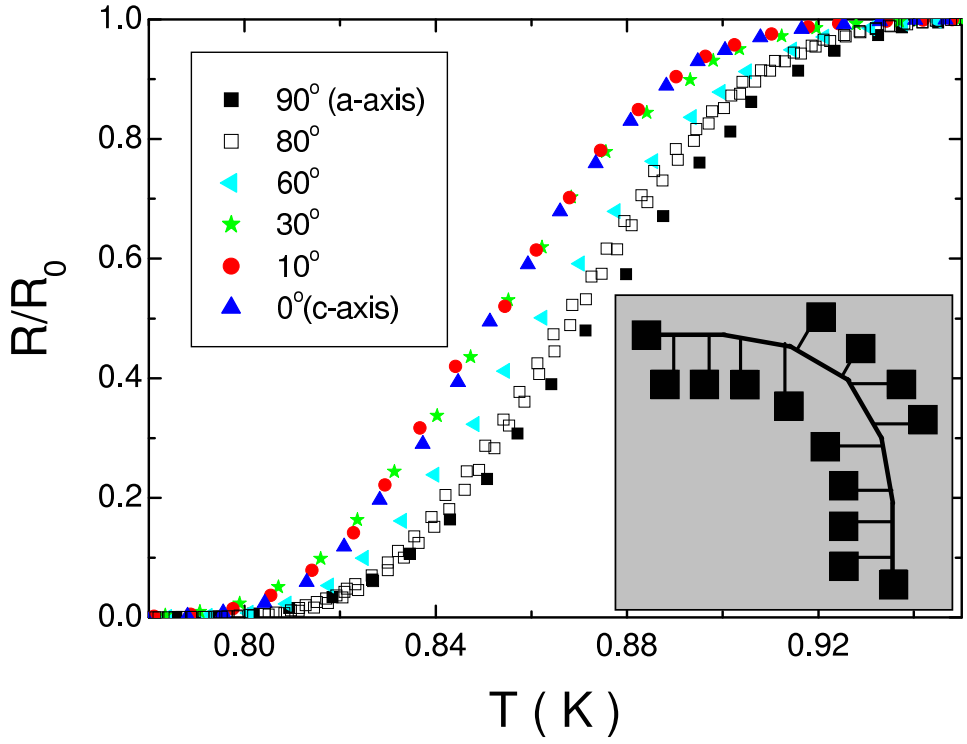

Figure 5.10: Resistive superconducting transition in a structured UNi_2Al_3 thin film for various crystallographic directions. The in-plane angle α is defined with respect to the c-axis. Schematic of the measurement geometry in the inset.

which is comparable to the total splitting. The agreement of two independent data sets including corrections justifies this procedure.

Since the resistive transition occurs at different temperatures for $I \| a$ and $I \| c$, it is necessary to consider the way of the current through the structure for different angles α. If e.g. transport in one direction is already superconducting while it is still normalconducting in the other, the current will take a zig-zag pattern inside the lead, thus minimizing the resistance. In general, for very different resistivities in two directions, the result of a measurement for α will be the superposition of contributions in the two basic directions. However, in this case (Figure5.10) the splitting of T_c is small compared to the transition width ΔT_c and thus the difference in resistivity for the two current directions is comparatively small at any temperature. Therefore, the transport current will flow straight along the geometrically shortest way, i.e. along the structured path. Then the measured resisistivity is intrinsic for the given direction.

As shown in Figure 5.10, the angular dependence of the resisitve transition is

not uniform. For example, for angles α between 0° and 30° , no significant change in the temperature dependence is observed. On the contrary, data for $\alpha = 80°$ already differs significantly from data for the *ab*-plane ($\alpha = 90°$).

For a better assessment of the angular dependence, the comparison with a simple model of anisotropic conductivity proves conclusive. For more clarity, details of the derivation are skipped and shifted to Appendix A6, only the basic assumptions will be mentioned here. Ohm's law for current density $\vec{j}$ and electric field $\vec{E}$ in 2 dimensions is used in the form:

$$\begin{pmatrix} j_c \\ j_a \end{pmatrix} = \begin{pmatrix} \sigma_c & 0 \\ 0 & \sigma_a \end{pmatrix} \begin{pmatrix} E_c \\ E_a \end{pmatrix} = \begin{pmatrix} \sigma_c E_c \\ \sigma_a E_a \end{pmatrix}$$

where the indices a and c denote components along the respective crystallographic directions. The off-diagonal elements of the conductivity tensor are zero since no magnetic field is applied. Further a homogenous current distribution is assumed for each segment ($\vec{j} = const.$). From above relation, using as input the measurements for $I \| a$ and $I \| c$ which yield $\sigma_c(T)$ and $\sigma_a(T)$, the transitions for other directions may be constructed.

The results of this model for $\alpha = 10°$, 30°, 60°, and 80° are shown in Figure 5.11 as lines, together with the corresponding experimental data (symbols of same color). There is a clear discrepancy between the experiment and the behavior expected according to the model. In particularly, the model predicts the decrease in the resistivies at higher temperatures than observed in experiment.

In other words, the conductivity for $I \| a$ deviates stronger from the other investigated directions than expected in the simple model of anisotropic conductivity for one electronic system. This indicates that the transport in a-direction is carried by another electronic subsystem or part of the Fermi surface than for the c-direction. As was stated before, this is one important assumption of the two-band model for the directional dependence of T_c.

Upper Critical Field H_{c2}

The structure of the Fermi surface is expected to be also reflected in the anisotropy of the upper critical field H_{c2}. Consequently, the upper critical field H_{c2} was determined from the resisitive transition $R(T)$ in different (concerning strength and orientation) magnetic fields H for both, $I \| a$ and $I \| c$. Since the width and the shape of the transition depend only weakly on the field H, the upper critical field $H_{c2}(T)$ was extracted using a midpoint criterion. In the $H \| c$ configuration, the

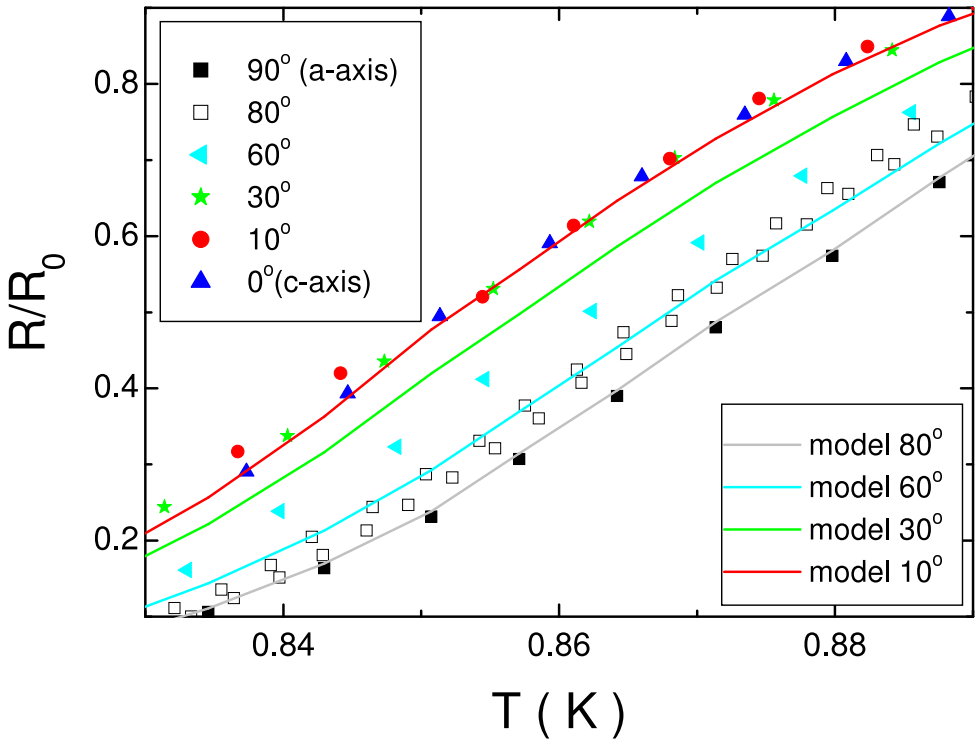

Figure 5.11: Resistive superconducting transition in a structured UNi_2Al_3 thin film for various crystallographic directions. Comparison of experimental data (symbols) with model (lines of same color). For details, please refer to the text.

field is parallel to the thin film surface, which in principle can lead to increased critical fields due to finite size effects (thin film and surface superconductivity). However, these phenomena should result in a pronounced angular dependence of $H_{c2}(\vartheta)$, which was not observed. It should be mentioned, that the results of Figure 5.12 are not completely new, in fact they are also featured in Reference [97]. They are presented in this work again, because from them important conclusions about the superconducting state in UNi_2Al_3 can be drawn.

The dependence of H_{c2} on the direction of the applied field shows similarities with UPd_2Al_3 [34]. Close to T_c, the initial slope dH_{c2}/dT and H_{c2} is smaller for $H\|c$, compared to $H\|a$. At around $T \approx 0.5$K the curves cross, which resembles the situation in UPd_2Al_3, where such crossing occurs at $T^* \approx 0.75T/T_c$ [34]. The relative difference in H_{c2} between the two field directions is slightly bigger for UNi_2Al_3 compared to the UPd_2Al_3.

According to the WWHM theory, taking into account only orbital interactions, the orbital upper critical field H_{c2}^{orb} of a type-II superconductor can be estimated

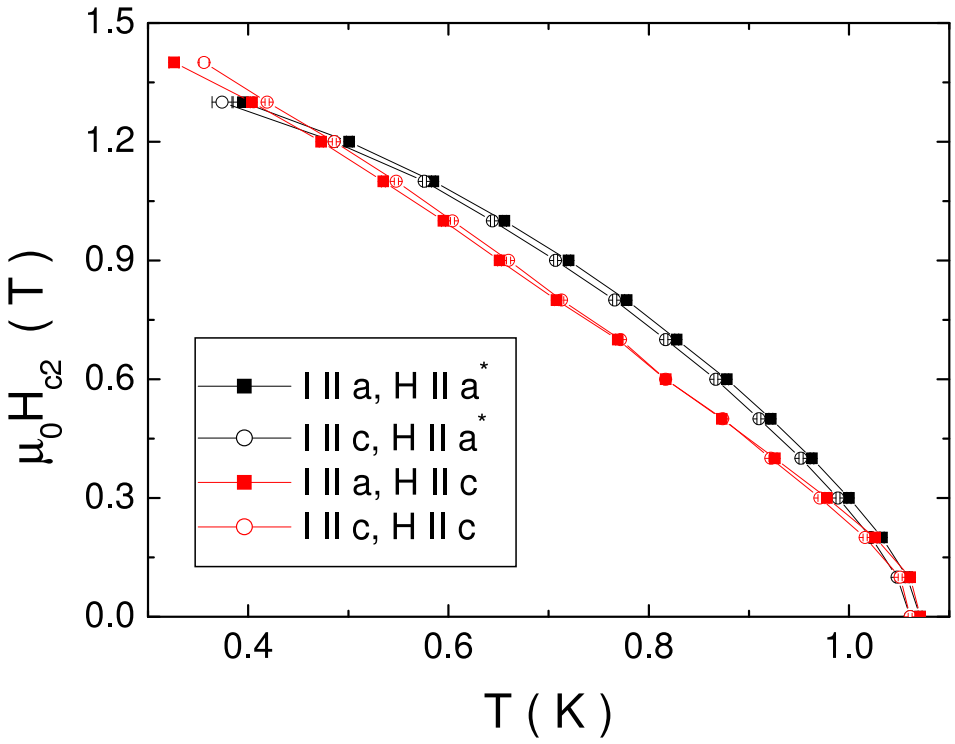

Figure 5.12: Upper critical field H_{c2} of a UNi_2Al_3 thin film for different field and current directions. H_{c2} is determined from the resistive transition $R(T)$ using a midpoint criterion.

from the slope $dH_{c2}/dT|_{T_c}$ [35, 36]:

$$H_{c2}^{orb} = 0.693(-dH_{c2}/dT|_{T_c}) \cdot T_c$$

The reason is that the pairbreaking at low fields is dominated by orbital interactions. If this rule is applied to the data of Figure 5.12, the resulting values are large, $\mu_0 H_{c2}^{orb}$ >5T. However, extrapolated experimental values $\mu_0 H_{c2}(0\mathrm{K})$ are much smaller, around $1.5 - 1.7$T only, depending on the field orientation. Also $H_{c2}(T)$ shows a pronounced curvature around T_c in contrast to the WWHM model which predicts only small deviations from linearity down to $\sim 0.5T_c$. Both facts signal a not negligible contribution of paramagnetic pairbreaking. Please note, that the Chandrasekhar-Clogstone limit for paramagnetic pairbreaking [7]:

$$\mu_0 H_{c2}^{p} = 1.84T/\mathrm{K} \cdot T_c \approx 1.95\mathrm{T}$$

is similar to the experimental values $\mu_0 H_{c2}(0\mathrm{K})$. The different curvatures for $H\|c$ and $H\|a$, as well as the crossing at $T \approx 0.5$K indicate an anisotropy of the paramagnetic pairbreaking, like it is observed in UPd_2Al_3, too [34]. The

observation of paramagnetic pairbreaking implies the realization of an opposite spin, most likely spin singlet pair state.

In contrast, NMR measurements in UNi_2Al_3 show no change of the Knight shift upon entering the superconducting state [78], which raises the question of a possible (equal) spin triplet pair state. The Knight shift of the central peak in the NMR spectrum is due to the field generated by polarized spins of conduction electrons or quasiparticles at the nuclei in the applied magnetic field. For an opposite spin pair state, the contributions from the paired electrons' or quasiparticles' spins cancel, resulting in a change of the Knight shift upon pair formation.

Upper critical fields determined for polycrystalline samples and bulk single crystals do not provide support to either side. On the one hand, they yield values for $H_{c2}(0\mathrm{K})$ which are similar to the ones expected from the slope $dH_{c2}/dT\|_{T_c}$ for orbital pairbreaking (see Table 1.1). But it should be pointed out, that although this is compatible with equal spin pairing, it does not allow a determination of the spin pair state. For these experiments, paramagnetic pairbreaking cannot be expected to play a dominant role anyway. In them, both $H_{c2}(0\mathrm{K})$ as well as the estimated H_{c2}^{orb} are strongly reduced and thus are smaller than the Chandrasekhar-Clogstone limit.

Until another explanation for either the lack of observing a change of the Knight shift or the particular $H_{c2}(T)$ behavior in thin films is brought forward, the contradiction has to be considered unresolved. However, the upper critical field measured for UNi_2Al_3 thin films cannot be explained in simple terms including only orbital pairbreaking.

Current Direction Dependence of H_{c2}

Additionally, in UNi_2Al_3 a dependence of H_{c2} on the current direction is observed (Figure 5.13). For the magnetic field applied in the *ab*-plane, the resistive transition occurs at slightly higher temperatures for $I\|a$ as compared to $I\|c$, which is expected from the splitting of T_c in zero field. The size of the splitting remains widely unaffected by increasing the magnetic field. Also for small fields $H\|c$, the resistive transition occurs at slightly higher temperatures for $I\|a$ compared to $I\|c$.

However, below $\mu_0 H \approx 0.6\mathrm{T}$, the splitting in Figure 5.13 (red color) changes sign, i. e. the transition temperature for $I\|a$ is lower than for $I\|c$. This striking

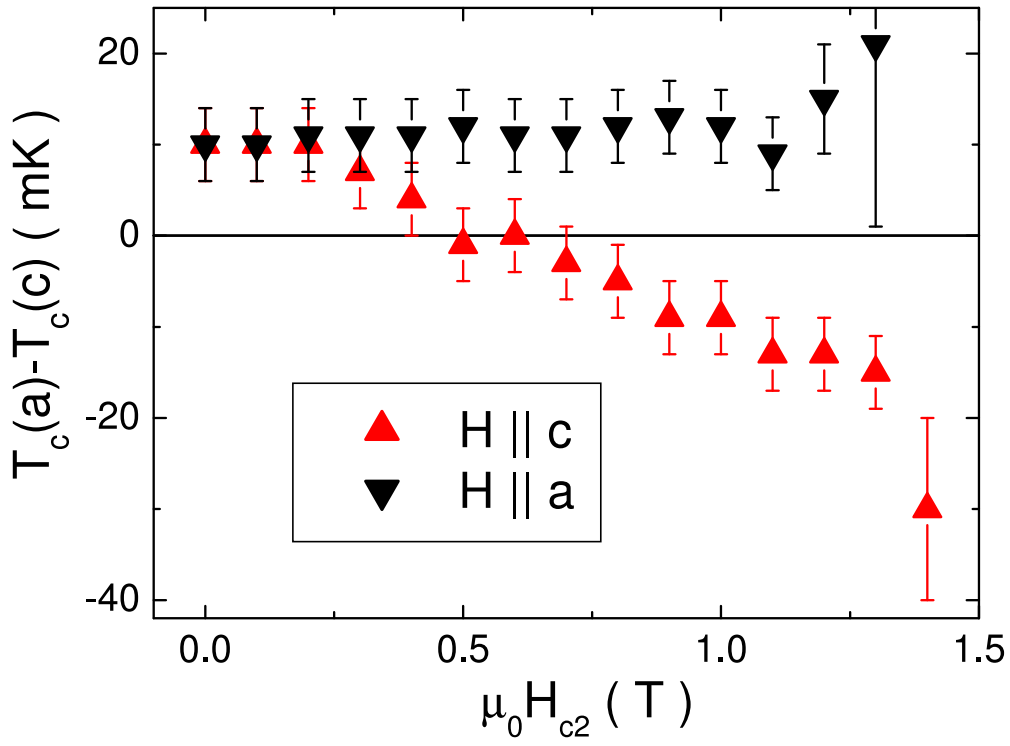

Figure 5.13: Splitting of the resistive transition as function of the applied magnetic field H. For $H \| c$, a change of sign occurs around $\mu_0 H \approx 0.6$T.

feature may be understood considering a simple argument concerning the interaction of transport and screening currents (around vortices). For $H \| c$, screening currents flow in the ab plane and are dominated by the cylindrical part of the Fermi surface. A transport current in the ab plane will give increased current densities in some parts leading to an earlier breakdown of superconductivity. On the contrary, a transport current along the c axis is orthogonal to the screening currents (and generated on a different sheet of the Fermi surface). It interacts only weakly with the screening currents, resulting in smaller sensitivity to the magnetic field.

First, these results prove again that the directional difference in T_c cannot be related to any spatial inhomogenity of the crystal quality. This is demonstrated by the fact, that depending just on the magnetic field strength, one or the other part of the measurement structure exhibits the higher resistive T_c. Second, the splitting is stable when the magnetic field is applied in the ab-plane. Together with the sign change of the splitting for $H \| c$, further evidence for the existence of (at least) two different, weakly coupled sheets of the Fermi surface is provided.

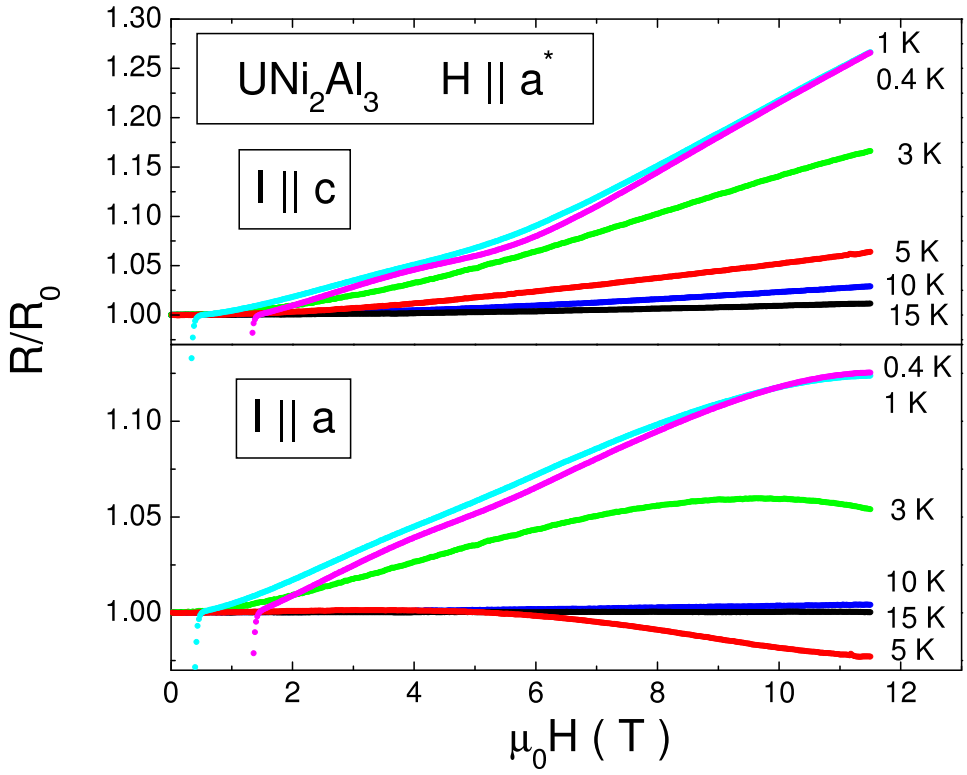

Figure 5.14: Normalized magnetoresistance $R(H)$ of a UNi_2Al_3 thin film with the field applied perpendicular to the surface. Temperature was stabilized by means of a capacitance sensor to rule out any influence of the field on the temperature sensor.

Magnetoresistance

Anisotropic transport properties were also observed in the normalconducting state. For example, for current directions in the ab-plane ($I \| a$ and $I \| a^*$), the temperature dependent resistivity $\rho(T)$ shows a kink signalling the onset of antiferromagnetic order at T_N which does not appear for $I \| c$ [77, 134]. Another signature of magnetic ordering is found in the magnetoresistance $R(H)$. When the current direction is parallel to the c-axis (Figure 5.14, top), the magnetresistance effect is purely positive, for all temperatures between $0.4-15$K. In contrast, for $I \| a$ (Figure 5.14, bottom) and high magnetic fields, a considerable negative contribtuion is present at temperatures close to T_N, namely at $T = 3$K and $T = 5$K. The decrease of the resistance $R(H)$ can be associated with less spin disorder scattering due to improved magnetic order induced in the sample by the external magnetic field.

Various experiments presented before gave compelling evidence that the transport along a- and c-axis are generated on different parts of the Fermi surface. The

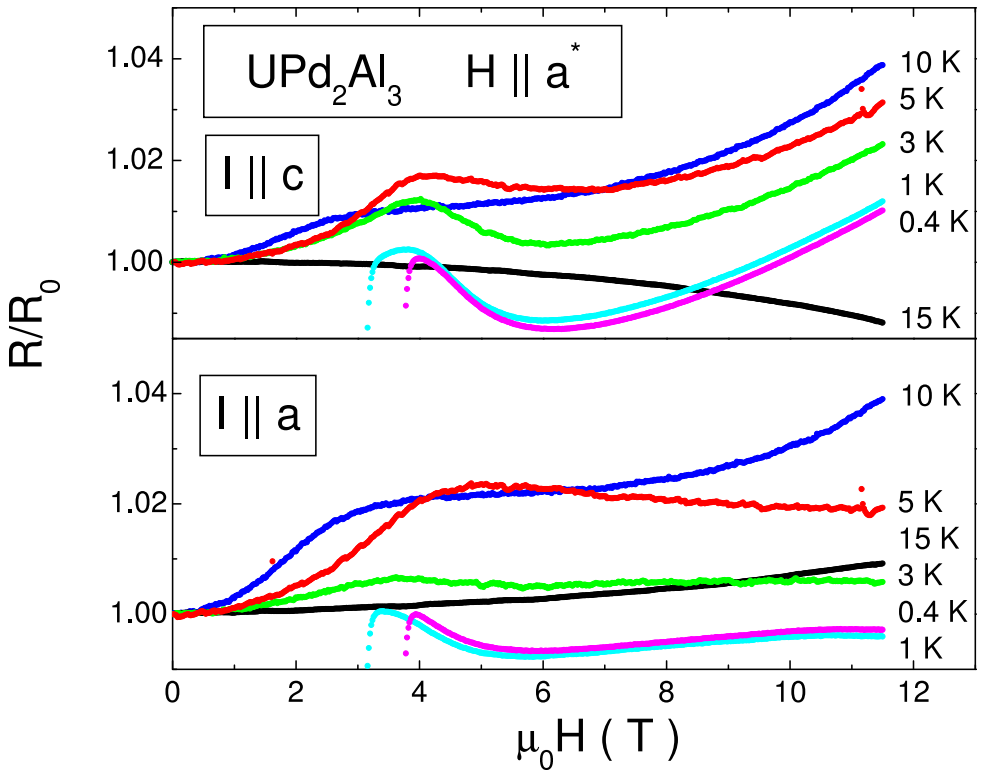

Figure 5.15: Normalized magnetoresistance $R(H)$ of a UPd_2Al_3 thin film with the field applied perpendicular to the surface.

part of the Fermi surface dominating a-axis transport is of strongly 2-dimensional, cylindrical character. Transport in a-direction, for both $R(T)$ and $R(H)$, is influenced by magnetic ordering, while staying unaffected in the c-direction. Consequently, the magnetic moments have to be ascribed to the cylindrical part of the Fermi surface. Weak coupling of the two subsystems causes the lack of any signature in c-direction.

Magnetoresistance in UPd_2Al_3

Compared with UNi_2Al_3, the magnetoresistance effect in equivalent UPd_2Al_3 (100) films is much smaller. The behavior (Figure 5.15) is characterized by different positive and negative contributions, of which not all are understood. A local maximum or shoulder occuring in the range between $\mu_0 H \approx 3$T and $\mu_0 H \approx 6$T was observed in (001) oriented films before [133]. The temperatures (5-6K) at which the feature is most strongly developed are similar in both kind of samples. In Reference [133] the feature is related to reorientation of magnetic domains in the applied field.

For $I \| c$, all curves $R(H)$ except the one for $T = 15$K show an increase at high fields H. The negative magnetoresistance close to $T_N = 14.3$K can be explained in a similar manner like for UNi_2Al_3 by a reduction in spin disorder scattering. A clear difference between UPd_2Al_3 and UNi_2Al_3 is marked by the appearance of a negative magnetoresistance close to T_N for $I \| c$ instead of $I \| a$. However, principle differences do not come surprisingly, since the properties of the magnetic order are quite different concerning size and character of the ordered magnetic moments (localized vs. spin density wave).

No direct sign of the magnetic order is present in the magnetoresistance $R(H)$ of UPd_2Al_3 for $I \| a$. Also a reduction of the resistance is observed, but it occurs at lower temperatures considerably below T_N. At $T = 15$K and $T = 10$K, the positive contribution to the magnetoresistance is dominating, while for 5K and 3K the negative contribution is stronger in the investigated field region. Qualitatively, the behavior for both current directions is similar, but the size of the positive contribution is clearly reduced for $I \| a$.

Summary

The present work addresses the electronical properties of the superconductors UPd_2Al_3 and UNi_2Al_3 on the basis of thin film experiments. These isostructural compounds are ideal candidates to study the interplay of magnetism and superconductivity due to the differences of their magnetically ordered states, as well as the experimental evidence for a magnetic pairing mechanism in UPd_2Al_3.

Epitaxial thin film samples of UPd_2Al_3 and UNi_2Al_3 were prepared using UHV Molecular Beam Epitaxy. The analysis of the epitaxial growth of UPd_2Al_3 (001) on $LaAlO_3$ (111) and UNi_2Al_3 (100) on $YAlO_3$ (112) & (010) reveals similarities, which motivated the attempt to deposit UPd_2Al_3 on $LaAlO_3$ cut in the alternative (110) direction. For the $LaAlO_3$ (110) substrate, the predicted change of the UPd_2Al_3 growth direction from the intrinsic (001) to the epitaxial (100) was successfully demonstrated. The change of the epitaxial growth direction for a relatively complicated, ternary compound is a remarkable achievement. Deposition process parameters for UPd_2Al_3 (100) oriented films were optimized, and turned out to differ significantly from the ones for (001) orientation. Accordingly, a considerable dependence of the deposited sample's stoichiometry on the growth direction was proved using Rutherford-backscattering spectroscopy.

Samples with (100) orientation prepared in optimized conditions revealed all characteristic crystallographic and electronic properties of UPd_2Al_3 as known from bulk single crystals and (001) films. Magneto transport properties $R(H)$ and $R_H(T)$ were also found to agree with measurements on (001) thin film samples. However, the slightly reduced superconducting transition temperature and the higher residual resistance in (100) oriented thin films indicate a higher defect density compared to the best conventional samples.

With the availability of this new sample class, additional experimental opportunities are created. Two of them were realized during this work. First, UPd_2Al_3 (100)-AlO_x-Ag tunneling junctions were prepared to investigate the superconducting density of states along the (100) direction and to search for eventual

indications of strong coupling features. Junctions in the tunneling regime with superconducting UPd_2Al_3 base electrode were obtained. However, no signature of the energy gap Δ was found in the tunneling spectra. This might be related to a strong pairbreaking effect of the (100) surface. Pairbreaking at the (100) surface could also explain the absence of signatures of superconductivity in the tunneling spectra of UNi_2Al_3 (100) based junctions [97]. However, alternative explanations such as junction defects cannot be ruled out completely.

Further, the resistive superconducting transition was probed for a possible dependence on the current direction. The existence of such a feature was excluded for UPd_2Al_3 (100) thin film samples. This indicates that the observation in UNi_2Al_3 is not related to the experimental techniques, which are the same for both materials. In fact, the differences between the two compounds concerning this phenomenon can be understood considering their respective Fermi surfaces.

The second focus of this work is the dependence of the resistive superconducting transition in UNi_2Al_3 on the current direction. The experimental fact that the resistive transition occurs at a slightly higher temperature for $I \| a$ than for $I \| c$ can be explained within a model of two weakly coupled superconducting bands. In this framework, two energy gaps of extremely different size open at one common T_c on different parts of the Fermi surface. Since the presumably cylindrical part with the bigger gap contributes to electrical transport only in the *ab*-plane, the smaller gap is hidden by critical current effects for currents along the *c*-axis.

In this work, evidence is presented for the key assumption of the two-band model, namely that transport in and out of the *ab*-plane are generated on different, weakly coupled parts of the Fermi surface. The superconducting transition was measured for four different angles between the *a*- and *c*-axis. Results were compared with the predictions of a model for anisotropic transport in one band. The actual angle dependence of the transition deviates clearly from the modeled behavior, in particular for angles close to the *a*-axis. Therefore it is concluded that transport is generated by two different electronic subsystems, with one being restricted to angles $\alpha < 10^{\circ}$ relative to the *a*-axis.

Measurements of the upper critical field B_{c2} revealed a sign change of the splitting for $H \| c$ around $\mu_0 H \approx 0.6$T but not for $H \| a$. This proves again that the splitting is not caused by spatial inhomogeneity of the crystal quality. In fact, the sign change can be explained considering the interaction of transport and screening currents around vortices, if the Fermi surface indeed has the properties

assumed in the two-band model.

Additionally, several possible alternative explanations for the directional splitting have been addressed in this work. No correlation of the magnitude of the splitting with the crystal defect and impurity density as deduced from the residual resistance ratio RRR and transition temperature T_c was found. Therefore an origin due to scattering on crystal defects or impurities can be exluded.

Upon varying the current density magnitude, two different regimes were observed. For high current densities $j > 500\mathrm{A/cm}^2$, the transition width decreased rapidly, indicating ohmic heating in the sample. However, in the current densitiy range $5\mathrm{A/cm}^2 < j < 500\mathrm{A/c}^2$, the shift $T_c(0) - T_c(j)$ behaves as predicted by the Ginzburg-Landau theory for critical current depairing. No indications of ohmic heating are found in this regime. Thus the significance of critical current depairing, which is supposed to be the mechanism supressing superconductivity for $I \| c$ in the two-band model, is demonstrated.

The voltage-current curves $V(I)$ in the superconducting states were measured in magnetic fields up to $\mu_0 H = 1.1\mathrm{T}$. A region with exponential behavior $E(j) \propto exp(j/j_0)$ was found at intermediate field strength, corresponding to the flux creep regime in the Anderson-Kim model. The pinning potenial is anisotropic, however, this anisotropy is not sufficient to explain the directional splitting of the resistive transition by vortex dynamics driven effects. The characteristics of the mixed state in terms of resistance and current density are radically different from the conditions under which the directional splitting is observed. Therefore an origin related to vortex dynamics is excluded.

In conclusion, all experimental observations are consistent with the two-band model while several alternative explanations were ruled out. Based on these findings, the directional splitting of the resisitive transition has to be considered an intrinsic and unique property of UNi_2Al_3. UNi_2Al_3 is proposed as a role model for weakly coupled multiband superconductivity.

Further, in the magnetoresistance $R(H)$ of UNi_2Al_3, a negative contribution was found only for $I \| a$ but not for $I \| c$ close to $T_N \approx 4.6\mathrm{K}$. This indicates that the ordered magnetic moments have to be assigned to the cylindrical part of the Fermi surface, in agreement with the characteristics of temperature dependent transport $R(T)$ [97].

For UPd_2Al_3, magnetic pairing scenarios have been proposed based on experimental evidence from tunneling spectroscopy and inelastic neutron scattering [20, 43, 51]. In principle, the fact that superconductivity is more strongly evolved

on the same part of the Fermi surface to which the magnetic moments are assigned seems to fit with the realization of a magnetic pairing in UNi_2Al_3as well. However, a future approach to the pairing mechanism in UNi_2Al_3 must take into account the pairing in both bands, as well as the differences in the magnetically ordered state in comparison with UPd_2Al_3.

Appendix A

A.1 Evaporation Rate Comparison based on XTC Settings

To calculate the effective ratio of evaporated atoms of different materials, the following comment is useful. The varied parameter in the optimization process is the material density setting of the XTC controller and not the measured growth rate since the density setting offers more digits than the rate measurement. All other characteristics of the monitor system like geometry, tooling factors, acoustic impedance etc. are assumed to be equal or calibrated.

The quantity actually measured by the XTC is the change of the crystal mass $\dot{m}$[1], which relates as:

$$\dot{m} = A\dot{d}\rho$$

with the thickness growth rate $\dot{d}$ (control parameter of the XTC), the crystal area A and the actual density setting ρ of the XTC. The number of incoming atoms $\dot{n}$ in units of N_A is given by:

$$\dot{n} = \dot{m}/M$$

where M is the molar mass. Thus the ratio of incoming atoms for equivalent monitors is:

$$\frac{\dot{n}_1}{\dot{n}_2} = \frac{\rho_1}{\rho_2} * \frac{M_2}{M_1} * \frac{\dot{d}_1}{\dot{d}_2}$$

where the thickness growth rate ratio $\dot{d}_1/\dot{d}_2$is a redundant parameter; a typical choice is $\dot{d}_1/\dot{d}_2 = 1$. The real material densities are not needed for this comparison.

[1]Deduced from the oscillation frequency change

A.2 Deposition of a Junction Stack

Sample UPA 99 in (100) orientation

Preparations

- Clean substrate ($LaAlO_3$ (110)) thoroughly with aceton, water and isopropanol
- Glue substrate on substrate holder with silver paint and allow to dry in rough vacuum (a shadow mask covering a part of the edge may produce a stripe for controlling ion beam etching progress when removed before the counter electrode deposition)
- In the deposition chamber, temper substrate at $T_{thermocouple} = 1000^oC$ for at least 1h
- Preoperate e-beam evaporators to clean evaporants and to reduce contamination released by heated surfaces

UPd_2Al_3 Base Electrode

- Substrate deposition temperature $T_{thermocouple} = 750^oC$; $T_{pyrometer} \approx 650^oC$
- Al e-beam evaporator *ESV 4*: amorphous Al_2O_3 (Frialit) crucible liner, beam voltage $U = 4kV$, beam current $I = 48mA$
- Al - XTC settings: gain:30%, approach:2, density:5.35g/cm^3, rate:1.0Å/s, z-ratio:1.08, tooling factor:100, nominal thickness:1804Å
- Pd e-beam evaporator *ESV 6*: graphite crucible liner, beam voltage $U = 8kV$, beam current $I = 50mA$
- Pd - XTC settings: gain:30%, approach:3, density[2]:19.07g/cm^3, rate:1.0Å/s, z-ratio:0.358, tooling factor:100, nominal thickness:1800Å
- U e-beam evaporator *ESV 4*: graphite crucible liner, beam voltage $U = 8kV$, beam current $I = 90mA$

[2]Conversion factor for nominal thickness between *ESV4* and *ESV6* from different mounting position: 1.3; i.e. $\rho_{ESV6} \hat{=} 1.3\rho_{ESV4}$

- U - XTC settings: gain:20%, approach:0, density:10.88g/cm^3, rate:1.2Å/s, z-ratio:0.238, tooling factor:100, nominal thickness:2140Å
- Deposition pressure: rising from $p_{0s} = 1.7 * 10^{-6}$mbar to $p_{1600s} = 4.7 * 10^{-6}$mbar
- RHEED: strong 0th order and 1st order after 500s, remains unchanged

Barrier

- Cool down to 100°C in ∼1h
- Deposition of Al from e-beam evaporator: 45s at 1.0Å/s and $\rho = 5.35$g/cm^3; real thickness ≈ 30Å
- UHV transfer to junction preparation chamber
- Remove control stripe shadow mask (if applicable)
- Fill junction chamber with $p_O = 0.4$mbar O_2 and add slowly Ar; final pressure $p_{total} = 0.8$mbar
- Oxidize for 40s with plasma discharge, sample facing the oxidization cathode (covered with Al foil)

Counter Electrode

- Flush junction chamber with Ar and pump several times
- Wait for at least 30min with Turbo pump working to remove remaining O_2
- Presputtering of Ag cathode for 5min (or until conditions are stable) at $U = 300$V, $I = 11$mA and $p_{Ar} = 0.15$mbar
- Turn sample to face cathode and deposit Ag counter electrode (6min≙1000Å)

A.3 Lithography Protocol

Thin film structuring process protocol from the 25.2.2005

- Clean sample in aceton in an ultrasonic bath and blow dry with pressurized air
- Check sample in an optical microscope, if necessary repeat step 1
- Coat with photoresist AZ-6612 on the spinner; apply with pipette and distribute at 6000rpm for 35s
- Bake for 16min at 100°C on a hotplate in an oven
- Expose for 60s to the light of an Hg-vapor lamp; photomask in contact with surface
- Develop in NaOH (0.1 molar) for 50s, then rinse with water
- Ion beam etching; etching should be continued for some time (∼4min) after the film is not visible anymore
- Remove residual photoresist with aceton in an ultrasonic bath and blow dry with pressurized air

A.4 Mesa Lithography Protocol

Mesa structuring process protocol from the 29.5.2007

- Remove coarse silver glue by softly sweeping with the sample backside over a tissue wetted with aceton
- Clean sample on spinner by rinsing first with aceton, then water
- Coat with photoresist ma-P 1215 on the spinner; apply with pipette in short distance, no rotation; distribute for 10s at 300rpm, then flatten at 3000rpm for 30s
- Bake for 90s at 100°C on a Cu-plate on top of a hotplate, then remove Cu-plate with sample to slowly cool down

- Expose for 40s to the light of an Hg-vapor lamp; photomask (mesa) in contact with surface
- Develop with ma-D 331 on the spinner; apply and wait for 45s without rotation, then 15s at 300rpm while rinsing with water, spin dry at 4000rpm for 15s
- Ion beam etching under 70° angle; if the etching rate is not known well enough, use a control stripe/sample with only an equivalent top electrode; etching should be continued for some time (∼4min) after the top electrode is not visible anymore
- Remove residual photoresist with aceton in a ultrasonic bath; use spinner and rinse with aceton for final cleaning
- Coat with Su8-2002; apply with pipette in short distance without rotation; distribute for 5s at 500rpm, then flatten at 3000rpm for 30s
- Slowly (8min) heat to 95°C on a Cu-plate on top of a hotplate, keep for 90s, then remove Cu-plate with sample to slowly cool down
- Expose for 40s to the light of an Hg-vapor lamp; photomask (window) in contact with surface
- Slowly (6min) heat to 95°C on a Cu-plate on top of a hotplate, keep for 60s, then remove Cu-plate with sample to slowly cool down
- Develop with XPSU-8 on the spinner; apply and wait for 75s without rotation, then 15s at 300rpm while rinsing with isopropanol, spin dry at 4000rpm for 15s

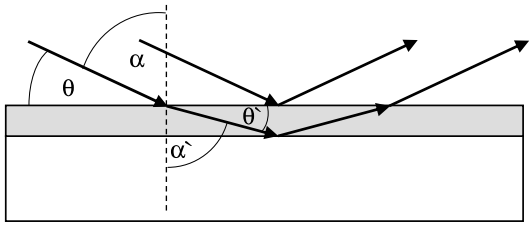

Figure A.1: X-ray refraction on the air-film interface causing error in thickness determination.

A.5 Refractive Index in X-ray Reflectometry

The error arising from the refractive index of the thin film for thickness determination by X-ray reflectometry can be estimated as follows. The approximated thickness d^* is calculated using Bragg's law:

$$m\lambda = 2d^* sin\theta$$

Typically the refractive index for X-rays in metals is $n = 1 - \delta$ with $\delta \sim 10^{-6}$ [103]. Then Bragg's law reads:

$$m\lambda' = 2dsin\theta'(*)$$

where $\lambda' = \lambda/n = \lambda/(1-\delta)$ is the wavelength inside the material and d the real film thickness. The angle θ' follows from Snellius' law (Figure A.1):

$$\frac{1}{n} = \frac{sin(90^o - \theta')}{sin(90^o - \theta)} = \frac{cos\theta'}{cos\theta}$$

θ and θ' are small (around 1^o), so the $cos\theta$ function is approximated by the Taylor expansion $1 - \theta^2/2$ and it follows:

$$\theta'^2 = \frac{\theta^2 - 2\delta}{1-\delta}$$

Inserting θ' and λ' into $(*)$ and approximating $sin\theta'$ by θ':

$$\frac{m\lambda}{2d} = (1-\delta)\sqrt{\frac{\theta^2 - 2\delta}{1-\delta}} = \sqrt{\theta^2 - 2\delta - \delta\theta^2 + 2\delta^2} \approx \theta - \delta/\theta$$

where the Taylor expansion for the square root was used and the two latter terms inside were neglected. Thus the estimated thickness d^* relates to the real thickness d as:

$$\frac{d^*}{d} = \frac{\theta - \delta/\theta}{\theta} = 1 - \frac{\delta}{\theta^2}$$

and the error $(d^* - d)/d$ is around 0.3% for $\theta = 1^o$ and $\delta = 10^{-6}$.

A.6 Model for Anisotropic Conductivity and Resistive Transition

Starting from Ohm's law for current density $\vec{(}j)$ and electric field $\vec{E}$, which may be written in 2 dimensions as follows:

$$\begin{pmatrix} j_c \\ j_a \end{pmatrix} = \begin{pmatrix} \sigma_c & 0 \\ 0 & \sigma_a \end{pmatrix} \begin{pmatrix} E_c \\ E_a \end{pmatrix} = \begin{pmatrix} \sigma_c E_c \\ \sigma_a E_a \end{pmatrix}$$

where the indices a and c denote the components along the respective crystallographic directions. In the anisotropic case, the electric field $\vec{E}$ is not parallel to the current density $\vec{j}$. The current density is assumed to be homogenous and thus must be parallel to the conductor path $\vec{r}$, enclosing the angle α with the c-axis:

$$\vec{j} = j \begin{pmatrix} cos(\alpha) \\ sin(\alpha) \end{pmatrix} = \begin{pmatrix} j_c \\ j_a \end{pmatrix}$$

However, in this experiment the observable is the total voltage U dropping over (a segment of) the current path at a fixed current density j. Then the voltage, again for the homogenous case, is given by:

$$U = \vec{E} \cdot \vec{r} = (E_c cos(\alpha) + E_a sin(\alpha))r$$

using $E_{c,a} = \frac{1}{\sigma_{c,a}} j_{c,a}$ from the first relation and $j_c = j cos(\alpha)$ from the second, it follows the proportionality

$$U \propto \frac{1}{\sigma_c} cos^2(\alpha) + \frac{1}{\sigma_a} sin^2(\alpha)$$

where the conductor path's length r and the current density j are taken into the proportionality constant. However, the measured voltage will depend on the temperature T as well as on the angle α. The transition can be characterized by the quantity $B(T, \alpha)$, which is defined with respect to a temperature just above the transition $T_0 = 0.95K$ (in this sample):

$$B(T, \alpha) = \frac{U(T, \alpha)}{U(T_0, \alpha)} = \frac{\frac{1}{\sigma_c(T)} cos^2(\alpha) + \frac{1}{\sigma_a(T)} sin^2(\alpha)}{\frac{1}{\sigma_c(T_0)} cos^2(\alpha) + \frac{1}{\sigma_a(T_0)} sin^2(\alpha)}$$

Possible values of $B(T, \alpha)$ range between 0(transition complete) and 1(above transition). The temperature dependent conductivities $\sigma_c(T)$, $\sigma_a(T)$ are known from measurements at $\alpha = 0^o$ and 90^o:

$$\frac{1}{\sigma_c(T)} = \frac{1}{\sigma_c(T_0)} \frac{U(T, 0^o)}{U(T_0, 0^o)} = \frac{1}{\sigma_c(T_0)} C(T)$$

and

$$\frac{1}{\sigma_a(T)} = \frac{1}{\sigma_a(T_0)} \frac{U(T, 90^o)}{U(T_0, 90^o)} = \frac{1}{\sigma_a(T_0)} A(T)$$

with $C(T) = B(T, 0^o)$ and $A(T) = B(T, 90^o)$. After introducing an experimental constant, the ratio $x = \frac{\sigma_a(T_0)}{\sigma_c(T_0)} = 0.956$, the quantity $B(T, \alpha)$ may be finally written as:

$$B(T, \alpha) = \frac{xC(T)cos^2(\alpha) + A(T)sin^2(\alpha)}{x \cdot cos^2(\alpha) + sin^2(\alpha)}$$

where the denominator is just a normalization constant. Thus, this model allows to construct an expected behavior $B(T, \alpha)$ for any α, with input only from the measurements at $\alpha = 0^o$ and 90^o.

Bibliography

[1] M. Jourdan, *Tunneling spectroscopy of the heavy-fermion superconductor* UPd_2Al_3, PhD-thesis (1999), Institut für Physik, Johannes-Gutenberg-Universität Mainz, Germany.

[2] F. Steglich, J. Aarts, C. D. Bredel, W. Lieke, D. Meschede, W. Franz, and H. Schäfer, *Phys. Rev. Lett.* **43**, 1892 (1979).

[3] F. Steglich, *Physik Journal* **3**, 8/9-61 (2004).

[4] P. W. Anderson, *Phys, Rev.* **124**, 41 (1961).

[5] P. W. Anderson, *Phys. Rev. B* **30**, 1549 (1984).

[6] M. R. Norman, *Phys. Rev. B* **37**, 4987 (1988).

[7] M. Tinkham, *Introduction to Superconductivity*, 2nd Ed., McGraw-Hill Book Co. , New York (1996).

[8] J. G. Bednorz and K. A. Müller, *Z. Phys. B* **64**, 189 (1986).

[9] M. Sigrist and K. Ueda, *Rev. Mod. Phys.* **63**, 239 (1991).

[10] C. C. Tsuei and J. R. Kirtley, *Rev. Mod. Phys.* **72**, 969 (2000).

[11] X. J. Zhou, T. Cuk, T. Devereaux, N. Nagaosa, and Z. -X. Shen, *Handbook of High-Temperature Superconductivity*, eds. J. R. Schrieffer and J. S. Brooks, Springer, New York (2007).

[12] D. J. Scalapino, *Science* **284**, 1282 (1999).

[13] E. Bauer, G. Hilscher, H. Michor, Ch. Paul, E. W. Scheidt, A. Gribanov, Yu. Seropegin, H. Noël, M. Sigrist, and P. Rogl, *Phys. Rev. Lett.* **92**, 027003 (2004).

[14] P. W. Anderson, *Phys. Rev. B* **30**, 4000 (1984).

[15] D. F. Agterberg and R. P. Kaur, *Phys. Rev. B* **75**, 064511 (2007) *and the references cited within.*

[16] A. Bianchi, R. Movshovich, C. Capan, P. G. Pagliuso, and J. L. Sarrao, *Phys. Rev. Lett.* **91**, 187004 (2003).

[17] C. Geibel, S. Thies, D. Kaczorowski, A. Mehner, A. Grauel, B. Seidel, U. Ahlheim, R. Helfrich, K. Petersen, C. D. Bredel, and F. Steglich, *Z. Phys. B* **83**, 305 (1991).

[18] C. Geibel, C. Schank, S. Thies, H. Kitazawa, C. D. Bredel, A. Böhm, M. Rau, A. Grauel, R. Caspary, R. Helfrich, U. Ahlheim, G. Weber, and F. Steglich, *Z. Phys. B* **84**, 1 (1991).

[19] C. Geibel, A. Böhm, R. Caspary, K. Gloos, A. Grauel,P. Hellmann, R. Modler, C. Schank, G. Weber, and F. Steglich, *Physica B* **186-188**, 188 (1993).

[20] M. Jourdan, M. Huth, and H. Adrian, *Nature* **398**, 47 (1999).

[21] A. Krimmel, P. Fischer, B. Roessli, H. Maletta, C. Geibel, C. Schank, A. Grauel, A. Loidl, and F. Steglich, *Z. Phys. B* **86**, 161 (1992).

[22] R. H. Heffner and M. R. Norman, *Comm. Cond. Mat. Phys.* **17**, 361 (1996).

[23] R. Caspary, P. Hellmann, M. Keller, G. Sparn, C. Wassilew, R. Köhler, C. Geibel, F. Steglich, and N. E. Phillips, *Phys. Rev. Lett.* **71**, 2146 (1993).

[24] K. Knöpfle, A. Mavromaras, L. M. Sandratskii, and J. Kübler, *J. Phys.: Condens. Matter* **8**, 901 (1996).

[25] G. Zwicknagel, A. Yaresko, and P. Fulde, *Phys. Rev. B* **68**, 052508 (2003).

[26] N. K. Sato, *J. Phys.: Condens. Matter* **15**, 1937 (2003).

[27] P. Thalmeier, T. Watanabe, K. Izawa, and Y. Matsuda, *Phys. Rev. B* **72**, 024539 (2005).

[28] F. Steglich, *Physica B* **359**, 326 (2005).

[29] E. Blackburn, A. Hiess, N. Bernhoeft, M. C. Rheinstädter, W. Häußler, and G. H. Laner, *Phys. Rev. Lett.* **97**, 057002 (2006).

[30] S. I. Fujimori, Y. Saitoh, T. Okane, A. Fujimori, H. Yamagami, Y. Haga, E. Yamamoto, and Y. Onuki, *Nature Physics* **3**, 618 (2007).

[31] G. Zwicknagl and M. Reese, *J. Magn. Mag. Mat.* **310**, 201 (2007).

[32] L. Paolasini, J. A. Paixao, G. H. Lander, A. Delapalmes, N. Sato, and T. Komatsubara, *J. Phys.: Condens. Matter* **5**, 8905, (1993).

[33] A. Hiess, N. Bernhoeft, N. Metoki, G. H. Lander, B. Roessli, N. K. Sato, N. Aso, Y. Haga, Y. Koike, T. Komatsubara, and Y. Onuki, *J. Phys.: Condens. Matter* **18**, 437 (2006).

[34] J. Hessert, M. Huth, M. Jourdan, H. Adrian, C. T. Rieck, and K. Scharnberg, *Physica B* **230-232**, 373 (1997).

[35] N. R. Werthamer, E. Helfand, and P. C. Hohenberg, *Phys. Rev.* **147**, 295 (1966).

[36] K. Maki, *Phys. Rev.* **148**, 362 (1966).

[37] H. Tou, Y. Kitaoka, K. Asayama, C. Geibel, C. Schank, and F. Steglich, *J. Phys. Soc. Jpn.* **64**, 725 (1995).

[38] S. Yip and A. Garg, *Phys. Rev. B* **48**, 3304 (1993).

[39] K. Matsuda, Y. Kohori, and T. Kohara, *Phys. Rev. B* **55**, 12233 (1997).

[40] M. Hiroi, M. Sera, N. Kobayashi, Y. Haga, E. Yamamoto, and Y. Onuki, *J. Phys. Soc. Jpn.* **66**, 1595 (1997).

[41] N. Metoki, Y. Haga, Y. Koike, and Y. Onuki, *Phys. Rev. Lett.* **80**, 5417 (1998).

[42] N. Bernhoeft, N. Sato, B. Roessli, N. Aso, A. Hiess, G. H. Lander, Y. Endoh, and T. Komatsubara, *Phys. Rev. Lett.* **81**, 4244 (1998).

[43] N.K. Sato, N. Aso, K. Miyake, R. Shiina, P. Thalmeier, G. Varelogiannis, C. Geibel, F. Steglich, P. Fulde, and T. Komatsubara, *Nature* **410**, 340 (2001).

[44] M. Huth, M. Jourdan, and H. Adrian, *Eur. Phys. J. B* **13**, 695 (2000).

[45] N. Bernhoeft, *Eur. Phys. J. B* **13**, 685 (2000).

[46] Y. Nisikawa and K. Yamada, *J. Phys. Soc. Jpn.* **71**, 237 (2002).

[47] H. Ikeda, *J. Phys.: Condens. Matter* **15**, S2247 (2003).

[48] M. Kyogaku, Y. Kitaoka, K. Asayama, C. Geibel, C. Schank, and F. Steglich, *J. Phys. Soc. Jpn.* **62**, 4016 (1993).

[49] P. Thalmeier, *Eur. Phys. J. B* **27**, 29 (2002).

[50] P. McHale, P. Fulde, and P. Thalmeier, *Phys. Rev. B* **70**, 014513 (2004).

[51] P. Fulde and G. Zwicknagl, *J. Supercond.* **17**, 631 (2004).

[52] J. Chang, I. Eremin, P. Thalmeier, and P. Fulde, *Phys. Rev. B* **75**, 024503 (2007).

[53] N. Bernhoeft, A. Hiess, N. Metoki, G. H. Lander, and B. Roessli, *J. Phys.: Condens. Matter* **18**, 5961 (2006).

[54] P. Thalmeier and K. Maki, *Europhys. Lett.* **58**, 1 (2002).

[55] T. Watanabe, K. Izawa, Y. Kasahara, Y. Haga, Y. Onuki, P. Thalmeier, K. Maki, and Y. Matsuda, *Phys. Rev. B* **70**, 184502 (2004).

[56] H. Won, D. Parker, K. Maki, T. Watanabe, K. Izawa, and Y. Matsuda, *Phys. Rev. B* **70**, 140509(R) (2004).

[57] L. Tewordt and D. Fay, *Phys. Rev. B* **72**, 014502 (2005).

[58] P. M. Oppeneer and G. Varelogiannis, *Phys. Rev. B* **68**, 214512 (2003).

[59] A. Hiess, E. Blackburn, N. Bernhoeft, and G. H. Lander, *Phys. Rev. B* **76**, 132405 (2007).

[60] C. Stock, C. Broholm, J. Hudis, H. J. Kang, and C. Petrovic, *Phys. Rev. Lett.* **100**, 087001 (2008).

[61] H. Shimahara, *Phys. Rev. B* **72**, 134518 (2005).

[62] J. C. Xavier and E. Dagotto, *Phys. Rev. Lett.* **100**, 1464003 (2008).

[63] M. Scheffler, M. Dressel, M. Jourdan, and H. Adrian, *Nature* **438**, 1135 (2005).

[64] M. Dressel and M. Scheffler, *Ann. Phys.* **15**, 535 (2006).

[65] P. Drude, *Phys. Z.* **1**, 161 (1900).

[66] A. N. Yaresko, V. N. Antonov, and B. N. Harmon, *Phys. Rev. B* **68**, 214426 (2003).

[67] N. Kernavanois, J.-X. Boucherle, P. Dalmas de Réotier, F. Givord, E. Lèlievre-Berna, E. Ressouche, A. Rogalev, J.-P. Sanchez, N. Sato, and A. Yaouanc, *J. Phys.: Condens. Matter* **12**, 7857 (2000).

[68] S. H. Yang, H. Kumigashira, T. Yokoya, A. Chainani, T. Takahashi, S. J. Oh, N. Sato, and T. Komatsubara, *J. Phys. Soc. Jpn.* **65**, 2685 (1996).

[69] T. Terashima, K. Enomoto, T. Konoike, S. Uji, N. Sato, and H. Yamagami, *Physica B* **378-380**, 991 (2006).

[70] A. Schröder, J. G. Lussier, B. D. Gaulin, J. D. Garrett, W. J. L. Buyers, L. Rebelsky, and S. M. Shapiro, *Phys. Rev. Lett.* **72**, 136 (1994).

[71] A. Hiess, P. J. Brown, E. Lèlievre-Berna, B. Roessli, N. Bernhoeft, G. H. Lander, N. Aso, and N. Sato, *Phys. Rev. B* **64**, 134413 (2001).

[72] N. Aso, B. Roessli, N. Bernhoeft, R. Calemczuk, N. Sato, Y. Endoh, T. Komatsubara, A. Hiess, G. H. Lander, and H. Kadowaki, *Phys. Rev. B* **61**, R11867 (2000).

[73] B. D. Gaulin, M. Mao, C. R. Wiebe, Y. Qiu, M. Shapiro, C. Broholm S.-H. Lee, and J. D. Garrett, *Phys. Rev. B* **66**, 174520 (2002).

[74] H. Tou, Y. Kitaoka, T. Kamatsuka, K. Asayama, C. Geibel, F. Steglich, S. Süllow, and J. A. Mydosh, *Physica B* **230-232**, 360 (1997).

[75] Y. Dalichaouch, M. C. de Andrade, and M. B. Maple, *Phys. Rev. B* **46**, 8671 (1992).

[76] N. Sato, N. Koga, and T. Komatsubara, *J. Phys. Soc. Jpn.* **65**, 1555 (1996).

[77] M. Jourdan, A. Zakharov, M. Foerster, and H. Adrian, *Phys. Rev. Lett.* **93**, 097001 (2004).

[78] K. Ishida, D. Ozaki, T. Kamatsuka, H. Tou, M. Kyogaku, Y. Kitaoka, N. Tateiwa, N. Sato, N. Aso, C. Geibel, and F. Steglich, *Phys. Rev. Lett.* **89**, 037002 (2002).

[79] M. Foerster, A. Zakharov, and M. Jourdan, *Phys. Rev. B* **76**, 144519 (2007).

[80] A. P. Mackenzie and Y. Maeno, *Rev. Mod. Phys.* **75**, 657 (2003).

[81] J. A. Duffy, S. M. Hayden, Y. Maeno, Z. Mao, J. Kulda, and G. J. McIntyre, *Phys. Rev. Lett.* **85**, 5412 (2000).

[82] K. Ishida, H. Mukuda, Y. Kitaoka, K. Asayama, Z. Mao, Y. Mori, and Y. Maeno, *Nature* **396**, 658 (1998).

[83] R. Joynt and L. Taillefer, *Rev. Mod. Phys.* **74**, 235 (2002).

[84] G. Zwicknagl and P. Fulde, *J. Phys.: Condens. Matter* **15**, S1911 (2003).

[85] A. Llobet, A. D. Christianson, W. Bao, J. S. Gardner, I. P. Swainson, J. W. Lynn, J.-M. Mignot, K. Prokes, P. G. Pagliuso, N. O. Moreno, J. L. Sarrao, J. D. Thompson, and A. H. Lacerda, *Phys. Rev. Lett.* **95**, 217002 (2005).

[86] S. Ohira-Kawamura, H. Shishido, A. Yoshida, R. Okazaki, H. Kawano-Furukawa, T. Shibauchi, H. Harima, and Y. Matsuda, *Phys. Rev. B* **76**, 132507 (2007).

[87] M. Foerster, *Supraleitende dünne Schichten der Schwere-Fermionen Verbindung* UNi_2Al_3 , Diploma-thesis (2003), Institut für Physik, Johannes-Gutenberg-Universität Mainz, Germany (unpublished).

[88] J. R. Heffelfinger and C. B. Carter, *Surf. Sci.* **389**, 188 (1997).

[89] G. Binnig, H. Rohrer, H. Gerber, and C. Weibel, *Phys. Rev. Lett.* **50**, 120 (1983).

[90] M. Lannoo and P. Friedel, *Atomic and Electronic Structure of Surfaces*, Springer-Verlag, Berlin-Heidelberg (1991).

[91] S. A. Hayward, S. A. T. Redfern, and E. K. H. Salje, *J. Phys.: Condens. Matter* **14**, 10131 (2002).

[92] M. Huth, A. Kaldowski, J. Hessert, C. Heske, and H. Adrian, *Physica B* **199&200**, 116 (1994).

[93] A. Zakharov, M. Jourdan, M. Foerster, and H. Adrian, *Physica B* **359**, 1108 (2005).

[94] N. L. Ross, J. Zhao, and R. J. Angel, *J. Solid State Chem.* **177**, 1276 (2004).

[95] S. Geller and E. A. Wood, *Acta Cryst.* **9**, 563 (1956).

[96] A. R. Wildes, J. Mayer, and K. Theis-Bröhl, *Thin Solid Films* **401**, 7 (2001).

[97] A. Zakharov, *Unconventional superconductivity in the heavy fermion compound UNi_2Al_3*, PhD-thesis (2008), Institut für Physik, Johannes-Gutenberg-Universität Mainz, Germany.

[98] A. Conca, *Magnetic Tunneling Junctions with the Heusler compound $Co_2Cr_{0.6}Fe_{0.4}Al$*, PhD-thesis (2007), Institut für Physik, Johannes-Gutenberg-Universität Mainz, Germany.

[99] W. Braun, *Applied RHEED*, Springer-Verlag, Berlin-Heidelberg (1999).

[100] W. K. Chu, J. W. Mayer, and M. A. Nicolet, *Backscattering spectrometry*, Academic Press, Inc., Orlando (1978).

[101] available at *http://www.genplot.com/*

[102] P. F. Miceli and C. J. Palmstrøm, *Phys. Rev. B* **51**, 5506 (1995).

[103] L. G. Parratt, *Phys. Rev.* **95**, 359 (1954).

[104] available at *http://www.hmi.de/bensc/instrumentation/instrumente/v6/refl/parratt_en.htm*

[105] J. P. Hannon, G. T. Trammell, M. Blume, and D. Gibbs, *Phys. Rev. Lett.* **61**, 1245 (1988).

[106] M. Jourdan, A. Zakharov, A. Hiess, T. Charlton, N. Bernhoeft, and D. Mannix, *Eur. Phys. J. B* **48**, 445 (2005).

[107] A. Hiess, N. Bernhoeft, S. Langridge, C. Vettier, M. Jourdan, M. Huth, H. Adrian, and G. H. Lander, *Physica B* **259-261**, 631 (1999).

[108] J. P. Hill and D. F. McMorrow, *Acta Cryst. A* **52**, 236 (1996).

[109] A. Ishiguro, A. Sawada, Y. Inada, J. Kimura, M. Suzuki, N. Sato, and T. Komatsubara, *J. Phys. Soc. Jpn.* **64**, 378 (1995).

[110] J. Kondo, *Progr. Theo. Phys.* **32**, 37 (1964).

[111] M. Huth, J. Hessert, M. Jourdan, A. Kaldowski, and H. Adrian, *Phys. Rev. B* **50**, 1309 (1994).

[112] I. Giaver, *Phys. Rev. Lett.* **5**, 147 and 464 (1960).

[113] J. P. Carbotte, *Rev. Mod. Phys.* **62**, 1027 (1990).

[114] W. L. McMillan, and J. M. Rowell *Tunneling and strong coupling Superconductivity*, in *Superconductivity*, Vol. 1, chapter 11, eds. R. D. Parks, Marcel Dekker, New York (1969).

[115] W. J. Tomasch, *Phys. Rev. Lett.* **16**, 16 (1966).

[116] M. Tinkham, *Phys. Rev. B* **6**, 1747 (1972).

[117] J. Geerk and H. v. Löhneysen, *Phys. Rev. Lett.* **99**, 257005 (2007).

[118] G. E. Blonder, M. Tinkham, and T. M. Klapwijk, *Phys. Rev. B* **25**, 4515 (1982).

[119] R. C. Dynes, V. Narayanamurti, and J. P. Garno, *Phys. Rev. Lett.* **41**, 1509 (1978).

[120] W. F. Brinkmann, R. C. Dynes, and J. M. Rowell, *J. Appl. Phys.* **41**, 1915 (1970).

[121] J. G. Simmons, *J. Appl. Phys.* **34**, 238 (1963).

[122] A. Ortiz, J. C. Alonso, V. Pankov, A. Huanosta, and E. Andrade, *Thin Sol. Films* **369**, 74 (2000).

[123] B. J. Jönsson-Åkerman, R. Escudero, C. Leighton, S. Kim, and I. K. Schuller, *Appl. Phys. Lett.* **77**, 1870 (2000).

[124] Z.-S. Zhang, and D. A. Rabson, *J. Appl. Phys.* **95**, 557 (2004).

[125] D. A. Rabson, B. J. Jönsson-Åkerman, A. H. Romero, R. Escudero, C. Leighton, S. Kim, and I. K. Schuller, *J. Appl. Phys.* **89**, 2786 (2001).

[126] D. Parker and P. Thalmeier, *Phys. Rev. B* **75**, 184502 (2007).

[127] H. Suhl, B. T. Matthias, and L. R. Walker, *Phys. Rev. Lett.* **3**, 552 (1959).

[128] N. Sato, T. Sakon, N. Takeda, T. Komatsubara, C. Geibel, and F. Steglich, *J. Phys. Soc. Jpn.* **61**, 32 (1992).

[129] M. Foerster, M. Jourdan, A. Zakharov, C. Herbort, and H. Adrian, *J. Magn. Mag. Mat.* **310**, 346 (2007).

[130] M. N. Kunchur, S. I. Lee, and W. N. Nang, *Phys. Rev. B* **68**, 064516 (2003).

[131] P. Anderson, *Phys. Rev. Lett.* **9**, 309 (1962).

[132] P. Anderson and Y. Kim, *Rev. Mod. Phys.* **36**, 39 (1964).

[133] M. Huth, *Transportphänomene und Kohärenz in epitaktisch gewachsenen Schwere-Fermionen-Supraleiter-Filmen*, PhD-thesis (1995), Fachbereich Physik, Technische Hochschule Darmstadt, Germany.

[134] S. Süllow, B. Becker, A. de Visser, M. Mihalik, G. J. Nieuvenhuyst, A. A. Menovsky, and J. A. Mydosh, *J. Phys.: Condens. Matter* **9**, 913 (1997).

Acknowledgements

Datenschutz

List of Publications

Author *Anisotropic transport properties of UNi_2Al_3 thin films*
M. Foerster, A. Zakharov, and M. Jourdan
Phys. Rev. B 76, 144519 (2007).

Electronic properties of a-oriented UPd_2Al_3 thin films*
M. Foerster, M. Jourdan, A. Zakharov, C. Herbort, and H. Adrian
J. Magn. Mag. Mat. 310, 346 (2007).

Coauthor *Preparation of superconducting films of UNi_2Al_3*
A. Zakharov, M. Jourdan, M. Foerster and H. Adrian
Physica B 359, 1108 (2005).

Evidence for multiband superconductivity in the heavy fermion compound UNi_2Al_3
M. Jourdan, A. Zakharov, M. Foerster, and H. Adrian
Phys. Rev. Lett. 93, 097001 (2004).

Preparation of thin films of the heavy fermion superconductor UNi_2Al_3
M. Jourdan, A. Zakharov, M. Foerster, and H. Adrian
J. Magn. Mag. Mat. 272-276, E163-E164 (2004).

Conference Contributions

2007 Spring meeting of the German physical society (DPG), Regensburg, Germany
Poster presentation

2006 International Conference on Magnetism ICM, Kyoto, Japan
Poster presentation

2006 Spring meeting of the German physical society (DPG), Dresden, Germany
Oral presentation

2005 Spring meeting of the German physical society (DPG), Berlin, Germany
Oral presentation

2004 International Conference on Strongly Correlated Electron Systems SCES, Karlsruhe, Germany
Poster presentation, Coauthor

Curriculum Vitae

Datenschutz

Eidesstattliche Erklärung

Hiermit erkläre ich an Eides statt, dass ich die vorliegende Arbeit selbstständig und nur unter Verwendung der angegebenen Hilfsmittel verfasst habe.

Ich habe bisher keinen Promotionsversuch unternommen.

Mainz,